THE DEVELOPMENT OF A NOVEL METHOD FOR ARRESTING TUNNEL EXPLOSIONS

A thesis submitted for the Degree of Doctor of Philosophy

By

Michael Dwomoh, BEng (Hons)

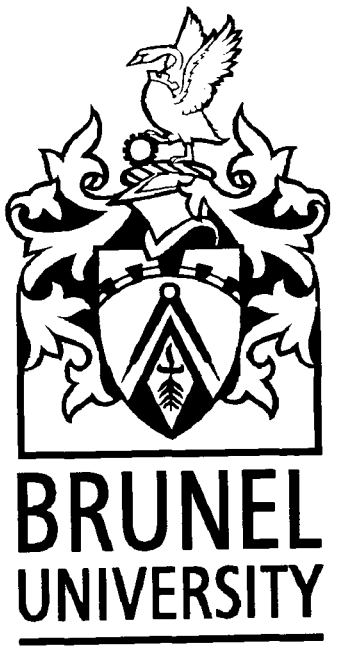

Department of Mechanical Engineering

October 1998

ABSTRACT

The onset of an explosion in an underground mining environment is a threat that has over years attracted a lot of attention. Much of this attention has focused on either arresting the explosion after it has been initiated or preventing the initiation. The methods devised have proved successful in most cases, but on the odd occasion that they fail, the end results can be disastrous. There have been fatalities from underground mining explosions as a result of fires burning and sapping all the oxygen in the atmosphere leading to asphyxiation. A different approach to arresting these explosions would enhance safety in the face of increased productivity. A novel method using an explosion door with a porous media acting as a shock wave attenuator and arresting the flames has been introduced.

This research investigates the ability of the porous media used in the explosion door to withstand explosions. The performance of the porous media is crucial, as its failure would render the explosion door useless. In order to assess the performance of the porous media, a shock tube was built capable of generating shock waves with a Mach number of 1.5. By placing samples of the porous media within the test section of the shock tube, pressure measurements were taken fore and aft of the porous media as it was impinged upon by the shock wave. Tests were also conducted using thin orifice plates to provide data for comparing the performance characteristics of the porous media. Computational fluid dynamics (CFD) simulations of the porous media and the orifice plates were performed to validate the experimental work as well providing graphic detail of the flow around the test specimen.

The work presented in this thesis makes a contribution to the efforts towards the provision of a safe underground environment. This contribution is achieved by investigating the performance of the porous media to be used in an explosion door and correlating the performance of the porous media with thin orifice plates. The porous media in the work presented here is currently used in the castings industry and its application as a shock wave attenuator and fire arrester would contribute greatly to the well being of all people working underground.

ACKNOWLEDGEMENTS

This thesis is dedicated to my late mother, SARAH, who was not there when it all started because she caught the bus to heaven before the printer could start running.

I am very grateful to Dr. Darron Dixon-Hardy for giving me the opportunity for realising his ideas through his support, guidance and critical mind throughout the course of this work.

Those who suggested, discussed, helped, read, encouraged, are the people who really made it happen. I am indebted to Dr. Reza Mokhtarzadeh, Dr. David Stribling, Dr. Rita Kaur, Changjiang Wang, Mamadou Silue, Faustin Ondore, Matthew Blay, Sara Al-Sabti, Anthony Morgan, Richard Torrens, and Debarati Datta.

Those who made things and bought things made the laboratory work a joy. I would like to thank Bob Webb, John Langdon, Clive Barrett, Tony Whitby, Keith Withers and Paul Chapman.

I would like to thank the brothers and sisters, Lawrence, Patrick, Sarah, and Elizabeth.

To the Clarkes, Anita, Stephen, and especially Franklyn.

That's all.

CONTENTS

LIST OF FIGURES

LIST OF TABLES

NOMENCLATURE

C_μ	Empirically determined constant in the turbulent viscosity equation
$C_{1\varepsilon}$	Empirical constant in the k-ε turbulence model
C_2	Inertial resistance factor in the porous media momentum equation
$C_{2\varepsilon}$	Empirical constant in the k-ε turbulence model
$C_{3\varepsilon}$	Empirical constant in the k-ε turbulence model
c_v	Specific heat capacity at constant volume (J/kgK)
e	Internal energy (J)
E	Total energy (J)
F_i	External body forces in the *i*-direction
G_b	Generation of turbulence due to buoyancy
g	Gravitational acceleration (m/s^2)
G_k	Rate of production of turbulent kinetic energy
h	Enthalpy (J/kg)
k	Conductivity term in the energy equation
k	Turbulent kinetic energy (m^2/s^2)
K_G	Gas-phase constant
K_{St}	Dust constant
M	Molecular weight (kg/kgmol)
MIE	Minimum ignition energy (J)
M_s	Moving shock Mach number
M_t	Turbulent Mach number
n	Value at current time level, t
$\dot{q}$	the rate of volumetric heat addition per unit mass.
p	Static pressure (N/m^2)
P_{max}	Maximum explosion pressure (N/m^2)
$(dP/dt)_{max}$	Maximum rate of pressure rise (N/m^2s)
R	Molar gas constant (J/kgK)
r	Radial co-ordinate
R	Rate-of-strain term
S_i	Source term for the *i*th (x, y, or z) momentum equation

S_i	Curved incident shock wave
S_m	Source mass term
S_r	Reflecting shock wave
T	Temperature (K)
T_{ref}	Reference temperature (K)
t	Time (s)
u, v, w	Velocity in the x, y, z directions (m/s)
u_p	Induced mass motion behind a shock wave (m/s)
W	Moving shock wave velocity (m/s)
x, y, z	Rectangular Cartesian co-ordinates
α	Inverse Prandtl number for turbulent transport
σ	Empirical constant in the k-ε turbulence model
Φ	Fluid property, e.g. density, pressure, temperature
ϕ	Air porosity
ε	Dissipation rate of the kinetic energy (m^2/s^3)
γ	Ratio of specific heat capacities
ρ_c	Bulk density (ceramic foam material) (kg/m^3)
ρ_s	Material density (ceramic foam material) (kg/m^3)
ρ	Mean density (kg/m^3)
$\overline{\rho u_i' h'}$	Correlation term in the enthalpy equations
$\overline{\rho u_i' m_i'}$	Correlation term in the species conservation
$-\rho\overline{u_i u_j}$	Turbulence correlations
τ_{ij}	Viscous stress which acts in the j-direction on a surface normal to the i-direction
σ_k and σ_ε	Prandtl numbers for k and ε
Δt	Time step (s)
μ	Dynamic viscosity (kg/m-s)
μ_t	'Eddy' or turbulent viscosity (kg/m-s)

CHAPTER 1 Introduction

Coal has been mined throughout the world for centuries and although there has been a significant reduction in the quantity of coal mined in the UK in recent years, global production has actually increased. The increases in coal production have largely taken place in China, South America, Australia and South Africa and are as a result of massive increases in productivity achieved by a greater use of mechanisation and achieved with a decrease in manpower. It has long been recognised that increased production imposes great demands on the mine environment since underground coal mining releases coal dust, heat, methane and other contaminants into the underground airstream. Methane is the main contaminant of concern in this thesis since it has the potential to cause an explosion. The dangers caused by an excess of methane cannot be overstated, as there have been several reports of fatal mining accidents throughout the world as reported by Cybulska[1] in her work on coal dust explosions.

An ignition of methane is usually the initial phase associated with a full-blown underground explosion. The action of a cutter pick or some other device that can cause a spark of sufficient energy to ignite a pocket of methane at concentrations between 5 - 15% is a common mining occurrence. Once the methane is ignited it burns initially with a slow flame that has the potential to increase in strength and speed. If the quantity and concentration are sufficient then it is possible for the methane to detonate and cause significant though often localised damage. The greatest danger, however, is where the pressure wave caused by the expanding, burning methane forces coal dust from the roadway into the air. If the coal dust is at a sufficient concentration and the heat from the burning methane is sufficient to ignite the coal dust a secondary phenomenon can take place. The coal dust can ignite and possibly detonate thereby creating a very dangerous underground situation.

There are essentially two methods of dealing with methane emission. The first is to dilute the methane, as it appears in the ventilating system airstream, the second is methane drainage. The latter method is widely practised in the UK. However, even the best prevention methods fail leading to an explosion.

To combat this problem most mines have some form of active safety monitoring system. Such systems may take the form of using an active barrier or a passive barrier. Though independent of the use of barrier systems there are instances when a methane draining system is used. In reality, methane drainage is not an active safety monitoring system as it uses instrumentation to monitor parameters within it. Thus the decision to use methane drainage is dependent on other factors such as whether the gas is to be used for heat the pit baths or even for power generation. For the latter case, methane may be drained. This could be true even if no drainage means that the 1.25% concentration limit is not reached in the roadway. However, if no drainage is used and the airflow cannot reduce the methane to less than 1.25% then drainage must be used. In some cases both active and passive barriers are utilised. The former type of barrier is widely used throughout the mining community in light of the shortcomings of the passive barrier systems. Active barriers work by detecting a change in static pressure caused by the explosion, from the oncoming explosion front. They then empty some inert material into the path of the oncoming explosion.

Though active barriers are in use, there are instances when they fail. In particularly powerful explosions, the chances are that these barriers may miss the flame front altogether, leaving it to burn until it runs out of energy as well as asphyxiating miners further away from the source of the explosion. In weak explosions the barriers could also fail in their operation, as the blast wave preceding the flame front might not be strong enough to activate the barriers.

To further enhance the current safety devices in underground mining environments as well as successfully arrest an explosion where primary active barriers fail, a novel method for arresting underground mining explosions has been devised. Such a system would be used along with the current systems and placed anywhere within the mining environment, such that it is activated when the primary active barriers fail. This explosion barrier takes the form of a door with a region that allows the shock wave preceding the explosion to pass through and successfully arrest the flame front.

Though there has been some research into explosion barriers in underground mining environments by Michelis and Kleine[2], they all work on the principle of deflecting the

shock wave and not allowing it to pass through. The explosion door proposed in this work will be permeable and will allow the passage of the shock wave through the permeable section but arrest the flame front that will be travelling behind the blast wave. Such a feature will significantly reduce the risk of the explosion barrier being damaged, thereby rendering it ineffective.

The porous media within the explosion door is crucial to the performance of the door. It is meant to minimise the pressure drop to such an extent that the door and the porous media remain intact when the flame front that is travelling behind the shock wave arrives. In order to investigate the ability of the porous media to remain intact, tests will be conducted where the pressure reflected and transmitted are recorded. Such data will also be compared with pressure data obtained from thin orifice plates tested under the same boundary conditions. The results from the comparison tests are meant to categorise the behaviour of the porous media in terms of orifice plates for which much data has been obtained. As an example, the pressure attenuation characteristics of the various porous media would be similar to thin orifice plates with blockage areas of between 50% and 60%. With such information experimental tests and computer simulations of thin orifice plates could quickly show the likely performance of the porous media. This is especially useful as computational modelling of transient flow in porous media is not well represented in the commercial codes.

By analysing the performance of the permeable region of the explosion door, it is hoped that this research will provide an insight into the characteristics of the porous media that will be adopted for use in the explosion door. This research will design and use a shock tube to provide the shock waves that are produced in mining explosions. The incident shock wave will then impinge upon the porous media with data being collected from pressure transducers located fore and aft of the porous media. Previous work by Rogg et al[3] and Levy et al[4] on the flow of shock waves through porous media has concentrated on either placing the porous media at the end of the shock tube, thus measuring the incident and reflected waves, or using a deformable porous media, similar to a sponge, which will not be used in this research.

1.1 Original contribution to the body of knowledge

This brief introduction has highlighted the shortcomings of explosion barriers currently used in underground tunnels. Though the arresting of these explosions can be successful, there are some failures and it is in an effort to minimise the effects of an explosion that the explosion door has been devised. The door in its entirety contains several parts, however, in this research the porous material used to attenuate the shock wave preceding the flame front is the part of interest. The ability of the porous material to attenuate the shock wave without being damaged, and subsequently quenching the flame front will determine its use in the explosion door. However, detailed knowledge on the performance of porous materials for attenuating explosions is not prevalent in the literature. Tests will also be conducted on thin orifice plates with varying blockage areas (BA) and hole configurations to ascertain a correlation between the thin orifice plates and the porous material for the explosion door.

Thus it is seen that such performance data will contribute to the body of knowledge not only on shock wave attenuation and porous media research but also to that of underground mining safety. It will also introduce a new area of application for the porous media used in this work which is currently used as a filter in the castings industry.

The performance data will take the form of the following: -

- *the pressure drop across barriers of various thickness and area ratios*
- *the nature of the flow field when the shock wave meets the barrier*
- *the effect of multiple barriers on the reduction of shock strength*
- *the effect of multiple perforations on shock wave attenuation*
- *correlation between the performance of thin orifice plates and the porous media.*

1.2 Structure of this thesis

This thesis is divided into eight chapters with chapter one being the introduction.

In **chapter two**, an insight is given into coal dust and gas explosions. In order to help the reader better understand the phenomenon of explosions, a section is dedicated to the initiation of dust explosions in underground mining environments, from the formation of methane to a brief discussion on some of the accidents, highlighting the magnitudes of some of the more powerful explosions. Some characteristics that define the severity of explosions are introduced and definitions are given for the more common terms used in dust explosion research. The chapter ends with a review of some of the attempts made at modelling explosions in underground mines using computer software.

Leading on from chapter two, **chapter three** will then give a detailed insight into the state of current methods for arresting underground explosions. From the early days of passive barrier research right through to the proliferation of active barrier research, the reader is given the history of explosion protection underground to the advantages and disadvantages of the current active barriers. The disadvantages of the current systems allow the introduction of the new explosion door that is the subject of this research. The properties of the explosion door are discussed, giving its method of operation, likely structure, and a series of illustrations showing its intended mode of operation.

Chapter four gives an introduction to computational fluid dynamics (CFD), from the basics of fluid flow to the solution of turbulent flow. Here, Rampant, the software used for the experiments will be evaluated. The turbulence models used by Rampant to solve such problems will be discussed. This chapter also introduces porous media modelling, and the model for solving porous flow problems in Rampant. Particular emphasis will be given to the failings of the porous media model within the Rampant CFD code and thus its inability to model the flow through the porous media in the experiments conducted in this research. A brief account of discretisation schemes used to solve time marching problems to give the reader an insight to the ability of CFD to solve problems that will be encountered in this research.

Chapter five will introduce the porous media and the experimental set-up. The porous media, which is the main subject of this research, will be introduced, giving details on its manufacture, its current use in industry, and other porous media used in shock wave research. As the shock tube is the main tool for experimental work, a brief introduction

will be given to the physics of shock tube flow including the subject of one-dimensional unsteady wave motion and a derivation of the governing equations for one-dimensional shock tube motion. Also the subject of compression, expansion, transmitted, and reflected wave theory will be discussed, as they are an integral part of the behaviour of shock waves in obstructed flows. The design and specification of the shock tube used in this research and the experimental apparatus will also be introduced in this section of the report and some initial experimental results given and analysed. These experimental results will be compared with the results of the analytical resolution of the shock tube flow. Further results of more extensive testing will also be given.

A thorough discussion of the CFD and experimental results from the porous media and orifice plates tests will be given in **chapter six.** Here a comparison table will be given for the equivalent single orifice plate results for the porous media. Also a table of the main properties and characteristics of the porous media that will be of benefit to designers of the explosion door will be given. This in particular will add to the body of knowledge on porous media and on the ceramic foam that could be applied in an underground mining environment in the future.

Chapter seven will summarise the main findings that will contribute to the body of knowledge.

Chapter eight will put forward some conclusions and some recommendations for further work.

CHAPTER 2 Coal dust and gas explosions

2.1 Introduction

An explosion is a phenomenon that results from a sudden release of energy. Explosions can be classified as deflagrations or detonations. They may come from coal dust, methane, or wheat flour as in a grain elevator. The release of energy must be sudden, such that there is a local accumulation of energy at the site of the explosion. This accumulated energy is then dissipated in various ways, amongst which are blast waves.

As most explosions in an underground mining environment are initiated by methane, there is a critical value at which the percentage of methane in the air will be sufficient to initiate an explosion, as stated in the Mines and Quarries Acts[5].

Methane is a colourless, odourless, and tasteless gas. Its low density means that it accumulates in the high places of an underground mining environment where there is little or no movement of air. Chemically, methane is fairly inert; however, in a mining environment its explosive nature makes it dangerous especially as methane is a by-product of the diagenesis of carbonaceous material, which eventually results in the formation of coal or oil. Methane is explosive at concentrations between 5% and 15% in air, however, at 9.6% the air/methane mixture reaches its maximum explosibility.

This research work is primarily concerned with the shock wave produced by methane initiated coal dust explosions, which are defined by Essenhigh[6] as the rapid transmission of a combustion wave through a cloud of solid particles. For most coal dust explosions, it is the rapid chemical oxidation of the particles dispersed in air that supplies the sudden release in energy. This energy release increases the temperature so fast that there is an accompanying increase in the pressure, which can cause the formation of a shock wave, Hertzberg and Cashdollar[7].

2.2 *Initiation of dust explosions*

The main distinguishing factor between gas and dust explosions is the existence of only one phase in the former type. Gas combustion is a homogeneous process in which only molecular distances separate the smallest entities of fuel and air. Thorough mixing of fuel and oxidant is readily achieved and gravitational effects are negligible. However, in a dust/air mixture, the dust particles are strongly influenced by gravity. Thus, an essential prerequisite for a dust explosion is the formation of a dust/oxidant suspension. Uniformity of the dust cloud may not occur, leading to local variations in concentration. As dust suspensions can only be quiescent in the absence of a gravitational field, measurements of laminar burning velocities cannot be easily made in closed vessel explosion experiments. Also in addition to the concentration of dust in suspension, variations in other parameters such as particle size, shape and distribution can affect explosion characteristics of a dust since evolution of volatiles from and heat transfer into the particles depend on the exposed surface area as shown by Ogle et al[8]. The combustion process is complicated by the existence of a solid phase in addition to a gas phase in that the combustion process becomes a step-wise procedure and is dependent upon the nature of the combustible material.

Transfer of energy by thermal means through a temperature difference is a relatively slow process and depends very much on the external conditions such as the ambient pressure. Thus, a deflagrative explosion wave is subsonic in nature and sustained by a chemical reaction. However, decomposition by means of a detonation process proceeds very rapidly due to the very rapid transmission of the mechanical forces that are relatively independent of external conditions. Thus a detonation explosion wave is supersonic in nature and is sustained by the energy of the chemical reaction in the highly compressed explosive medium that exists within the wave.

It has been shown that the particle size is critical to the initiation of an explosion[9]. There is a critical size at which coal dust will ignite and explosibility tests using coal dust use a particle size of less than 74 μm. Thus, in order for the flame to propagate, the dust concentration must lie within an explosible region bounded by upper and lower limits. Basically, the smaller the particle size of the dust, the higher the intensity of the

explosion. This is because smaller particles burn faster, which in turn means faster burning of the surrounding particles causing a rapid increase in pressure and a subsequent increase in the destructive potential of the initial explosion.

Coal dust explosions then occur when the finely divided combustible matter is dispersed into an atmosphere containing sufficient oxygen to enable combustion and a source of ignition of appropriate energy[10]. However, there is a primary explosion initiated in a mine by a methane-air explosion that generates sufficient air pressure to disperse coal dust into the expanding combustion zone behind the pressure wave. Heat transfer to the coal dust particles results in the production of volatiles and tars from these particles. Thus there are two mechanisms by which the energy required for the activation of the explosion reaction can be transferred from exploded to unexploded material. One is primarily mechanical in nature, acting through pressure forces. The resulting impact on neighbouring materials is the basis for a detonation mechanism. The second mechanism for the propagation of an explosion reaction is thermal in nature. The material surrounding the initial explosion site is warmed above its decomposition temperature so that it explodes. This forms the basis of deflagration explosions.

Figure 2.1 to Figure 2.4 show the damaging effects of an explosion in air[11]. Though explosions in underground tunnels can be described as explosions in confined places. The shock wave travels along the tunnel network with obstructions in the way and these illustrations show the similar type of damage that could occur.

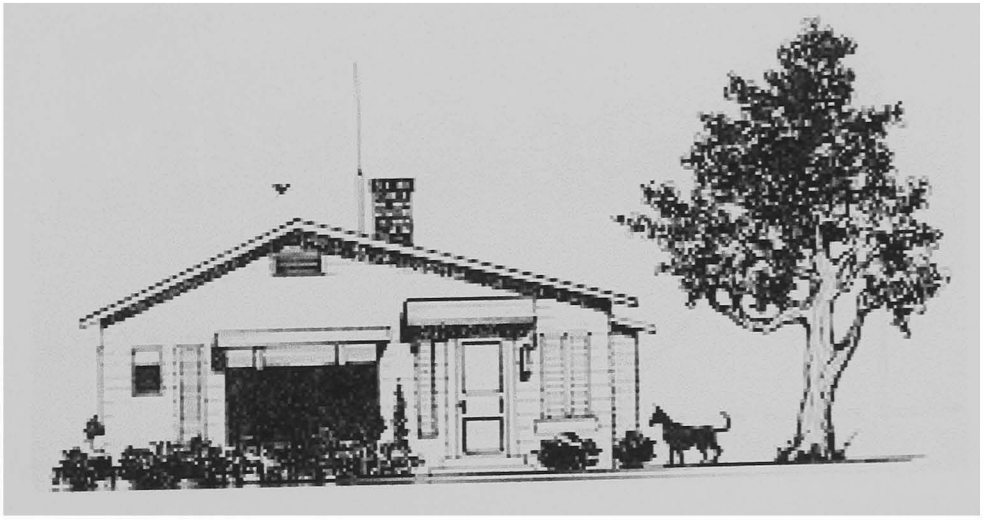

Figure 2.1 – A. Before the blast wave strikes. The atmosphere is still[11].

Figure 2.2 – B. Immediately after the passage of the shock front. The force experienced by the object is proportional to the pressure rise and the impact area.

In addition there is the force exerted by the blast wind. These blast wave effects then decrease quasi-exponentially with time until the pressure reaches atmospheric after which there is a slight negative phase, as shown in Figure 2.3, along with a reversed blast wind.

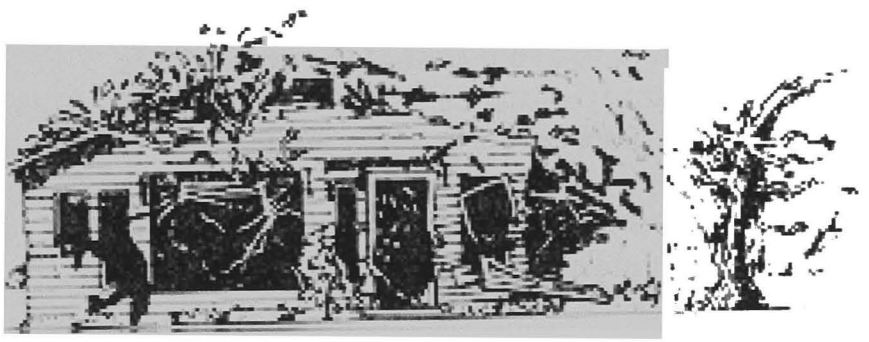

Figure 2.3 – C. In negative overpressure phase with reversed blast wind.

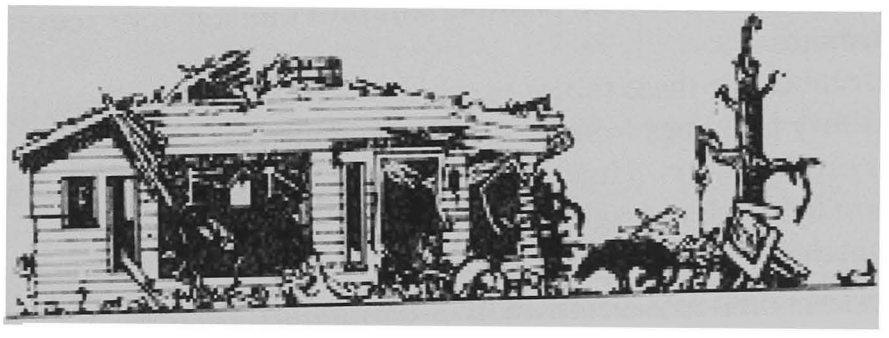

Figure 2.4 – D. After blast wave subsides.

The pressures in a typical blast wave such as that in Figure 2.1 to Figure 2.4 are illustrated schematically in Figure 2.5. The peak pressure associated with the shock wave is dependent upon the strength of the initial explosion.

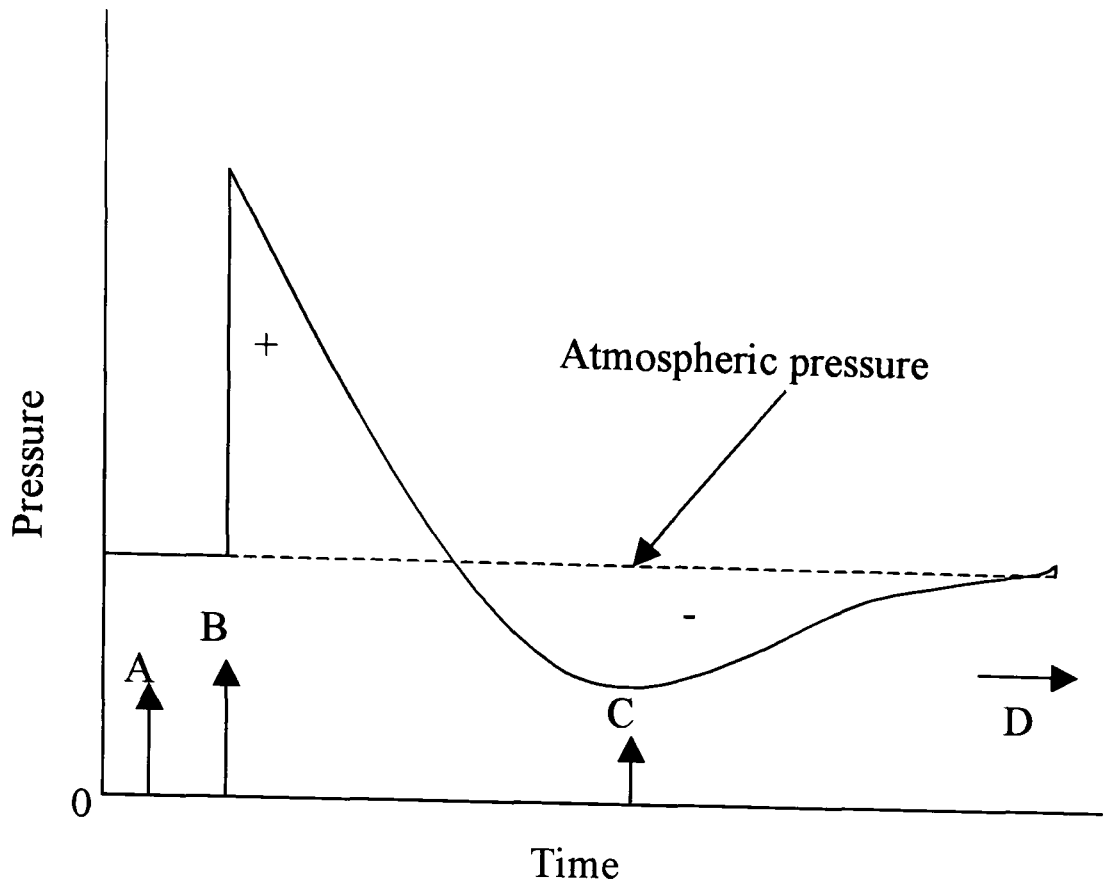

Figure 2.5 – Blast wave pressures plotted against time.

Since the extensive mechanisation of coal production, the coal cutting machine picks striking against rock causes most coal dust explosions. Whilst there is no evidence to suggest that any one type of machine is likely to cause ignition, the majority of all machine ignitions occur when coal-cutting machines cut into quartzitic rock in the floor or roof. Powell et al[12] have conducted some tests on this type of methane ignition, investigating the influence of cutting speed on the probability of ignition when cutting quartzitic sandstone in methane-air mixtures. The role of friction in ignitions was investigated; properties that help the ignition process - thermal and tribological properties, have all been investigated. The 'ingredients' needed for particle ignition are also given. The effect of cutting speed on the probability of ignition of quartzitic sandstone in methane-air mixtures was also investigated. There are three possible sources of rock ignition when being cut by a pick; hot surface on the pick; hot surface remaining on the rock; pieces of hot particles detaching from either the rock or the pick. In tests, it was found that every ignition was caused by a hot surface left on the rock. Investigations on the ability of water to reduce ignitions showed that the probability of an ignition occurring was reduced by a substantial amount.

The existence of detonations in coal mine blasts has been speculated upon for years as discussed by Griffith[13], and experiments conducted at the Safety in Mines Research Establishment by Rae[14] have demonstrated flame speeds and pressure-wave speeds of up to 1km/sec. There has been some research on detonations and the onset of deflagration to detonation transition (DDT) by Gardener et al[15]. However, most research on dust explosions has been concerned with deflagrative combustion, despite the fact that the shock wave that precedes an explosion can be supersonic in nature.

The severity of a coal dust explosion is dependent on the primary explosion, which is initiated by methane. As mentioned by Phylaktou and Andrews[16], and Phillips[17], the two most important parameters defining the severity of an explosion are the rate of pressure rise and the maximum pressure attained. At the early stages of explosion, characteristic features are high rates of pressure rise associated with fast flame speeds and significant overpressures. This is significant, as the most important part of arresting the flame is explosion behaviour at the early stages of its development. The flame speeds are also dependent on the aerodynamic roughness of the mining environment as experiments have shown that in smooth pipes, flame accelerations are much lower than in pipes with obstructions in them.

2.3 Recent explosions in underground mining environments

Coal dust explosions have been the subject of extensive research since the early 20th century, Edwards and Ford[18]. Artingstall and Corlett[19] have investigated the existence of detonations in coal mining explosions and even the weakest explosion has a flame speed of 30 m/s and a dynamic pressure of 1 kPa. In particularly powerful explosions, Vos[20], and Cybulski[21] have shown that the flame speed and dynamic pressure can go up to 1000 m/s and 1700 kPa, respectively.

Umezu et al[22] tried to experimentally replicate the results of an explosion, which occurred in a Japanese underground mine in 1974, which resulted in some fatalities. These experiments were carried out using a Y-shaped model to determine the correlation between parameters such as ignition point, gas distribution in a gas layer, and

propagation. Their results revealed that in a Y-shaped roadway, when violent explosions occurred in one side of the roadway, the other side of the roadway having a layer of methane gas did not always explode but combustion propagation could occur. However when the opposite roadway was filled with a uniform concentration of methane gas, explosion did occur and propagated to the open end of the model. Flame speeds could reach magnitudes of over 21 m/s, though there was not mention of the pressures experienced.

In most explosions it is not possible to obtain real data such as maximum explosion pressures and flame velocities and those that provide data are primarily concerned with deflagrative combustion. However, in most instances the number of fatalities measures the severity of these explosions. Cybulska[23] gives examples of some of the worst coal dust explosions since the turn of the century. In all cases, the explosions were initiated by methane and the primary barrier did not work in all but one of the reported cases.

2.4 *Dust explosion characteristics*

Each explosion has characteristics that are measurable. These define the nature of the explosion in terms of its severity. Some of the explosion parameters associated with dust deflagrations are defined and related to dust explosion hazards. Parameters of interest are: -

- the maximum explosion pressure, P_{max},
- the maximum rate of pressure rise, $(dP/dt)_{max}$,
- the flammability or explosibility limits, and
- the minimum ignition energy *(MIE)*.

Some values for the parameters listed above are given in Table 2.1 -comparison of gas and dust explosions. For a more detailed review of dust explosions the reader is referred to a paper by Lee[24].

Sometimes referred to as the peak overpressure, the maximum explosion pressure, P_{max}, and the maximum rate of pressure rise, $(dP/dt)_{max}$, are used as indicators of explosion violence or severity. As such P_{max} will help in determining the strength of the explosion door.

Table 2.1 - Comparison of gas and dust explosions. Expanded from Bardon and Fletcher [25].

Characteristics	Gas explosions	Dust explosions
Type of explosion	Deflagrations or detonations	Usually deflagrations
Flame speed	Up to 3 km/s	Usually up to 10 m/s. In long galleries flames can accelerate up to 1 km/s and when detonations occur the flame speed can reach 2.5 km/s
Maximum explosion pressure	Same order of magnitude (typically 8 bar or less)	
Maximum rate of pressure rise	Usually greater for gases than for dusts	
Flammability limits	Usually narrow, but varies with material	Generally very wide, with upper limit several times stoichiometric concentration
Minimum ignition energy	0.2 – 10 MJ	10 – 40 MJ

The maximum rate of pressure rise, $(dP/dt)_{max}$, is a measure of the rate of pressure rise and is commonly expressed as the dust explosion constant K_{St}. K_{St} values are used to divide dust into dust explosion classes, Zeeuwen[26]; it provides a means of classifying the explosion severity of different dusts and has units of bar-m/s. With units of bar m/s, the dust explosion constant determines the speed of the explosion front. The cubic law commonly expresses the maximum rate of pressure rise.

The cubic law is usually written for gases as:-

$$\left(\frac{dP}{dt}\right)_{\max} V_0^{1/3} = K_G \qquad (2.1)$$

and for dusts:-

$$\left(\frac{dP}{dt}\right)_{\max} V_0^{1/3} = K_{St} \qquad (2.2)$$

Equations (2.1) and (2.2) are the cubic laws for gases and dusts respectively, where K_G is the gas-phase 'constant' and K_{St} is the dust constant. These two equations attempt to size normalise the maximum rate of pressure rise and thus provide a guide to venting requirements in vessels of different sizes.

Powel and Billinge[27] showed that maximum explosion pressures do not vary greatly from fuel to fuel under similar experimental conditions and are usually in the range 7 bar to 8 bar gauge when the initial pressure is atmospheric. However, its value depends on the expansion ratio, the greater the expansion ratio, the higher is the pressure for a given vessel filled with flame and combustible products.

Higher dispersing air pressures initially introduce higher burning rates in more turbulent mixtures whereas flame quenching is indicated by a decrease in the $(dP/dt)_{max}$. As the maximum explosion pressure should depend primarily on the amount of dust burned. The initial increase in P_{max} is due to the fact that more dust is raised into the suspension as the dispersing pressure increases and also the higher burning velocities associated with the more turbulent mixtures shorten the time of explosion.

As stated by Cashdollar[28], the lower (lean) and upper (rich) flammability or explosibility limits define the concentration boundaries within which a fuel/oxidant mixture will react explosively in the presence of an adequate ignition source.

For dusts, the lean limit, or minimum explosible concentration, is defined as the minimum concentration of dust in a cloud required to sustain a propagating flame. The upper limit flammability for a dust may not be reached in practise as it occurs at a much higher concentration.

Minimum ignition energy is defined as the least amount of spark energy required to ignite a flammable mixture. In practise it is applicable to cases of dust (as the explosion initiator, instead of methane) in relation to static electricity problems.

Minimum ignition energy and flammability limits are usually considered together due to the close association between flammability and ignitability. An ignition source must provide the flammable mixture with enough energy to enable the ignition of a dust-air mixture such that the rate of heat generation is higher that the rate of heat loss[28]. This is the condition necessary for self-propagation. The minimum ignition energy is thus the energy which must be imparted to the hot kernel for it to attain the critical size at which the flame propagates unaided. Thus an increase in minimum ignition energy with an increase in turbulence intensity is the net effect of two competing processes:-

- the enhanced burning velocity, leading to a reduction in the minimum ignition energy, and

- the increased rate of heat loss from the kernel to the surrounding unburned fuel, leading to an increase in the minimum ignition energy.

In studies for the determination of minimum ignition energy by Franke[29], and Skews and Law[30], a variety of ignition sources are used, such as friction sparks, and electrical sparks.

Minimum ignition energy is usually measured for the following reasons:-

- to determine the relative ease of spark ignition of a given dust compared with other dusts,

- to determine the hazard of spark ignition of a given dust,

- to determine the absolute minimum spark ignition energy of a given dust.

However, in underground mining environments explosions are initially caused by methane with propagation of the explosion front sustained by coal dust.

Table 2.1 provides a summary of some of the significant differences between gas and dust explosions characteristics.

The previously defined explosion parameters (P_{max}, $(dP/dt)_{max}$, flammability limits and minimum ignition energy) are all affected by turbulence according to Amyotte et al[31].

Turbulence generation can arise from flowing gases from a primary explosion, which can lift layered dust off surfaces. This forms a turbulent dust/air cloud. Should this mixture ignite and continue to propagate, lifting dust as it does so, a self-sustaining deflagration (secondary explosion) may be achieved, and indeed this is the case with most underground coal mine explosions. Turbulence and its effect on explosions are discussed below.

The flame propagation rate is not commonly measured in explosibility testing. However, it is pertinent to discuss the influence of turbulence on this parameter. Flame propagation rate has a pronounced effect on other explosion characteristics, particularly, the maximum rate of pressure rise.

Flame propagation can be enhanced by pre-ignition turbulence during a confined explosion, as demonstrated by Lunn and Roberts[32]. In accounting for the behaviour of coal dust explosions they suggested that a reason for low values for the 'burnt gas temperature' could lie in the fact that coal dust was not sufficiently mixed with the air to give uniformity. A form of pre-ignition turbulence was suggested where the coal dust could be distributed across the diameter of a gallery quickly by large turbulent eddies. Once the coal dust particles are lifted, they are then carried along by the turbulent eddies.

Several researchers have investigated the role of turbulence in the explosion process. Laminar burning flame velocities depend on the transport and chemical-kinetics properties of the gas mixture. However, flames are intrinsically unstable to most disturbances in the flow field so that the burning rate is also strongly influenced by the gas-dynamic flow of the unburned gas. Flame structure can in turn be strongly influenced by obstacles. Thus the presence of obstacles gives rise to distortions of the flame. Walls, connecting ducts, and vent openings all act as effective generators and as turbulence is produced, the burning velocity increases. This in turn increases the upstream velocity. This can continue with an ever-accelerating flame front. In experiments to determine the maximum flame velocity when obstacles are placed in the path of a flame front, results showed that there can be increases of up to a factor of 24 compared to when there are no obstructions.

Flame acceleration due to obstacles in the path of a propagating gaseous flame front has been demonstrated by Moen et al[33] and Hjertager[34]. Similar considerations apply for dust deflagrations, as illustrated by Lunn[35] who states that an obstacle can cause a rapid transition from deflagrative to detonative combustion during a dust explosion.

An explanation for obstacle-induced flame acceleration is provided by Alexiou et al[36] through empirical evidence from gas-explosions in long vessels. Obstacles in the form of single-hole orifice plates were placed in a long vessel. When the flame enters the turbulent flow region established by the obstacle it becomes stretched and folded as the hot combustion zone is distorted and entrained into the wakes by the action of large-scale eddies. An enhanced rate of burning and a higher burning velocity result from the increase in flame surface area. Small scale eddies which may be present in the wake are assumed to contribute to heat and mass transport across the flame surface. The higher burning velocity increases the flow velocity in the unburned mixtures creating more turbulence which leads to a further increase in burning velocity and so on. With periodic obstacle spacing the positive feedback mechanism or coupling between the flow dynamics and the burning velocity leads to rapid flame acceleration. This is of concern in mine galleries where machinery may be considered as turbulence-inducing obstacles should an explosion occur.

2.5 Shock waves

Whilst it has already been stated that the explosibility of dust is dependent on ignition source, chemical composition and nature of the coal, concentration of coal dust, and size distribution of the dust amongst others, Lebecki[37] showed that the creation of a shock wave is related solely to the necessity of adhering to the mass conservation.

It is the shock wave that raises the dust as well as making it possible to control explosions by triggering active/passive barriers. [These barriers are the subject of the next chapter]. The influence of reflection from the open end has been less than that from obstacles. In tests, the shock wave travels at more than twice the speed of the flame. From observations the reflected wave behaves like a quasi-rigid obstacle. [note that a

shock wave that has passed a barrier has a reduced speed and intensity as does the flame].

Shock waves are discussed in detail in chapter five.

2.6 *Numerical modelling of explosions*

Although the primary objective of this study is the flow through the explosion door and thus the ability of the door to withstand a shock wave, it is worth giving a brief overview of the various explosion modelling Computational Fluid Dynamics (CFD) software which is available commercially. One such overview of the commercial codes available has been done by Popat et al[38]. These codes are different in their numerical approach to solving the governing equations and the equations solved. However, it would seem that these codes offer a high degree of accuracy but there are some differences in their combustion, turbulence and drag models. For more detailed information, the reader should consult this study.

There are CFD codes capable of modelling underground fires as shown by Lea[39]. A network model, MFIRE, from the US Bureau of Mines is capable of predicting the altered ventilation, transport of heat and fume contaminants in the event of fire. However it assumes that smoke and hot gases are uniformly mixed across a tunnel cross-section. In modelling, the mine is considered to be comprised of a series of closed circuits of airways, which intersect at junctions. The conservation equations are constructed and solved iteratively using the Hardy-Cross algorithm with fire being modelled as a constant source of heat.

The Gravity Current model[40] predicts time-dependent growth and breakdown of the hot current in the presence of a background ventilation flow. It works by firstly finding the entrainment of ambient air into the fire and then given a supplied fire size (in MW), initial temperature, depth, and velocity of the downstream and upstream gravity currents are calculated. The one-dimensional forms of the energy and momentum equations are integrated over a small downstream distance from which the new downstream values for current depth, velocity and temperature are predicted. An account is made of the heat

loss to the walls, that due to wall shear, cooling due to entrainment of ambient air, and drag due to this entrainment in the latter stage. When the gravity current and associated shear-layer have grown to fill the tunnel or have come to rest, the model is stopped.

CFD codes such as Fluent and FLOW3D are capable of simulating turbulent flow and heat transfer. The conservation equations are solved using the 'SIMPLE' iterative algorithm developed by Pantaker[41] and turbulence is modelled using the k-ε model.

In dusty environments, the nature of the decay of the shock wave is governed by the size of the dust particles in the air. Investigations by Suzuki and Adachi[42] have showed that the blast wave over the dust layer decays faster than in a dust-free gas, with the particle size, having an effect on the rate of decay. The onset of an explosion in an underground mining environment leads to the creation of a shock wave and several researchers have investigated this.

Skews and Law[43] investigated the behaviour of a shock wave propagating through a system of branched ducts such as those that can be found in underground mining environments. Using a model of an underground mining environment in a shock tube, they discovered that the flow through the tunnel was complex. This complex flow pattern was captured. Using Schlieren photography allowed the tracking of the shock waves in the tunnels.

2.7 Blast modelling

Van den Berg and Van Wingerden define a deflagrative gas explosion[44] as a process of combustion-driven expansion flow in which the turbulent structure of the flow acts as an uncontrolled positive feedback. The consequence is that a turbulence-generating environment is required for the development of explosive, blast generating combustion. This determines the concept of a vapour cloud explosion that underlies the method of blast modelling.

A blast produced by a gas explosion can be modelled using TNT[i]-equivalency methods. This method uses TNT-blast data to represent the blast properties in the vicinity of an explosion. However, inaccurate results can be generated and in order to improve accuracy, Van den Berg et al[30] have applied the Multi-Energy method.

The Multi-Energy concept states that a blast is generated in a vapour cloud explosion only in the parts of the vapour cloud which are obstructed and/or partially confined and that the unobstructed and/or unconfined parts of the cloud hardly contribute.

In experimental situations TNT-blast data is used but its use has proved unsatisfactory and thus fuel-air charge blast data are used to model blast effects from gas explosions.

2.8 Conclusion

This chapter has reviewed dust and gas explosions. Useful parameters that determine the severity, maximum explosion pressures, flammability or explosibility limits, and the minimum ignition energy have all been defined and how turbulence affects them has been discussed. In order to better understand explosions in underground tunnels, some researchers conducted small scale explosions in shock tubes. These revealed rather complex flow patterns.

In the comparison of gas and dust explosions, the main differences between the explosions caused by them was showed to be the existence of one phase in gas explosions. However, the pressures that determine the severity of the explosion were showed to be similar for gas and dust explosions though the energy need to initiate the former was lower. The ability of coal dust to ignite was showed to be dependent on the particle size.

Though this chapter has given a brief review of gas and dust explosions, in front of these explosions are shock fronts. It is the behaviour of the shock wave preceding the flame front that is of primary concern in this research. The next chapter discusses current methods for arresting the explosions discussed here.

---

[i] Symmetrical 2, 4, 6-trinitrotoluene – an explosive

CHAPTER 3 Current methods for arresting underground explosions

3.1 Introduction

The previous chapter dealt with the initiation of underground mining explosions by methane and its subsequent propagation. It showed that explosions may vary in strength and thus arresting devices must be such that they can perform under all conditions, especially as an important consideration in mine safety is the suppression of an incipient coal dust explosion.

This chapter reviews arresting devices currently used in underground mining environments. The advantages and disadvantages of these devices will be highlighted and a novel method for arresting explosions will be introduced. This novel barrier will have all the advantages of the current systems as well as acting as a last line of defense further away from the source of an explosion should the primary barriers fail in their operation.

3.1.1 Explosion protection underground

In the mining industry numerous research on underground explosions has been carried including some publications and books on the subject[45, 46, 47, 48]. The researchers in Poland, Germany, and the United Kingdom sought to improve the safety of miners and mines in coal producing countries due to the need to mechanise coal mines and improve productivity.

This lead to the categorisation of methods for arresting explosions in underground coal mines: -

- Preventive measures, and
- Constructive measures.

Preventive measures seek to stop the explosion from taking place and are divided into two activities. One type of preventive measure is that to neutralise coal dust particles, and the other is that against the onset of an initial explosion from methane.

In the former category, there are two main measures against methane build-up – extraction and ventilation measures. With coal dust, activities such as watering, water-sprays, stone dust spreading, hygroscopic dust binding, and dust extraction are all measures that have been adopted to prevent the initiation of an explosion. For preventive measures against coal dust initiated explosions, inert materials such as water and stone dust based are usually used. These inert materials are spread liberally over the roadway floor such that if a methane ignition occurs, the mixture of coal dust and stone dust that is thrown into the air will not ignite. Though such preventive measures aim to stop the propagation of an explosion, they are rather difficult as shown by the accidents that do occur. Most research effort has been concentrated on constructive measures to prevent explosions underground.

Constructive measures on the other hand are meant to supplement the preventative measures and may take the form of explosion barriers or explosion-proof components. (See Figure 3.1- Measures of arresting underground explosions)[2]. In most mining environments a third category can be added; those using special structures like shelters to protect occupants in a mine during an explosion. Associated with these are materials used in arresting the explosions as well as their modes of operation. Explosion barriers can either be active or passive though most mining environments are equipped with active barriers with water or stone dust as the extinguishing medium.

Ventilation of underground mines is usually through the distribution of adequate airflow to the various locations to rapidly dilute pollutants that are being emitted. This goes on until concentration levels are harmless, though Cybulski[49] produced some equations to relate coal dust explosibility to the volatile content, fineness, inert content, and free water content. These equations are applicable when the volatile matter is the range of 15% to 40% and were deduced for conditions when the coal can be dispersed easily (placing the coal dust on roof bars) and when it is difficult to disperse the coal dust (when it spread on the floor). These equations were corroborated with experimental data to determine

their correctness. Along with methane extraction, there have been investigations by Cybulska and Cybulski[50] into the placement of water barriers close to the methane zones as methane is usually the initiator of coal dust explosions.

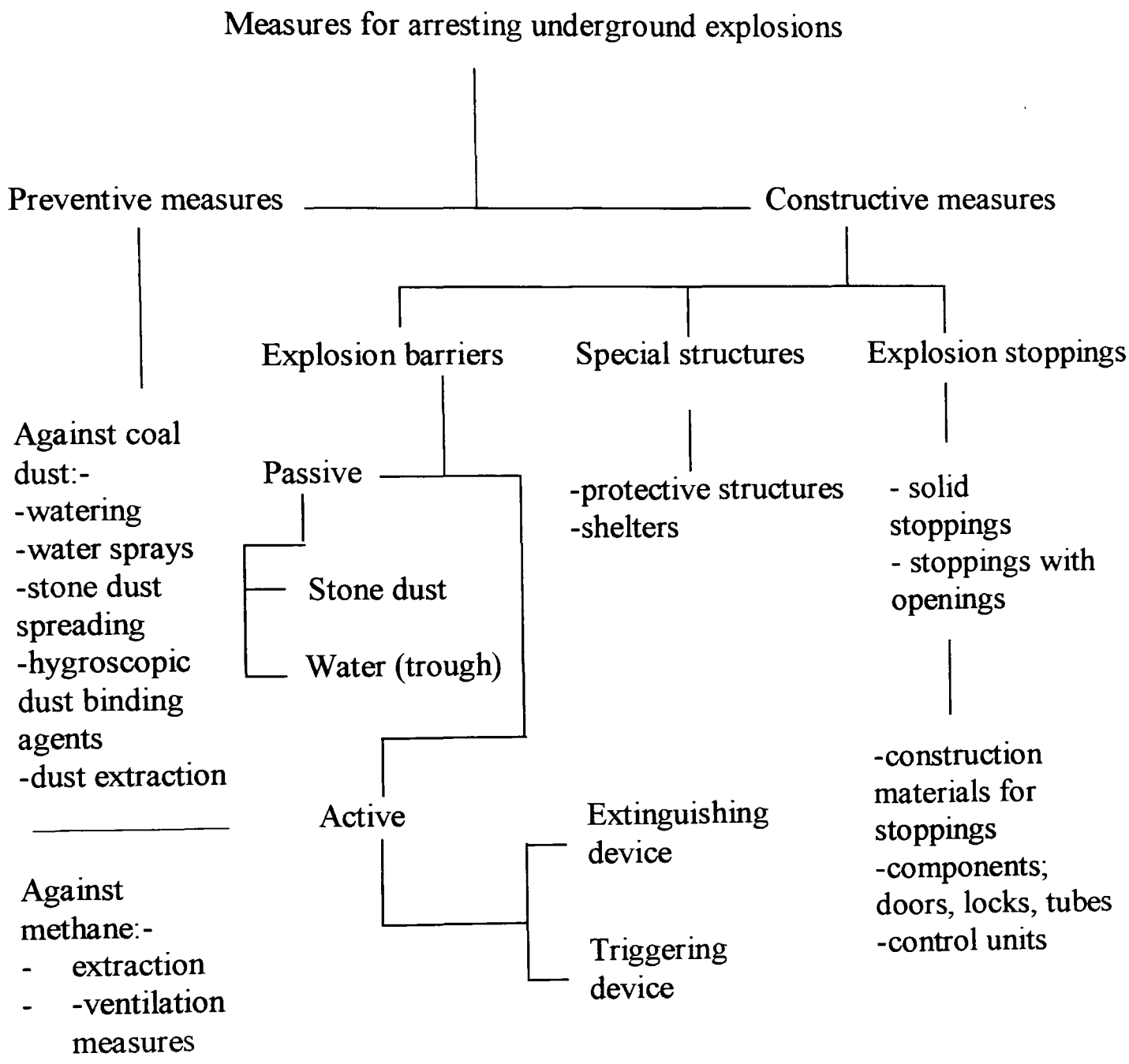

Figure 3.1 – Measures for arresting underground explosions.

The requirements, which determine the likelihood of an explosion, and the necessary steps, which must be taken, are given in Table 3.1: -

Table 3.1 - Adapted from The Mines and Quarries Acts (1954)[5].

Methane content (percentage in air)	Action to be taken
1.25	switch off electrical power
2.00	withdraw men
9.60	Methane is at its most explosive

3.2 Current barrier systems

3.2.1 Passive barriers – General

United Kingdom mining law states that every underground mining environment requires passive barriers. Installation problems can occur in tunnels containing a large amount of mining equipment such as overhead rail conveyors, and compressed air pipes. There are two types of passive barriers; stone dust and water barriers, Cybulski[51, 52].

These kinds of barriers may fail if the explosion is too weak; where the blast waves cannot dislodge the shelves containing the inert material. They may also fail if the flame speeds exceed 500 m/s; where the delay between the pressure front and the flame front is very short and also if the flame may have passed before dispersion of the inert material is complete. Whilst in most instances there may be only one explosion, there are times when a second explosion may take place. According to some investigations by Meerbach and Michelis[53] the time interval between these multiple explosions can range from a few minutes to several days, thus the likelihood of an explosion is reinitiated after an initial explosion is an important issue that cannot be ignored. The performance of the primary barriers are crucial as failure can usually result in a sizeable increase in the maximum pressure of the explosion as well as the speed with which the flame travels.

3.2.1.1 Passive stone dust barriers

These barriers consist of a series of planks of wood suspended from the roof of the tunnel on which are placed a predetermined quantity of stone dust. Being passive, they are designed such that the blast force from an explosion tips them.

As mentioned in section 3.1.1, preventive measures are used in combination with these barriers. The combustible coal dust can be diluted with an inerting chemical such as rock dust (Calcium Carbonate). In a coal mining operation, the rock dust is applied to the entry roof, ribs and floor. Should an explosion be initiated, the rock dust would be entrained along with the coal dust into the air stream. The dispersed rock dust acts as a thermal sink, with the transfer of thermal energy by conduction and convection, and as a means of blocking radiant energy transfer to the coal particles, thereby inhibiting the propagation of the coal dust explosion, Edwards and Ford[54].

More tests by Liebman and Richmond[55] have been conducted to determine the effectiveness of other extinguishing agents used in underground mining environments. These agents were ranked on their chemical inerting ability as well as the quantity required to arrest a propagating explosion. Ammonium Dihydrogen Orthophosphate ($NH_4H_2PO_4$) was the most effective with Calcium Carbonate ($CaCO_3$) the least effective. This is poignant as $CaCO_3$ is widely used as the inerting material in most underground mining environments.

3.2.1.2 Passive water barriers

According to Hinsley[56], the use of water as a suppressant is attractive for several reasons: -

- it is a traditional fire-fighting material,
- it is cheap and does not deteriorate in storage, but is likely to evaporate,
- there are several possible modes by which water extinguishes: a reduction of oxygen content, cooling by latent heat and cooling by thermal capacity, and

- in decomposition by combination with carbon, water does not produce any toxic compounds that are present in the explosion.

Passive water barriers are usually plastic containers filled with water supported by chains or placed on shelves. Here, the blast wave ruptures or overturns the water containers and thus disperses the water into the path of the flame. They are also classified according to the location of their installation and the quantity of water they contain, Sapko et al[57]: -

- concentrated passive water barrier: - designed to produce a dense cloud of water droplets in a relatively short length of roadway.

- distributed passive water barrier: - designed to produce a less dense but effective cloud of water droplets over a longer roadway.

Thus for concentrated water barriers, many countries have adopted a 200 l/m^2 of water loading and 1 l/m^2 of water has been adopted for distributed barriers.

In general, passive water barriers need higher speeds to perform satisfactorily as revealed by Liebman et al[58], due to the fact that a weak explosion might not produce enough force to rupture or tip the water containers. However, to overcome this failing, novel passive barriers have been designed by researchers at the US Bureau of Mines for stopping dust explosions propagating at speeds as low as 25 m/s. [See Figure 3.2 for typical layouts of passive water barriers].

3.2.2 Active barriers

Quite often an explosion starts as an almost pressureless inflammation of methane. Thus a passive water or stone dust barrier might not extinguish the explosion in its incipient stage. Also active (triggered) barriers came into prominence due to the problems encountered in the use of passive barriers, especially their inability to fully arrest an explosion which might be weak or violent. In order to fill this gap, active barriers were developed. They are also used where space is at a premium. However, there are some

minor drawbacks as tests carried out by Kawenski et al[59], have highlighted excessive noise generated by active barriers during dispersion of the quenching medium (powder in this case), though this is a not a concern when the primary issue is that of an explosion.

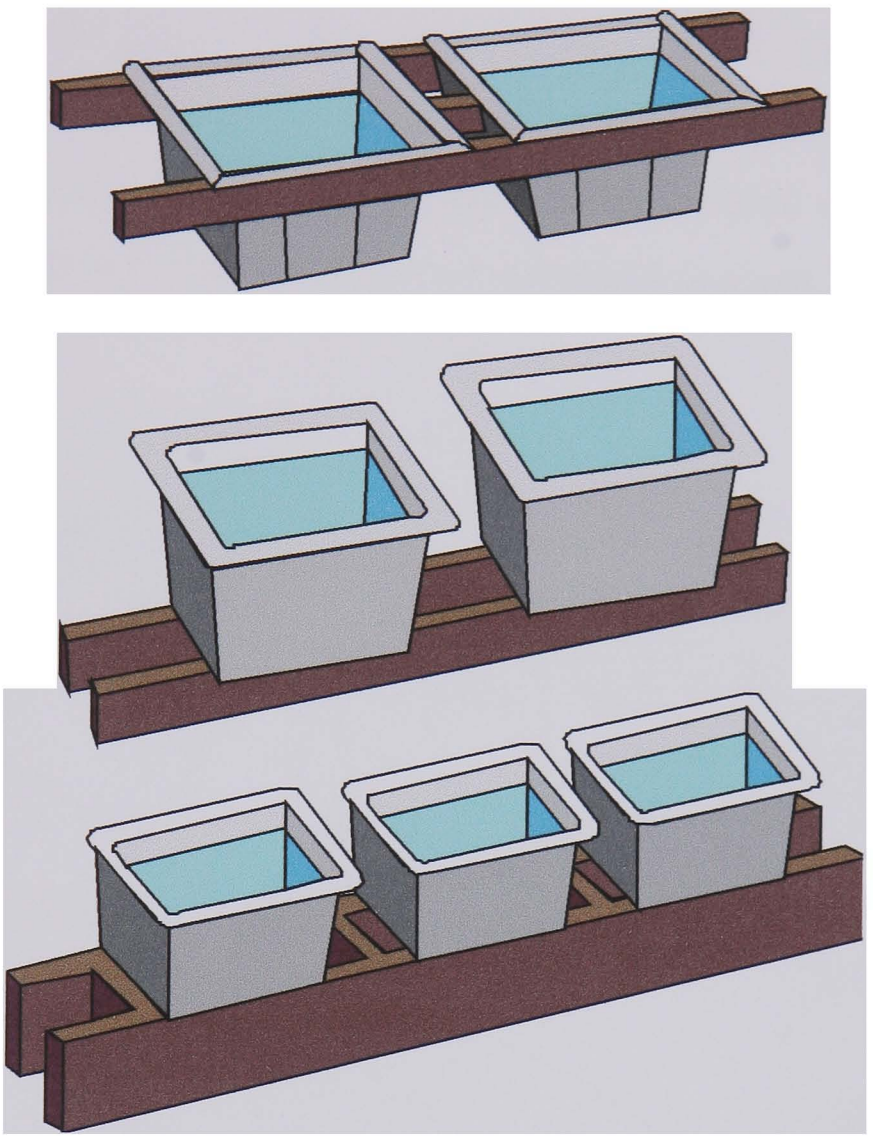

Figure 3.2 - Arrangements of passive water barriers.

Active barriers consist of two main units, the dispenser and the sensor. The dispenser discharges the inert material (nitrogen or carbon dioxide are often used) by means of a compressed gas, spring or explosive material. A sensor device detects the on-coming explosion by a rise in static pressure, temperature or radiation and triggers a mechanism to activate the dispenser.

Fisher and Cohen[60], and Jones and Bott[61] have all showed that in active barrier research, triggering components are the most important part. This is particularly true as response time, location of the sensor, and the detection of toxic gases which signal the imminent arrival of an explosion in relation to the positioning of the explosion barrier

dictate whether the explosion is extinguished or not. There are several methods used in the detection of the flame. Prominent amongst these are optical methods which have been used in the region of wavelength of electromagnetic radiation - UV-C region as shown by Faber and Scholl[62]. Such systems are chosen with regard to lighting conditions underground where they can be adjusted to suit the local environment. Cortese and Sapko[63] revealed that solar powered triggering devices have also been developed which use ultraviolet radiation from the developing explosion to generate electricity which can then be used to trigger an extinguishing agent. See Figure 3.3.

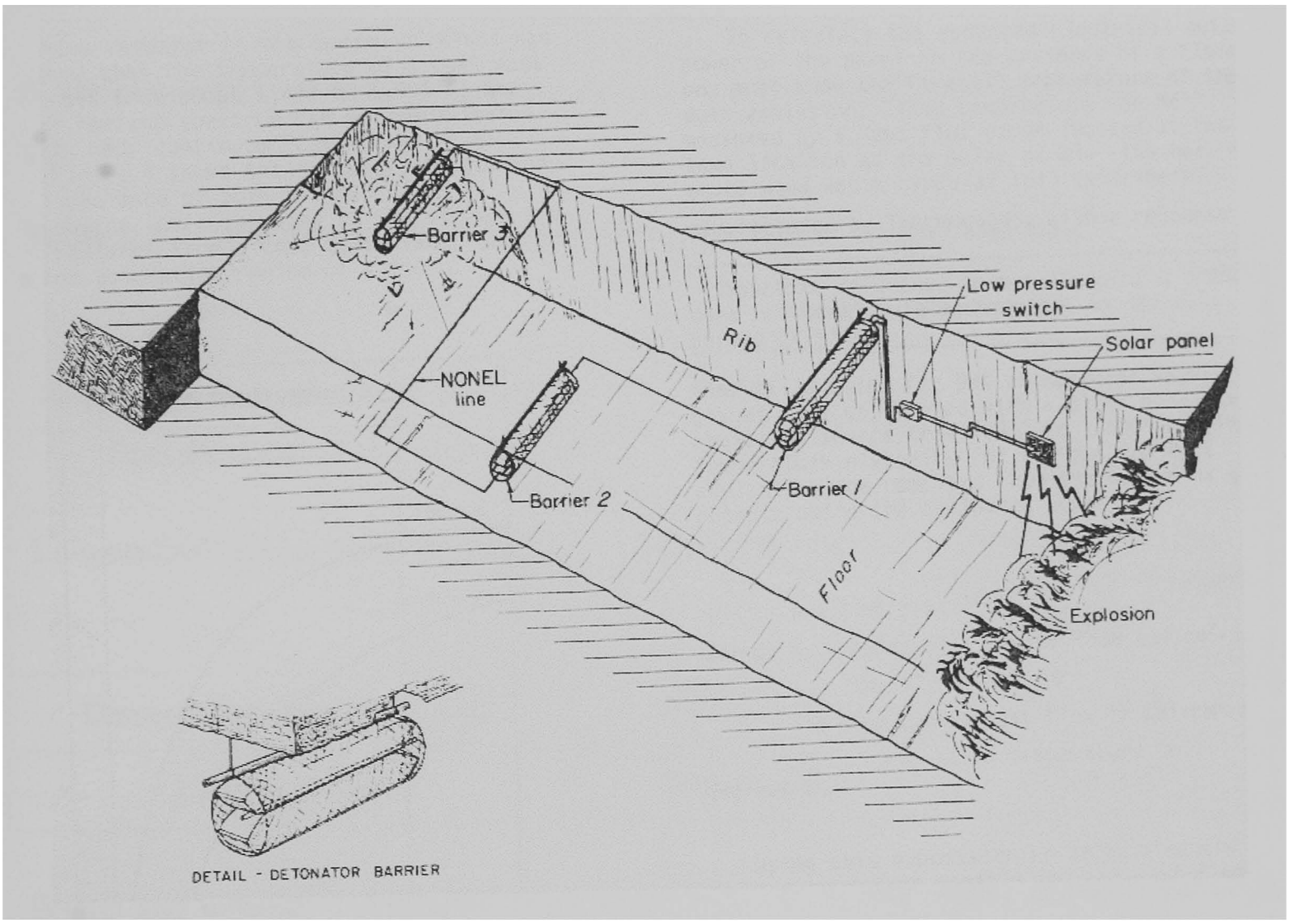

Figure 3.3 – Typical layout of an explosion barrier.

Cybulski[64, 65], was prominent in the research on triggered barriers, especially on their effectiveness when the type of explosion is weak or strong.

Further research by Michelis[66] on sensing methods for active barriers have been conducted using thermo-electric sensors. These barriers could be used both with stationary and mobile carriers making them easy to use in underground mines. The inert

material was a conventional water trough. Water is used in preference to stone dust barriers as it has many advantages such as reduced quantity of extinguishing agent, it is available in most underground mines; negating transportation problems, better behaviour against explosions, and ease of maintenance. Triggered water barriers are being developed as they can work in a variety of explosions, from pressureless inflammation of methane to violent explosions. Triggered barriers use a lower specific quantity of water compared to passive systems. In fact, in a direct comparison with stone dust barriers, Cybulski[67] found that active water barriers were more effective on an equal volume basis.

A useful comparison between passive and active water trough barriers is given in Table 3.2.

Table 3.2 – Characteristics of passive and active water trough barriers[57].

	Water trough barrier	
Requirements on explosion barriers	Passive	Active
Specific quantity of water	200 l/m^2	80 l/m^2
Longitudinal arrangement of troughs	1 trough/group	25% related to the whole number of water troughs
Distance between the troughs	Max. 1.2 m	Max. 2.5 m
Length of barrier	About 15 m	About 5 m

Winter and Giltaire[68] conducted experiments in a 145 m long gallery of cross section 8 to 12 m^2. These experiments were conducted to determine the effectiveness of conventional barriers (rock dust or water) and triggered barriers subjected to dust explosions of different strengths. In order to mimic conditions underground, obstacles (to replicate mining machines) were placed in the gallery. It was later found that these equipment did not hinder the effectiveness of the triggered barriers as compared to the conventional barriers.

Piezoelectric pressure gauges and flame detectors observed flame development. For ignition sources, it was found that ignition of methane by rock explosives gave the largest increase in pressure (2 bar absolute) and subsequently the highest flame velocity (up to 160 m/s). Ignition of coal dust produced flame velocities up to 100 m/s and a maximum pressure in the order of 1.4 bar (absolute). Methane ignited by 10 g of black powder[ii] produced flame velocities up to 80 m/s and a maximum pressure of the order of 1.25 bar (absolute).

Table 3.3 shows the types of barrier used in their experiments, the extension of the flame and time between the air blast and the flame front. The rock dust or water barriers showed the same effectiveness against the explosions. However, with more violent explosions, the 40 l tubs arrested the flame at 140 m instead of 105 m, as was the case with the 80 l tubs or rock dust platforms.

The detector for the triggered barrier used the UV radiation from the flame and its ability to work effectively depended on its location. Quenching agents were Sodium Bicarbonate, Limestone or Monoammonium Phosphate.

Whilst most in the literature test for the efficiency of barriers in a constant area tunnels, Meerbach[69] conducted some tests on the performance of water barriers in a region where there is a change in cross-section. Tests were carried out in such a way that the explosion could be initiated in the smaller area with the barriers initially placed in the smaller area and then in the larger area. The change in area was 2 m^2. Initial tests were conducted with flame speeds between 100 m/s and 200 m/s, where the passive barriers used could easily arrest the flames created by the explosion. However, placing mining equipment in the test region; conveyor belts, and increasing the strength of the explosion found that at relatively mild explosions, the obstructions did not have a significant effect on the performance of the barriers. With flame speeds in the region of 200 m/s to 300 m/s corresponding to pressures of 2 bar, the performance of the barriers were sensitive to its position within the mine – good when positioned below the obstruction, or when

---

[ii] There is no definition of this 'black powder' in the literature. It is assumed to be gun powder.

the barriers were placed much lower from the ceiling. Increasing the concentration of the extinguishing agent also contributed to the successful arrest of the flames.

Table 3.3 – Performance of water barriers and stone dust barriers.

Ignition source	Type of barrier	Quantity of water or rock dust (litre, l)	Flame velocity at barrier (m/s)	Δt[iii]	Extension of the flame (m)
Coal dust dispersed and ignited by explosive	80 l tubs, 40 l tubs, Rock dust platforms	1000	70 – 100	0.9 - 1.3	105
60 m^3 with 10% CH_4 ignited by 200 g explosive	80 l tubs, 40 l tubs, Rock dust platforms	1000	80 – 160	0.6 - 0.9	105 140
60 m^3 with 10% CH_4 ignited by 10 g black powder	80 l tubs, 40 l tubs, Rock dust platforms	500	20 - 80	1.2 - 3	90 - 105

3.2.2.1 Disadvantages of active barriers

They are expensive and complicated devices. However, their most significant disadvantage is that they have to provide precise matching of an explosion flame and the inert material cloud. If the cloud is formed too soon it will be carried along by the pressure wave ahead of the flame front, and if formed too late the flame front will have passed and the barrier will have no effect. In his review of explosions in Poland, Krzystolik[17] revealed that in explosions where the barriers were not effective, the path of the flame was nearly 2 km long. Thus a novel barrier for arresting explosions placed further away from the source could successfully arrest such flames. Table 3.4 gives more details of active barriers and their properties: -

[iii] Time between the arrival of the air blast and the flame front at the barrier

Table 3.4 - Barrier Types.

Type of barrier → Properties ↓	US Bureau of Mines Low Pressure Dispenser	SMRE MKII Triggered Water Barrier	Belgian Triggered Barrier System	SMRE Triggered Stone Dust Barrier
Shape	Spherical Vessel	Two part cylindrical vessel	Cylindrical vessel made from polyurethane, dispenser is made from PVC	Rectangular tubs made from plastic
Dispersing material	70% filled with water	One section is filled with water	Dispenser is water filled	Stores about 25 kg of stone dust
Method of drive	Void pressurised with nitrogen	One section contains compressed nitrogen		Energy required to activate the dust is stored in a compressed and wound coil spring
Activation method	Water released through a 7.6 cm wide diaphragm and a multiple nozzle or a 7.6 cm diameter pipe	the two parts are separated by an explosive charge and detonators which are fired electrically by a signal from the sensor	Explosion is detected by a thermochemical sensor	Use a rise in static pressure as the trigger mechanism. The pressure-sensing device is connected to the center pivot of the trigger mechanism.

3.3 New active barrier - Explosion-proof door

Safety in mines continues to be improved, minimising the risk posed by the leakage of methane and coal dust, through methane drainage and the use of passive and active barriers continues. However, as was mentioned earlier, there are still incidents when these barriers fail to arrest explosions. Thus in light of the shortcomings of the current barrier systems, a new technique as revealed by Dixon et al.[70] for arresting explosions in

a underground mining environment is being proposed and is the subject of this research project. This explosion barrier (see Figure 3.5) can be described as an explosion stopping device with openings - as defined by the explosion protection underground diagram in Figure 3.1.

The explosion door consists of a sensor, a release mechanism, and the door unit. The explosion door is not meant to replace current barriers but rather to supplement them. As such it will be placed about a kilometre from the coal face as research has revealed that should the primary barriers fail in their operation, the flame front behind the explosion can travel over 2 km.

Underground mining environments contain other ancillaries thus in designing the barrier system; attention is paid to the auxiliary equipment used in mines. The explosion-proof barrier can be used with overhead rail, railway and conveyor transportation with some measures, these are: -

- monorail (overhead) systems - designed in such a way that they can be attached/released separately from the door frame
- railway transport - closure of one door must not be impeded during transport in case of an explosion. This is dependent on the distance between the two doors.

The sensing mechanism is shared with current active barrier systems: a sensor picking up a rise in static pressure caused by an explosion. The sensor then triggers a mechanism, which causes the door to be closed in a specially constructed frame. The doors are of special construction and consist of suitable material with certain properties (good thermal conductivity and strength) having holes small enough to stop the flames but big enough to allow the pressure wave to pass through without damaging the door. The operation of the door is such that it does not interfere with tunnelling activities or equipment.

The main advantages with this door barrier are that: -

- it is relatively less complicated than triggered water and stone barriers,
- it will be easy to manufacture and requires little maintenance after installation, and

- it supplements current arresting devices.

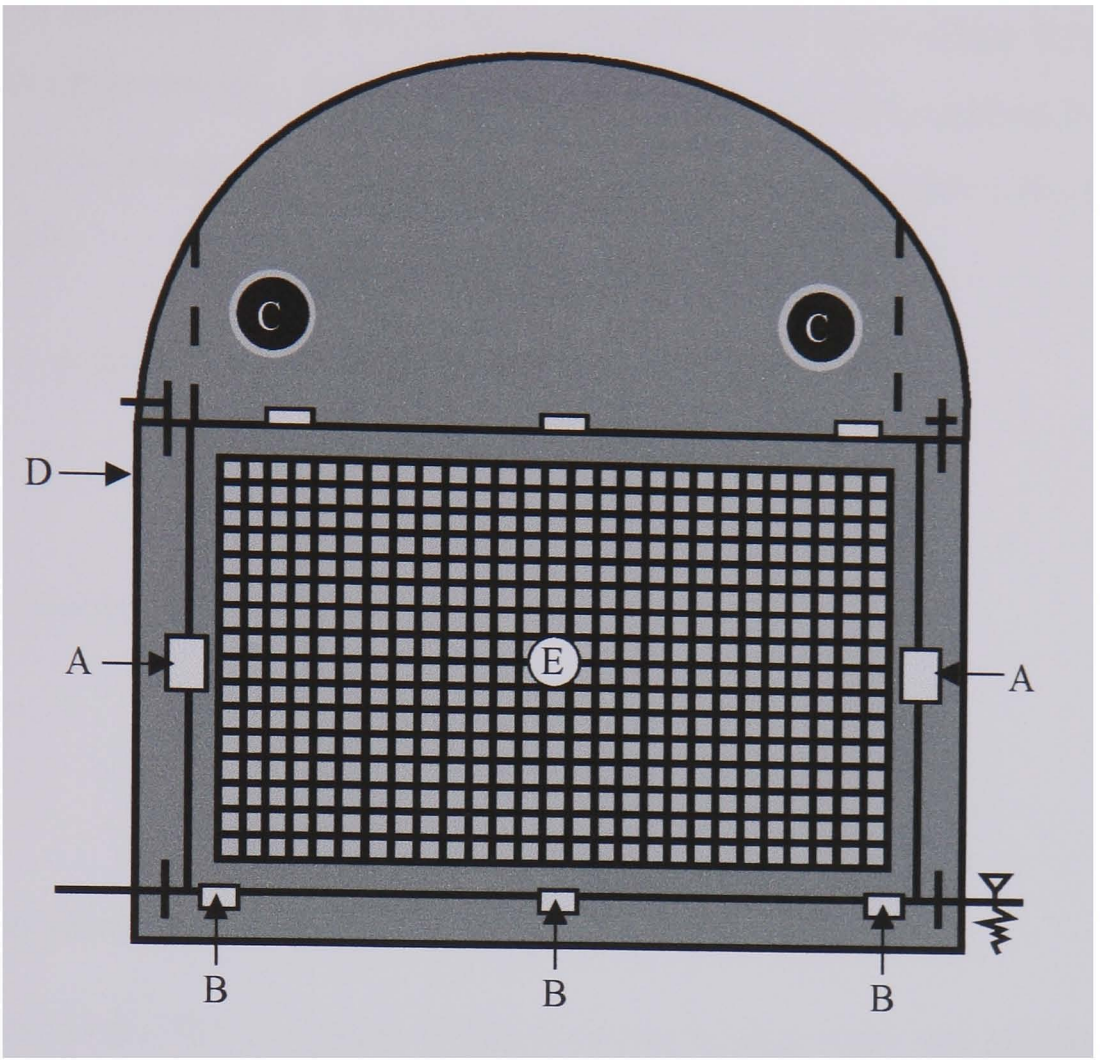

Figure 3.4 - Front elevation of the explosion door. Where A & B are the locking mechanism, C are for services (e.g. pipes), D is the door frame, and E is the individual flameproof sandwich components – porous material.

3.3.1 Active door properties

The idea of an arresting explosion-proof door is not new. Michelis and Kleine[2] conducted some experiments in accordance with German standards on structures used in underground mining environments. These structures were subjected to static pressures of 1 MPa. Of interest were tests conducted on a domed explosion-proof haulage door. Domed panels were used instead of plane panels, as the latter type could not withstand the stipulated pressure of 1 MPa. It is worth noting that, this explosion door did not allow the passage of a shock wave that would normally be preceding an explosion in a mining environment.

However the explosion-proof door reported in this thesis contains a porous media which will allow the passage of the shock wave but arrest the flame front which would be travelling behind the shock. In fact, this idea has been used in Liquefied Petroleum Gas (LPG) systems to prevent back firing and in safety lamps to cool down the lamp flame in a gaseous media.

The explosion door is made up of three units: -

- the Sensor,
- the Release mechanism, and
- the Door.

3.3.1.1 The sensor

A sensor selected for the operation of the door mechanism must not require any energy for operation and must be simple. As reported earlier, there are sensors currently in use for active barriers and these can be used for the operation of the explosion door.

3.3.1.2 The release mechanism

A signal from the sensor activates the door mechanism and allows it to fall under gravity until it hits the door frame. The mechanism consists of a drum, gear, wire etc. (See Figure 3.5). The distance between the sensor and the door can be a considerable distance away and linked electronically to the release mechanism.

3.3.1.3 The door unit

The unit consists of a flame proof door, the door frame, and the locking mechanism. The door is constructed such that it will allow passage of the flame and are designed to resist maximum dynamic pressure from the explosion. Securing the door upon closure is a locking mechanism. The door closes against a frame made up of four blocks, connected

together using bolts and insulating materials. Auxiliary equipment such as pipes and cables are placed through these blocks. To ensure total arrest of the flame, the barrier system comprises at least two explosion-proof doors placed at an appropriate distance apart.

Within the explosion door will be the porous material that will reduce the strength of the shock wave that precedes an explosion, but arrest the flame behind the shock.

The performance of the porous material is the subject of the research. The porous material used will be discussed in chapter five.

Figure 3.5 outlines the components of the door.

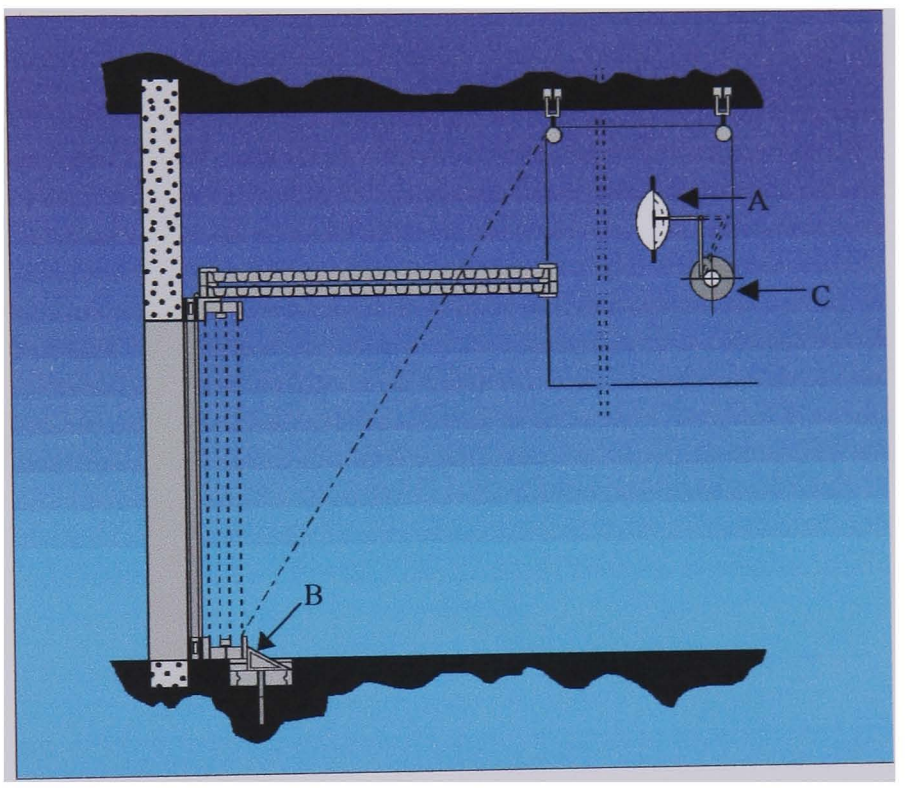

Figure 3.5 - Side elevation of the explosion door. Where A is a sensor, B is the locking mechanism, and C is the pulley and wire for the door release.

Figure 3.6 to Figure 3.9 show the proposed explosion door in situ and its methodology for arresting an explosion.

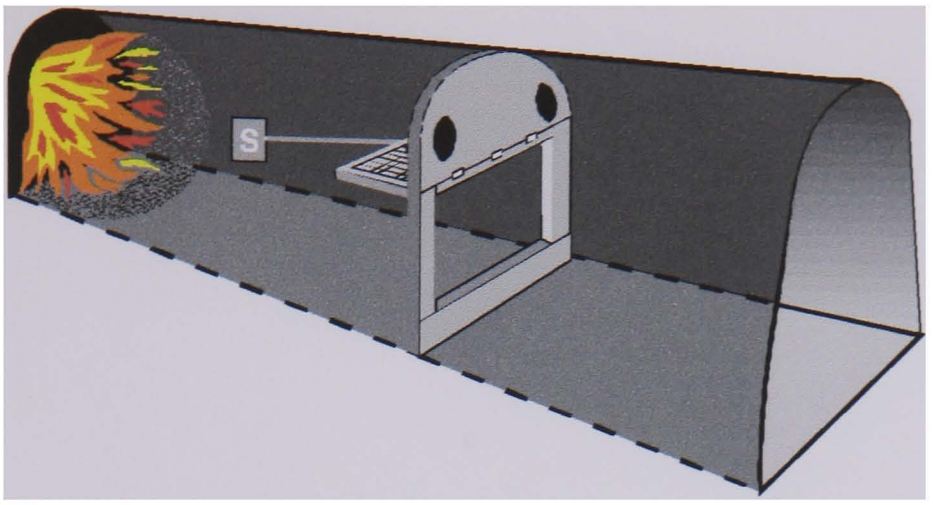

Figure 3.6 - Explosion approaching sensor.

In Figure 3.6, the explosion door is shown as it would be installed in a mining environment. It is placed a distance away from the source of the explosion, which would be travelling as a high-speed wave with a flame front just behind the wave. The sensor is in place to detect the pressure wave.

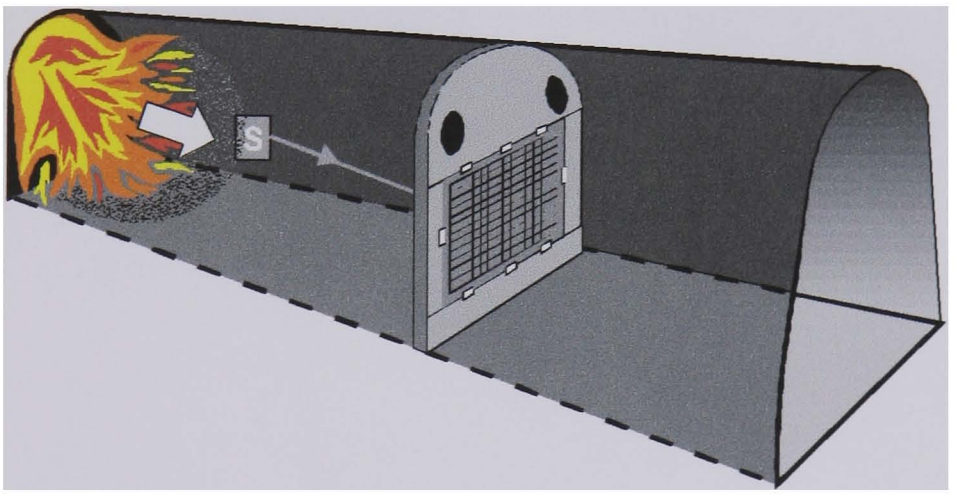

Figure 3.7 - Sensor triggered.

On detection of the pressure wave (Figure 3.7), the release mechanism allows the door to fall under gravity until it hits the door frame.

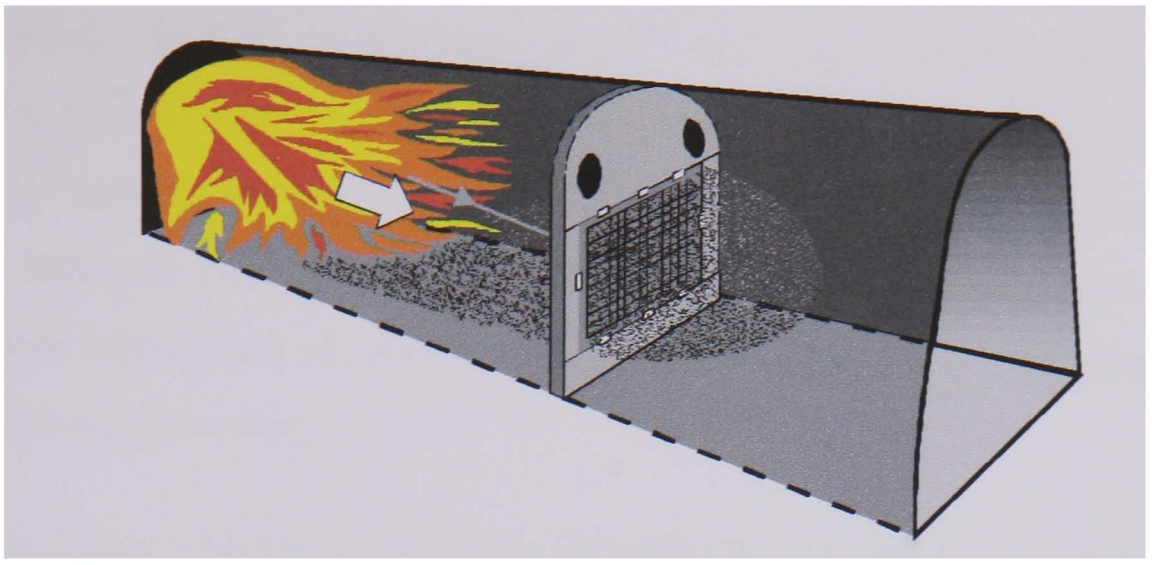

Figure 3.8 - Pressure wave passing through perforations.

The pressure wave then passes through the explosion door (Figure 3.8). The permeable barrier will be designed such that the pressure drop across the door would not inflict structural damage that would render the door ineffective.

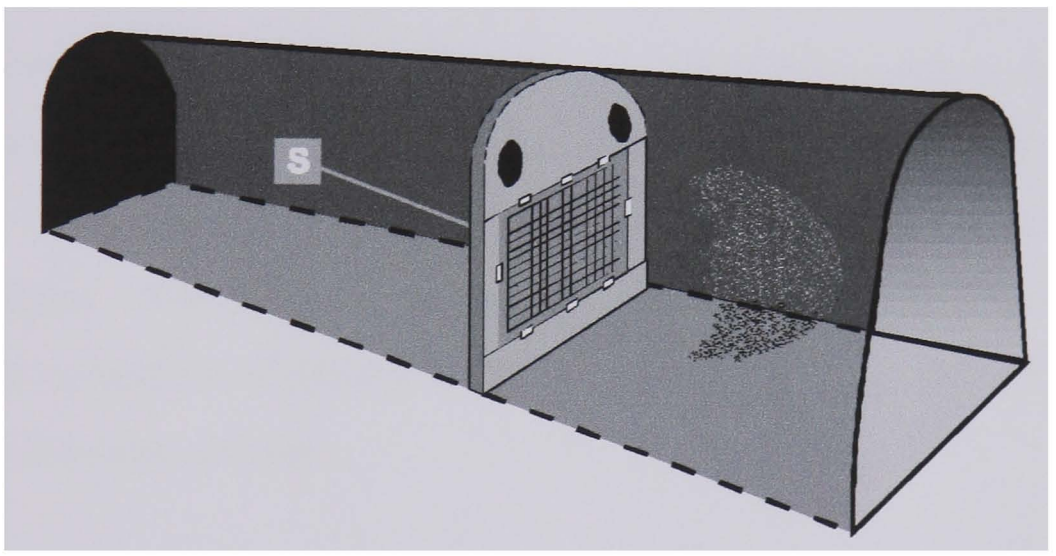

Figure 3.9 - Flame extinguished.

With the passage of the pressure wave, the permeable barrier would be of such a size that the following flame front would not pass through thus causing the flame to be extinguished (Figure 3.9).

3.4 Using barriers to quench explosions

Though the idea of using a porous barrier to quench explosions in an underground mining environment is new, using barriers to quench explosions has been the subject of

some research. In their work, Frolov et al[71] developed a simple analytical theory to predict the rate of decay of a planar shock wave travelling through a gaseous medium blocked by barriers and screens. They derived a parameter, which characterises the dynamic influence of a barrier on a flow. This proposed technique allowed the approximate calculations of shock waves in porous media, though their results are for a block of polyurethane foam.

Defining a device whereby the arresting material takes the form of an obstruction to the flow of gas and flame as a 'flame trap', Phillips and Pritchard[72] reviewed the performance requirements of several flame arresters for stopping a propagating flame in a flammable gas-air mixture. Various types of flame arresting elements or matrix, flame traps, are given: - Gauzes; Perforated plates; Expanded metal; Sintered metal; Metal foam; Compressed wire wool; Loose filling; Hydraulic arresters; Stacked plate; Crimped ribbon.

Many types of arresting elements have been developed for explosion speeds of up to detonation speed. The thermal properties of the elements are important as an element may become hot enough to ignite gases on the other side of the flame trap after quenching a flame. The maximum flame speed it can successfully arrest as well as its ability to stop re-ignition of unburned gases downstream of the arrester determine the effectiveness of a flame arrester.

3.5 Conclusion

Due to the mechanisation of coal production, the risks of methane and coal dust explosions have increased. This chapter has reviewed the current methods used in the arresting of these explosions. In the early days passive barriers using chemical inerting materials in conjunction with either stone-dust or water as the extinguishing material were utilised. However, their method of operation meant that they could be slow in arresting an explosion or could miss the pressure wave and its flame front altogether. Further research resulted in the introduction of active barriers, which used various inert materials to arrest explosions. Due to the fact that they sensed the oncoming blast wave

and then triggered the inert material they have been widely used in mining environments as the main primary barriers for arresting explosions. Though active barriers are more predictable in their performance in comparison with passive barriers, they do fail.

To increases the chances of being able to arrest an explosion should the primary barriers fail in their operation, a secondary explosion-proof barrier has been proposed. This barrier is positioned further away from the source of explosion; i.e. it is located over a kilometre from the coalface. The components of this barrier have been described and in the next chapter, the porous media used in the barrier will be introduced.

The performance of the explosion door and in particular the porous media in the door that will attenuate the shock wave and subsequently arrest the flame will contribute to the body of knowledge on the ability of porous media to attenuate shock waves without sustaining any damage.

CHAPTER 4 Introduction to computational fluid dynamics (CFD)

4.1 Introduction

The performance of the ceramic foam, briefly introduced in the previous chapter (see section 3.3.1.3) and the behaviour of the orifice plates were modelled using the computational fluid dynamics (CFD) code – Rampant[iv]. This not only gives the scope of carrying out more complex analysis, it also allows for the collection of more data that could not be carried out experimentally. From some initial work[73], the flow can be described as unsteady isentropic motion of a compressible fluid in one spatial dimension. Describing the flow as isentropic was based on the assumption that the transition of an initial pressure pulse to a shock wave does not occur. However, in the research reported here, the flow contains a shock wave and all modelling takes this into account. This chapter gives a brief introduction to CFD, introducing the concept of turbulent flow and porous media modelling.

CFD is the analysis of systems involving fluid flow, heat transfer and associated phenomena such as chemical reactions by means of a computer based simulation. Thus it is the art of replacing the governing partial differential equations of fluid flow and advancing these numbers in space and/or time to obtain a final numerical description of the complete flow field of interest[74]. In short the aim of CFD is to predict fluid motion using a computational grid to apply the mass, momentum, and energy balances across each grid cell by means of iterative numerical techniques.

CFD codes are structured around the numerical algorithms that can solve fluid flow problems. There are four distinct streams of numerical solution techniques: finite difference, finite element, finite volume, and spectral methods. These methods solve the governing equations by performing the following steps:-

---

[iv] Rampant is supplied by Fluent Europe Ltd., Holmwood House, Cortworth Road, Sheffield. UK

- approximating the unknown flow variables by means of simple functions,
- discretising by substituting the approximations into the governing equations, and
- solving the algebraic equations.

The main differences between the numerical solution techniques are in the way in which the flow variables are approximated and with the discretisation processes.

4.1.1 Finite difference method

With this method the unknowns Φ (fluid property, e.g. density, pressure, temperature) of the flow problem are described by means of point samples at the node points of a grid of co-ordinate lines. Truncated Taylor series expansions are used to generate finite difference approximations of derivatives of Φ in terms of point samples of Φ at each grid point and its immediate neighbours.

4.1.2 Finite element method

This method uses linear or quadratic piecewise functions valid on elements to describe the local variations of unknown flow variables Φ. The governing equation is precisely satisfied by the exact solution Φ. If the piecewise approximating functions for Φ are substituted into the equation it will not hold exactly and a residual is defined to measure the errors. These residuals (errors) are then minimised by multiplying them by a set of weighting functions and integrating. Thus a set of algebraic equations for the unknown coefficients of the approximating functions are obtained.

4.1.3 Spectral methods

The unknowns are approximated by means of Fourier series or a series of Chebyshev polynomials. Unlike the finite difference approach the approximations are not local but valid over the entire computational domain. The constraint that leads to the algebraic

equations for the coefficients of the Fourier or Chebyshev series is provided by a weighted residuals concept similar to the finite element method or by making the approximate function coincide with the exact solution at a number of grid points.

4.1.4 Finite volume method

This method differs from the other three in that the numerical methods that form the basis for solving the governing equations are solved by firstly integrating the governing equations over all the finite control volumes of the solution domain. What results express the exact conservation of relevant properties for each finite size cell.

This technique is used by Rampant.

4.2 Governing equations for fluid flow

4.2.1 Conservation laws

The governing equations of fluid flow and heat transfer state that:-

- the mass of a fluid is conserved,
- the rate of change of momentum equals the sum of the forces on a particle,
- the rate of change of energy equals the rate of heat addition to and the rate of work done on a fluid particle.

The equations for continuity, momentum and energy are given below:-

4.2.1.1 Continuity equation

$$\frac{\partial(\rho u)}{\partial x}+\frac{\partial(\rho v)}{\partial y}+\frac{\partial(\rho w)}{\partial z}+\frac{\partial \rho}{\partial t}=0 \qquad (4.1)$$

This equation holds for unsteady and compressible flow.

4.2.1.2 Momentum equation

$$\rho\frac{Du}{Dt} = -\frac{\partial p}{\partial x} + \frac{\partial \tau_{xx}}{\partial x} + \frac{\partial \tau_{yx}}{\partial y} + \frac{\partial \tau_{zx}}{\partial z} + S_{Mx} \qquad (4.2)$$

This is the x-component of the momentum equation. Similar equations can be obtained for the y and z components.

In the above equation, τ_{ij} is the viscous stress which acts in the j-direction on a surface normal to the i-direction. p is the pressure, S_{Mx} is the source term which includes contributions to the pressure and viscous forces (surface forces).

4.2.1.3 Energy equation

$$\begin{aligned}\rho\frac{DE}{Dt} = \rho\dot{q} &+ \frac{\partial}{\partial x}\left(k\frac{\partial T}{\partial x}\right) + \frac{\partial}{\partial y}\left(k\frac{\partial T}{\partial y}\right) + \frac{\partial}{\partial z}\left(k\frac{\partial T}{\partial z}\right) \\ &- \frac{\partial(up)}{\partial x} - \frac{\partial(vp)}{\partial y} - \frac{\partial(wp)}{\partial z} \\ &+ \frac{\partial(u\tau_{xx})}{\partial x} + \frac{\partial(u\tau_{yx})}{\partial y} + \frac{\partial(u\tau_{zx})}{\partial z} \\ &+ \frac{\partial(v\tau_{xy})}{\partial x} + \frac{\partial(v\tau_{yy})}{\partial y} + \frac{\partial(v\tau_{zy})}{\partial z} \\ &+ \frac{\partial(w\tau_{xz})}{\partial x} + \frac{\partial(w\tau_{yz})}{\partial y} + \frac{\partial(w\tau_{zz})}{\partial z} + S\end{aligned} \qquad (4.3)$$

Where $\dot{q}$ is the rate of volumetric heat addition per unit mass.

4.2.2 Software modelling – Rampant[75]

Rampant provides a suite of mathematical models for modelling compressible, incompressible, laminar, and turbulent fluid flow problems. Rampant models fluid flow

by solving a set of conservation equations for mass, momentum, and energy. For turbulent flows, there are additional conservation equations for turbulence variables. Turbulent flow is introduced in section 4.3.

4.3 Turbulent flow – introduction

The Reynolds number of a flow gives a measure of the relative importance of inertia forces (associated with convective effects) and viscous forces. At low Reynolds numbers, flows are laminar, however at higher Reynolds numbers, a chaotic and random motion develops in which the velocity and pressure change continuously with time. This behaviour is known as *turbulent* flow. The random nature of a turbulent flow thus precludes computations based on a complete description of all the fluid particles. Instead the velocity can be decomposed into a steady mean value $\bar{u}$, with a fluctuating component $u'(t)$. The velocity fluctuations give rise to additional stresses on the fluid, these are known as Reynolds stresses.

Turbulent flows always have a three-dimensional spatial character and are also characterised by rotational flow structures, turbulent eddies with a wide range of length scales, effective mixing (diffusion), and large Reynolds numbers.

4.3.1 Simulation of turbulent flows

The continuity and Navier-Stokes equations provide a valid description for nearly all flows including turbulent ones. However, to practically simulate the behaviour of a particular turbulent flow, there is a need to solve equations for instantaneous variables but the averaged values are used due to the difficulty in obtaining the instantaneous values.

Reynolds[76] proposed decomposition of the instantaneous variables (e.g. pressure, velocity, density) into mean and fluctuating components. Thus:-

$$u_i = \bar{u}_i + u_i', \; v_i = \bar{v}_i + v_i', \; w_i = \bar{w}_i + w_i',$$

Likewise, for pressure and other scalars :-

$$\phi = \bar{\phi} + \phi',$$

where ϕ denotes general scalars (pressure, enthalpy, and temperature).

By introducing these variables into the instantaneous Navier-Stokes equations and averaging their results gives:- (Note that the overbar on the mean velocity, $\bar{u}$ has been omitted)

Continuity equation:-

$$\frac{\partial \rho}{\partial t} + \frac{\partial}{\partial x_i}(\rho u_i) = 0 \qquad (4.4)$$

Momentum equation:-

$$\frac{\partial}{\partial t}\rho u_i + \frac{\partial}{\partial x_j}(\rho u_i u_j) = \frac{\partial}{\partial x_j}\left[\mu\left(\frac{\partial u_i}{\partial x_j} + \frac{\partial u_j}{\partial x_i}\right) - \frac{2}{3}\mu\frac{\partial u_l}{\partial x_l}\right] + \frac{\partial}{\partial x_j}(-\rho\overline{u_i' u_j'}) - \frac{\partial p}{\partial x_i} \quad (4.5)$$

these equations are written in Cartesian tensor notation.

Equations (4.4) and (4.5) are generally referred to as the Reynolds equations.

Due to the non-linearity of the convection terms in the Navier-Stokes equations, the averaging process introduces some unknown turbulence correlations ($-\rho\overline{u_i' u_j'}$). These are known as the Reynolds (or turbulent) Stresses.

The introduction of the unknown Reynolds stresses by the averaging process renders the equations insoluble, there are more unknowns than there are equations.

4.3.2 Closure models for turbulence

In order to solve the closure problem arising from above, a turbulence model is introduced. This consists of a set of differential equations and/or algebraic formulae that

allow for the determination of the Reynolds stresses and the time-averaged equations of fluid motion. The role of a turbulence model is to provide the numerical value of solutions $-\rho\overline{u_i'u_j'}$ at each point in the flow[77]. This is done by relating $-\rho\overline{u_i'u_j'}$ to the mean velocity and some other known quantities (eddy-viscosity models), or by constructing differential transport equations for $-\rho\overline{u_i'u_j'}$ and solving those in the same way as the Navier-Stokes equations, (Reynolds-Stress transport model [RSM] or second order closure model). Turbulence models are shown in Table 4.1.

Table 4.1 - Turbulence models[78].

Classical models	Based on (time averaged) Reynolds equations
	zero equation model - mixing length model
	two-equation model - k-ε model
	Reynolds stress equation model
	algebraic stress model

The classical models use the Reynolds equations whereas large eddy simulations are models where the time-dependent flow equations are solved for the mean flow and the largest eddies and where the effects of smaller eddies are modelled.

4.3.2.1 Eddy-viscosity models

Here Reynolds stresses may be modelled as being proportional to the mean rate of strain; the proportionality coefficient defining the turbulent (or eddy) viscosity.

Mathematically this is expressed as:-

$$-\overline{u_i u_j} = \upsilon_t\left(\frac{\partial U_i}{\partial x_j}+\frac{\partial U_j}{\partial x_i}\right)-\frac{2}{3}\delta_{ij}k \qquad (4.6)$$

The eddy viscosity, υ_t, which is a function of the flow can be evaluated from turbulence models consisting of zero, one, and two-equation models.

4.3.2.2 Reynolds-stress-transport models

In Reynolds-stress-transport models, the Reynolds stresses are obtained directly from the solution of the differential transport equations in which they are dependent variables. Although more complicated than Eddy-viscosity models, their use is increasing due to the fact that they provide more accurate representation of turbulence and are also valid over a wider range of flows.

The advantages and disadvantages of the turbulence closure models are given in Table 4.2.

4.4 Turbulent models in Rampant

Rampant models turbulence using the two-equation turbulence models. In two-equation models, the effects of turbulence are represented by an isotropic eddy or turbulent viscosity which is evaluated using two quantities: turbulent kinetic energy (k) and its dissipation (ε).

If a general scalar quantity ϕ is used then the general conservation equation can be written as:-

$$\frac{\partial}{\partial t}\left(\overline{\rho}\overline{\phi}\right)+\frac{\partial}{\partial x_i}\left(\overline{\rho}\overline{u}_i\overline{\phi}\right)=-\frac{\partial}{\partial x_i}\left(\overline{\rho u_i'\phi'}\right)+\overline{D}_\phi+\overline{S}_\phi \qquad (4.7)$$

The correlation, $\overline{\rho u_i'\phi'}$ appears as $\overline{\rho u_i' m_i'}$ and $\overline{\rho u_i' h'}$ in the species conservation and enthalpy equations respectively.

The task of the turbulence models are to provide expressions or closure models that allow evaluation of these correlations in terms of mean flow quantities. The turbulence closure models used in Rampant are:-

- the k-ε model

- the ReNormalization Group (RNG) k-ε model

Table 4.2 - Turbulence models - advantages and disadvantages.[78]

Model	Advantages	Disadvantages
Mixing length model	easy to implement in terms of computing resources good predictions for thin shear layers well established	incapable of describing flows with separation and recirculation only calculates mean flow properties and turbulent shear stress
k-ε model	simplest turbulence model - only initial and/or boundary conditions need to be supplied excellent performance for many industrially relevant flows well established	more expensive to implement than mixing length model poor performance in cases such as:- unconfined flows flows with large extra strains rotating flows fully developed flows in non-circular ducts
Reynolds stress equation model (RSM)	potentially the most general of all classical turbulence models only initial and/or boundary conditions need to be supplied accurate calculation of mean flow properties and all Reynolds stresses	large computing costs not as widely validated as the two previous models performs as badly as the k-ε model in some flows due to problems with the ε-equation modelling
Algebraic stress model (ASM)	cheap method to account for Reynolds stress anisotropy potentially combines the generality of approach of the RSM. if convection and diffusion terms are negligible the ASM performs as well as the RSM	only slightly more expensive than the k-ε model not as widely validated as the two previous models same disadvantages as the RSM apply model is severely restricted in flows where the transport assumptions for convective and diffusive effects do not apply.

4.4.1 The k-ε model

The k-ε is a semi-empirical model. It is the most widely used turbulence model in practical engineering calculations. In the k-ε turbulence model (an eddy-viscosity model), the Reynolds stresses are assumed to be proportional to the mean velocity gradients, with the constant of proportionality being the turbulent viscosity, μ_t. The turbulent viscosity is obtained by assuming that it is proportional to the product of a turbulent velocity scale and length scale. The Reynolds stresses are provided by:-

$$\rho\overline{u_i' u_j'} = \rho\frac{2}{3}k\delta_{ij} - \mu_t\left(\frac{\partial u_i}{\partial x_j} + \frac{\partial u_j}{\partial x_i}\right) + \frac{2}{3}\mu_t\frac{\partial u_l}{\partial x_l}\delta_{ij} \qquad (4.8)$$

$$\text{where } k = \frac{1}{2}\sum_i \overline{u_i'^2} \qquad (4.13)$$

The velocity and length scales are obtained from two parameters:-

k - turbulent kinetic energy,

ε - dissipation rate of the kinetic energy.

The velocity scale is taken to be $\sqrt{k}$ and the length scale is taken to be $\frac{\sqrt{k^3}}{\varepsilon}$.

$$\text{Thus } \mu_t = \frac{\rho C_\mu k^2}{\varepsilon} \qquad (4.9)$$

where C_μ is an empirically derived constant of proportionality (set to a default value of 0.09 in Rampant).

Transport equations for k and ε are obtained from the following equations:-

$$\frac{\partial}{\partial t}(\rho k) + \frac{\partial}{\partial x_i}(\rho u_i k) = \frac{\partial}{\partial x_i}\left(\frac{\mu_t}{\sigma_k}\frac{\partial k}{\partial x_i}\right) + G_k + G_b - \rho\varepsilon \qquad (4.10)$$

and

$$\frac{\partial}{\partial t}(\rho\varepsilon)+\frac{\partial}{\partial x_i}(\rho u_i\varepsilon)=\frac{\partial}{\partial x_i}\left(\frac{\mu_t}{\sigma_\varepsilon}\frac{\partial\varepsilon}{\partial x_i}\right)+C_{1\varepsilon}\frac{\varepsilon}{k}\left(G_k+(1-C_{3\varepsilon})G_b\right)-C_{2\varepsilon}\rho\frac{\varepsilon^2}{k} \qquad (4.11)$$

Here $C_{1\varepsilon}$, $C_{2\varepsilon}$, and $C_{3\varepsilon}$ are empirical constants,

σ_k and σ_ε are the inverse effective Prandtl numbers for k and ε, respectively.

G_k is the rate of production of turbulent kinetic energy:-

$$G_k=\mu_t\left(\frac{\partial u_j}{\partial x_i}+\frac{\partial u_i}{\partial x_j}\right)\frac{\partial u_i}{\partial x_i} \qquad (4.12)$$

and G_b is the generation of turbulence due to buoyancy:-

$$G_b=-g_i\frac{\mu_t}{\rho\sigma_h}\frac{\partial\rho}{\partial x_i} \qquad (4.13)$$

One limitation of the k-ε model is that μ_t is isotropic. This implies that the velocity and length scales are the same in all directions.

4.4.2 The RNG k-ε model

The *RNG*-based k-ε turbulence model is based on a mathematical foundation to turbulence transport modelling as opposed to the common semi-empirical approaches. It provides a more general and fundamental model and yields improved predictions of near-wall flows, flows with high streamline curvature and high strain rate, low-Reynolds-number and transitional flow, wall heat/mass transfer, and detailed wake flow and vortex shedding behaviour.

The RNG k-ε model differs from the standard k-ε model in that:-

- its constants and functions are modelled by theory and not by empiricism, making it applicable without modification,

- low-Reynolds-number effects are included permitting laminar-like behaviour to be predicted,
- new terms appear in the dissipation rate transport equation including a rate-of-strain term which is important for treatment of non-equilibrium effects and flows in the rapid distortion limit (separated flows and stagnation flows),
- compressibility effects on turbulence are included,
- turbulent transport equations are extended to permit prediction of swirling flows.

Transport equations for *RNG* k and ε are obtained from the following equations:-

$$\frac{\partial k}{\partial t} + u_i \frac{\partial k}{\partial x_i} = \upsilon_t S^2 - \varepsilon + \frac{\partial}{\partial x_i} \alpha \upsilon_t \frac{\partial k}{\partial x_i} \quad (4.14)$$

and

$$\frac{\partial \varepsilon}{\partial t} + u_i \frac{\partial \varepsilon}{\partial x_i} = C_{1\varepsilon} \frac{\varepsilon}{k} \upsilon_t S^2 - C_{2\varepsilon} \frac{\varepsilon^2}{k} - R + \frac{\partial}{\partial x_i} \alpha \upsilon_t \frac{\partial \varepsilon}{\partial x_i} \quad (4.15)$$

where α is the inverse Prandtl number for turbulent transport, S is the modulus of the mean rate-of-strain tensor, S_{ij}, and R is the rate-of-strain term.

4.4.2.1 RNG modification for compressibility

In the *RNG* k-ε model in Rampant, the effects of compressibility are accounted for by modifying the dissipation in the k equation as:-

$$\frac{\partial}{\partial t}(\rho k) + \frac{\partial}{\partial x_i}(\rho u_i k) = \frac{\partial}{\partial x_i}\left(\frac{\mu_t}{\sigma_k}\frac{\partial k}{\partial x_i}\right) + \tau_{ij} S_{ij} - \rho \frac{C_\mu k^2}{\upsilon_c} \quad (4.16)$$

$$\text{where } \upsilon_c = \upsilon_{mol} + \frac{\upsilon_t}{1 + 2M_t^2} \quad (4.17)$$

M_t is a turbulent Mach number defined by:-

$$M_t = \sqrt{\frac{k}{a^2}} \qquad (4.18)$$

where a ($\equiv\sqrt{\gamma RT}$) is the speed of sound.

4.4.3 Discretisation scheme in Rampant

The Rampant solver is a time-marching scheme with integration in time being handled with a multi-stage Runge-Kutta scheme with multigrid convergence acceleration.

In Rampant, the time-dependent equations must be discretised in both space and time. The spatial discretisation for the time-dependent equations is identical to the steady-state case. Temporal discretisation involves the integration of every term in the differential equations over a time step Δt. The integration of the transient terms is shown below:-

$$\frac{\partial \phi}{\partial t} = F(\phi) \qquad (4.19)$$

where the function F incorporates any spatial discretisation. Equation (4.19) is a generic expression for the time evolution of a scalar quantity ϕ.

If the time derivative is discretised using backward differences, the first-order accurate temporal discretisation is given by:-

$$\frac{\phi^{n+1} - \phi^n}{\Delta t} = F(\phi) \qquad (4.20)$$

and the second order discretisation is given by:-

$$\frac{3\phi^{n+1} - 4\phi^n + \phi^{n-1}}{2\Delta t} = F(\phi) \qquad (4.21)$$

where

ϕ is a scalar quantity

$n+1$ is the value at the next time level, $t+\Delta t$

n is the value at current time level, t

n-1 is the value at previous time level, t-Δt.

Once the time derivative has been discretised, F can be evaluated in two ways, as shown in sections 4.4.3.1 and 4.4.3.2.

4.4.3.1 Explicit time integration

One method is to evaluate $F(\phi)$ at the current time level

$$\frac{\phi^{n+1} - \phi^n}{\Delta t} = F\left(\phi^n\right) \qquad (4.22)$$

This is referred to as "explicit" integration since ϕ^{n+1} can be expressed explicitly in terms of the existing solution value, ϕ^n:

$$\phi^{n+1} = \phi^n + \Delta t F\left(\phi^n\right) \qquad (4.23)$$

This is the method used by Rampant when global time stepping is selected. Here, the time step, Δt, is restricted to the stability limit of the underlying solver (i.e., a time step corresponding to Courant number of approximately 1). The Courant number is the ratio of the time step Δt to the characteristic convection time, $u/\Delta x$, the time required for a disturbance to be convected a distance Δx. With Rampant's explicit time integration, all the cells in the domain must use the same time step, thus for stability, the time step used is the minimum of all the local time steps in the domain.

Global time stepping is used to capture the transient behaviour of moving waves such as shocks. This was the scheme chosen for solving the shock tube problem when the permeable barrier was in place.

4.4.3.2 Implicit time integration

Another method is to evaluate $F(\phi)$ at the future time level:-

$$\frac{\phi^{n+1}-\phi^{n}}{\Delta t}=F\left(\phi^{n+1}\right) \quad (4.24)$$

This is referred to as "implicit" integration since ϕ^{n+1} in a given cell is related to ϕ^{n+1} in neighbouring cells through $F(\phi^{n+1})$:-

$$\phi^{n+1}=\phi^{n}+\Delta tF\left(\phi^{n+1}\right) \quad (4.25)$$

This implicit equation can be solved iteratively by initialising ϕ^{i} to ϕ^{n} and iterating the equation:-

$$\phi^{i}=\phi^{n}+\Delta tF\left(\phi^{i}\right) \quad (4.26)$$

(first order)

or

$$\phi^{i}=\frac{4}{3}\phi^{n}-\frac{1}{3}\phi^{n-1}+\frac{2}{3}\Delta tF\left(\phi^{i}\right) \quad (4.27)$$

(second order)

This is the method used by Rampant when first- or second-order dual time stepping option is selected. The advantage of the fully implicit scheme is that it is unconditionally stable with respect to time step size.

4.4.4 Porous media modelling in Rampant

The porous media in Rampant can be used for flows through permeable barriers. In Rampant, when the porous media model is used, special cells are defined in which the porous media is applied and the pressure loss in the flow is determined via the equations given below.

The porous media model incorporates an empirically determined flow resistance in the region defined as porous. Thus a momentum sink is added to the governing momentum

equations. Equation (4.28) written in Cartesian tensor notation shows an equation for the case of a simple homogeneous porous media.

$$S_i = \frac{\mu}{\alpha} v_i + C_2 \frac{1}{2} \rho |v_i| v_i \qquad (4.28)$$

where

S_i is the source term for the ith (x, y, or z) momentum equation,

μ is the dynamic viscosity,

v_i is the velocity component,

α is the permeability term, and

C_2 is the inertial resistance factor.

The momentum sink term in the above equation contribute to the pressure gradient in the porous cell, creating a pressure drop that is in proportion to the fluid velocity (or velocity squared) in the cell.

At high flow velocities, the constant C_2 in the equation above provides a correction for the inertial losses in the porous medium. This constant can be thought of as a loss coefficient per unit length along the flow direction, thereby allowing pressure drop to be specified as a function of dynamic head.

Due to the fact that the porous media model is nothing more than an added momentum sink in the governing equations, there are limitations in using this model:-

- The fluid does not accelerate as it moves through the medium, since the volume of the blockage that is physically present is not represented in the model. This may have a significant impact in transient flows since it implies that the transit time for the flow through the medium is not correctly represented by Rampant.

- The solid portion of the medium is not represented, hence Rampant cannot predict the effect of the solid medium on temperature. Though the effects of temperature on the solid portion of the porous media was not interest in this research.

- The effect of the porous medium on the turbulence field is only approximated.

The limitations of the porous media model in Rampant meant that it could not accurately represent the flow through the ceramic foam and it was not used. A different approach to modelling the flow through the ceramic foam was devised (see section 5.4.1) and used in subsequent simulations.

4.5 Conclusion

This chapter introduced the concept of computational fluid dynamics (CFD) and turbulence modelling. It was shown that there are numerical solution techniques algorithms for solving the governing equations of fluid flow. These techniques approximate the unknown variables in the governing equations by mathematical equations that are dependent on the numerical solution technique. As an example, the Finite difference method (section 4.1.1) uses truncated Taylor series expansions to generate finite difference approximations for the variables in the governing equations.

Turbulent flow and how it is modelled was also introduced. The introduction of the extra terms in the governing equations due to turbulence, it was shown, leads to the introduction of closure models. These models provide solutions for these stress terms. The advantages and disadvantages of some of these turbulence models were shown, with a brief description on the more common turbulence currently used.

In rounding off the discussion on CFD, temporal discretisation schemes used by Rampant were introduced. They showed how the governing equations are differentiated over a given time step.

The porous media model in the CFD code, Rampant, was discussed and its limitations highlighted. These limitations meant that it could not accurately model the problem of fluid flow through the porous material to be modelled so it was not used.

CFD has become a tool for solving fluid flow and in the work reported herein, it was used to model the passage of shock wave in a shock tube.

The next chapter introduces the equipment used in the tests conducted; the shock tube and ceramic foam and how the porous media was represented numerically. Also validation results are given.

CHAPTER 5 The Porous Media and Experimental Set-up

5.1 Introduction

Chapters two and three discussed the coal dust explosions in underground mining tunnels and the current methods used for arresting these explosions respectively, whilst the previous chapter highlighted the inability of Rampant to simulate the flow within the porous media, and thus determine its performance. Though these current explosion arresting systems are in use in mines throughout the world, the risk of an underground mining explosion is ever present and these systems fail from time to time. To further reduce this risk, the possibility of arresting an explosion using an active explosion door that incorporates a porous region is the subject of this thesis. The porous section of the explosion door allows the passage of the shock wave that normally precedes the flame front whilst arresting the flames.

The porous media used within the explosion door is commonly known as ceramic foam and is widely used within the castings industry as a filter in the metal making process.

The ceramic foam, the experimental set-up, analytical results of a shock tube flow and some initial validation of experimental tests are presented in this chapter.

As a useful comparison, tests were conducted on thin orifice plates. The results that would be obtained from such a test would help draw up a correlation table between the performance characteristics of the ceramic foams and the orifice plates. Also various hole configurations of the orifice plates would be tested to determine whether the configuration of the orifice plate has an impact on the pressure attenuation characteristics of an orifice plate. A brief discussion on the orifice plates used is given in section 5.5.

5.2 Shock tubes

In order to fully describe the shock tube, it is worth giving a brief account of its *raison d'être*. The shock tube is used to generate shock waves and the shock wave is described

as a very sharp, thin, wave front which has a thickness of about a millionth of an inch, Glass[79]. A shock wave is generated when energy is suddenly released or deposited in a material such as, a liquid, solid, or a gas, thereby causing an explosion.

As an example, the processes involved in a spherical explosion are as follows: the shock wave races into the medium like a tidal wave and abruptly raises the material to a very high pressure, density, and temperature. It also induces a flow velocity that races behind it. As the spherical shock wave engulfs ever greater volumes of the material, it finally decays to a weak disturbance or sound wave.

5.2.1 Shock wave generation

Shock waves were briefly introduced in chapter two. Here a more detailed discussion on the generation of shock waves and shock wave theory is given.

The simplest means of observing the generation of a shock wave is through the motion of a piston in a cylinder. By moving the piston in a cylinder, a disturbance in the form of a planar sound pulse is generated. This races ahead of the piston at the speed of sound, heating and compressing the gas. At some time further on, the piston has moved to another point and another sound pulse is further produced. However, as this pulse is moving into a preheated gas, it will move faster (sound speed increases with temperature) and will overtake and unite with the first pulse to form a weak shock wave. This process continues until a step change in pressure occurs resulting in a shock wave. There is also a step change in all the physical quantities such as temperature, density, and velocity. In the latter case, the velocity is zero in front of the shock wave and behind it has a value that is identical to the speed of the piston. However, behind the piston, the reverse process takes place as the gas is cooled and rarefied. The pulses diverge and give rise to a rarefaction or expansion wave. Figure 5.1 shows the generation of a shock wave in a piston.

However, if the piston is accelerated impulsively from rest to a finite velocity, then a shock wave is instantly generated and all quantities remain constant from the piston face to the shock front. In practice, breaking a thin diaphragm under pressure in a shock

tube; where the driver channel is filled with a gas at a higher pressure, simulates such impulsive motion. Figure 5.2 shows the initial state of the pressure distribution in a shock tube before the diaphragm is broken.

An important application of unsteady wave motion is a shock tube.

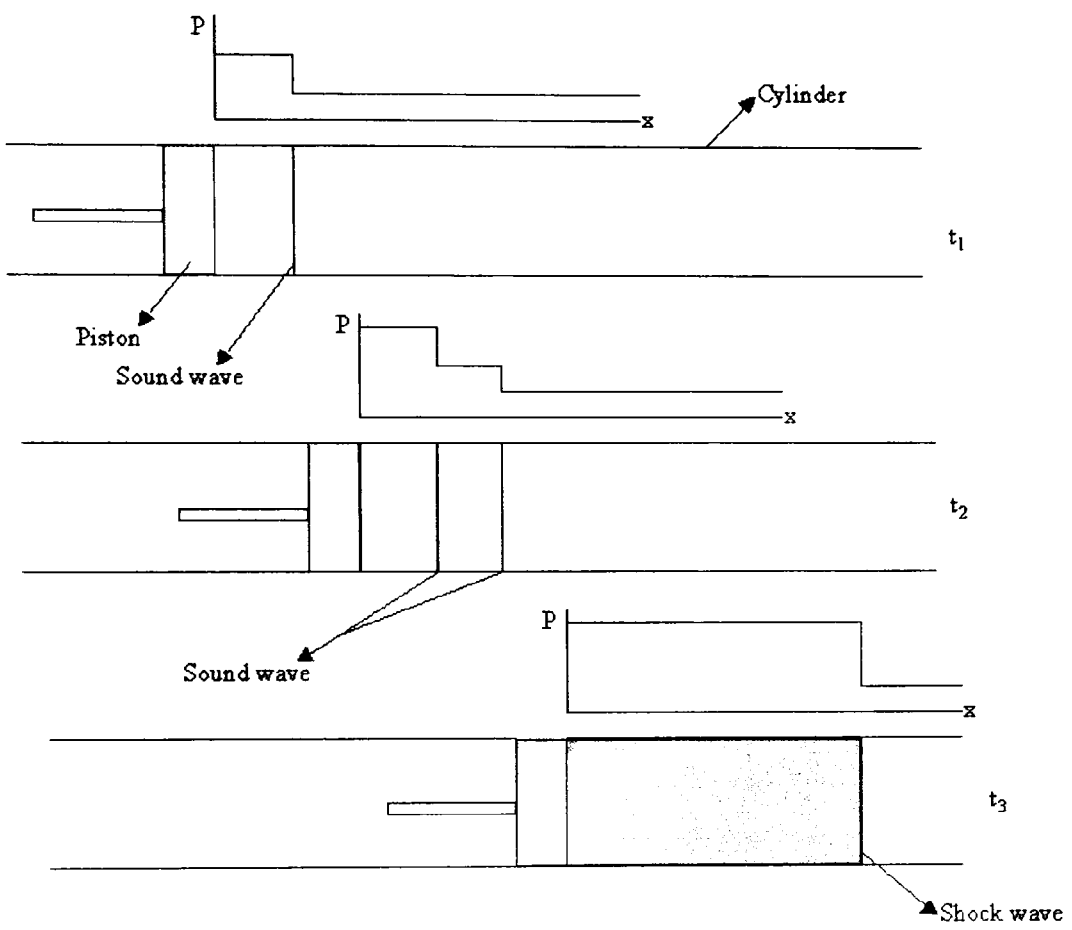

Figure 5.1 – Generating a shock wave with a piston.

Shock tubes are usually closed at both ends with a diaphragm separating a region of high pressure (4) from a region of low pressure (1). The diaphragm pressure ratio is p_4/p_1. The diaphragm pressure ratio is defined as the ratio of the pressure across the diaphragm separating the high pressure (driver section) from the low pressure region (driven section).

The gases in regions (1) and (4) can be at different temperatures and have different molecular weights. In this research, air is the gaseous media in both regions.

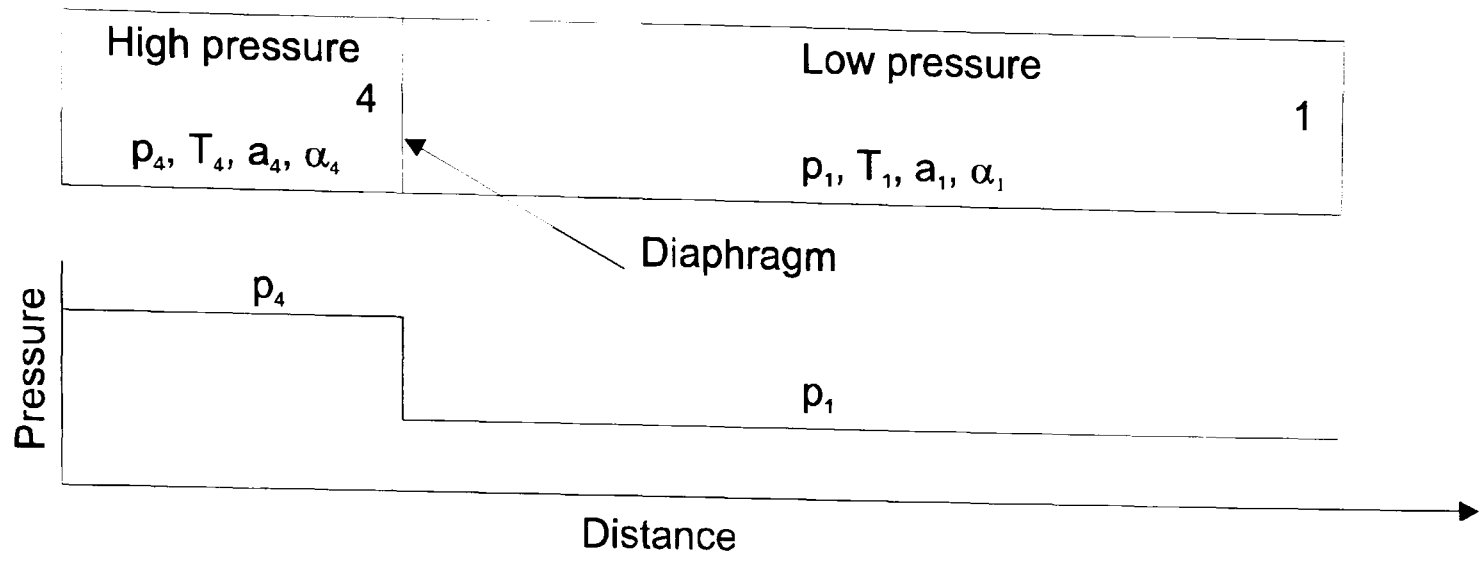

Figure 5.2 – Initial conditions in a shock tube.

When the diaphragm is broken by mechanical or electrical means, a shock wave propagates into region (1) and an expansion wave propagates into region (4). Figure 5.3 shows the flow field in a shock tube after the diaphragm is broken.

In shock tubes, the flow field in the tube after the diaphragm is broken is determined by the given conditions in regions (1) and (4) before the diaphragm is broken. The following steps describe what happens immediately after the diaphragm is broken:-

- the shock wave propagates to the right with a velocity W,
- the moving shock increases the pressure of the gas behind it (region (2)),
- the moving shock induces a mass motion with a velocity u_p,
- the moving shock is followed by a contact surface, this is the interface between the driver and driven gases. The contact surface also moves with velocity u_p,
- an expansion (rarefaction) wave propagates to the left (region (4)).

The new boundary of the driver gas is now the contact surface. At the contact surface, the flow pressure and velocity are matched on either side but all other thermodynamic properties are changed. The expansion and cooling through the rarefaction is a constant entropy (isentropic and reversible) process, whereas the compression and heating process through the shock transition is irreversible and the entropy increases. On either side of the shock front, the entropy is constant.

Figure 5.4 shows the shadowgram of a bursting cellophane diaphragm in a rectangular shock tube with a diaphragm pressure ratio of 2. The bulging, ruptured diaphragm D, and the pressurised air A, escaping through the fragments F, appear on the left. The curved incident S_i, and reflecting S_r, compression and shock waves are seen on the right.

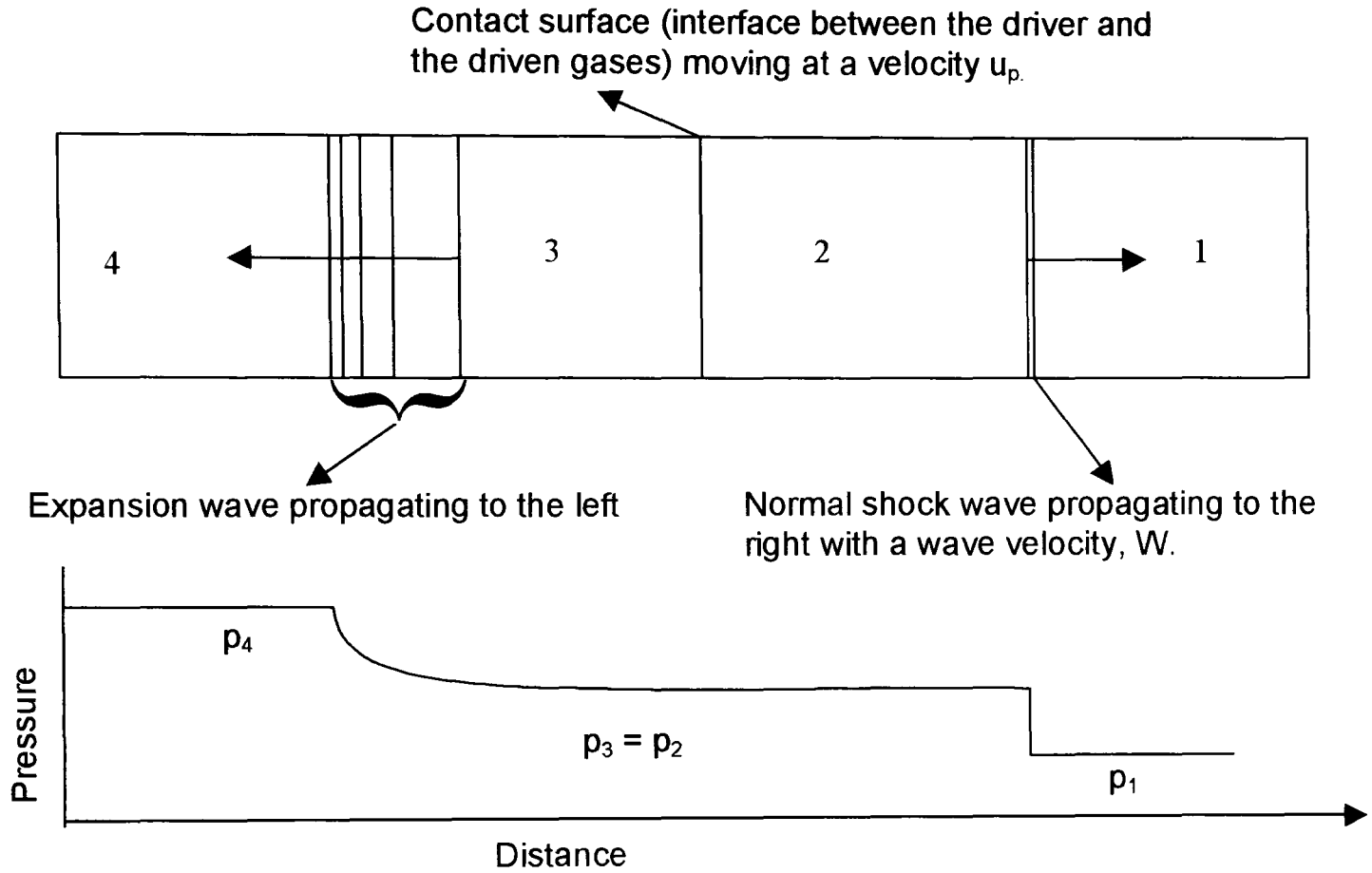

Figure 5.3 – Flow in a shock tube after the diaphragm has been broken.

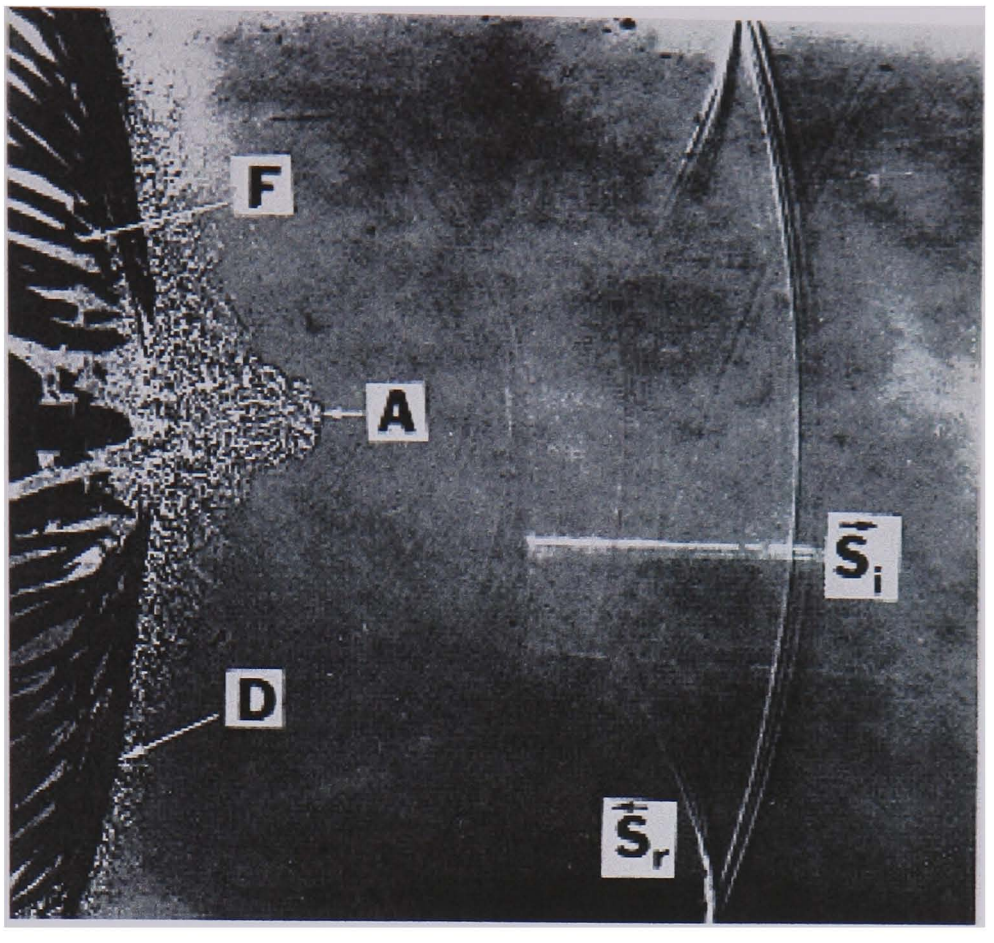

Figure 5.4 – Formation of a shock wave in a shock tube [79].

5.2.2 Shock wave theory – analytical

As mentioned earlier, if a piston is accelerated impulsively from rest to a finite velocity then a shock wave is generated. Breaking a thin diaphragm under pressure in a shock tube generates such a motion. Figure 5.3 describes such a motion and forms the basis of the ensuing discussion.

A shock wave is generated which travels to the right (low pressure region) of the shock tube with a velocity W (region (1) ahead of the shock wave and relative to the wave. In region (2), the velocity of the gas behind the shock wave is W - u_p relative to the wave. For regions (1) and (2) in the shock tube, the fluid flow must obey the equations for continuity, momentum, and energy for normal moving shock as the flow is akin to that of an unsteady moving shock wave, Anderson[80]. These are:-

$$\rho_1 W = \rho_2 \left(W - u_p \right) \qquad (5.1)$$

$$p_1 + \rho_1 W^2 = p_2 + \rho_2 \left(W - u_p \right)^2 \qquad (5.2)$$

$$h_1 + \frac{W^2}{2} = h_2 + \frac{\left(W - u_p\right)^2}{2} \qquad (5.3)$$

Rearranging equation (5.1) gives:-

$$W - u_p = W\frac{\rho_1}{\rho_2} \qquad (5.4)$$

Substituting equation (5.4) into (5.2) gives:-

$$p_1 + \rho_1 W^2 = p_2 + \rho_2 W^2\left(\frac{\rho_1}{\rho_2}\right)^2 \text{ and rearranging}$$

$$p_2 - p_1 = \rho_1 W^2\left(1 - \frac{\rho_1}{\rho_2}\right)$$

$$W^2 = \frac{p_2 - p_1}{\rho_2 - \rho_1}\left(\frac{\rho_2}{\rho_1}\right) \qquad (5.5)$$

From equation (5.1),

$$W = \left(W - u_p\right)\frac{\rho_2}{\rho_1} \qquad (5.6)$$

Substituting equation (5.6) into (5.5) yields

$$\left(W - u_p\right)^2\left(\frac{\rho_2}{\rho_1}\right)^2 = \frac{p_2 - p_1}{\rho_2 - \rho_1}\left(\frac{\rho_2}{\rho_1}\right)$$

or (5.7)

$$\left(W - u_p\right)^2 = \frac{p_2 - p_1}{\rho_2 - \rho_1}\left(\frac{\rho_1}{\rho_2}\right)$$

Recalling that $h = e + p/\rho$ and substituting equations (5.5) and (5.7) into (5.3) gives:-

$$e_1 + \frac{p_1}{\rho_1} + \frac{1}{2}\left[\frac{p_2 - p_1}{\rho_2 - \rho_1}\left(\frac{\rho_2}{\rho_1}\right)\right] = e_2 + \frac{p_2}{\rho_2} + \frac{1}{2}\left[\frac{p_2 - p_1}{\rho_2 - \rho_1}\left(\frac{\rho_1}{\rho_2}\right)\right] \qquad (5.8)$$

Equation (5.8) simplifies to:-

$$e_2 - e_1 = \frac{p_1 + p_2}{2}\left(\frac{1}{\rho_1} - \frac{1}{\rho_2}\right)$$

or

$$e_2 - e_1 = \frac{p_1 + p_2}{2}(v_1 - v_2) \qquad (5.9)$$

where v is volume.

Equation (5.9) is the Hugoniot equation and it relates to the changes in the thermodynamic variables across a normal shock. It is independent of whether or not the shock is moving.

For a perfect gas where $e = c_v T$, and $v = RT/p$, equation (5.9) becomes:-

$$\frac{T_2}{T_1} = \frac{p_2}{p_1}\left(\frac{\frac{\gamma+1}{\gamma-1} + \frac{p_2}{p_1}}{1 + \frac{\gamma+1}{\gamma-1}\frac{p_2}{p_1}}\right) \qquad (5.10)$$

and

$$\frac{\rho_2}{\rho_1} = \frac{1 + \frac{\gamma+1}{\gamma-1}\left(\frac{p_2}{p_1}\right)}{\frac{\gamma+1}{\gamma-1} + \frac{p_2}{p_1}} \qquad (5.11)$$

which are the temperature ratio and density ratio across the shock wave as a function of the pressure ratio, respectively.

As the shock is moving, the parameter p_2/p_1 governs the changes across the shock wave and this is reinforced by defining the moving shock Mach number as:-

$$M_s = \frac{W}{a_1}.$$

where $a=\sqrt{\gamma RT}$.

Incorporating this definition along with the perfect gas relations into equations (5.1) to (5.3) gives:-

$$\frac{p_2}{p_1} = 1 + \frac{2\gamma}{\gamma+1}\left(M_s^2 - 1\right) \qquad (5.12)$$

Solving for M_s,

$$M_s = \sqrt{\frac{\gamma+1}{2\gamma}\left(\frac{p_2}{p_1} - 1\right) + 1} \qquad (5.13)$$

Since $M_s = \frac{W}{a_1}$, equation (5.13) yields

$$W = a_1\sqrt{\frac{\gamma+1}{2\gamma}\left(\frac{p_2}{p_1} - 1\right) + 1} \qquad (5.14)$$

Equation (5.14) relates the wave velocity of the moving shock wave to the pressure ratio across the wave and the speed of sound of the gas into which the wave is propagating.

As the shock wave is propagating into a stagnant gas, it induces a mass motion with velocity u_p behind the wave which from equation (5.1) is:-

$$u_p = W\left(1 - \frac{\rho_1}{\rho_2}\right) \qquad (5.15)$$

Substituting equations (5.10) and (5.14) into (5.15), and simplifying yields:-

$$u_p = u_2 = \frac{a_1}{\gamma}\left(\frac{p_2}{p_1} - 1\right)\left(\frac{\frac{2\gamma}{\gamma+1}}{\frac{p_2}{p_1} + \frac{\gamma-1}{\gamma+1}}\right)^{\frac{1}{2}} \qquad (5.16)$$

which is dependent on the pressure ratio across the shock wave and the speed of sound of the gas ahead of the shock wave.

There is a limiting value for u_p and this is calculated as follows:-

The Mach number of the induced motion is u_p/a_2, where

$$\frac{u_p}{a_2} = \frac{u_p}{a_1}\frac{a_1}{a_2} = \frac{u_p}{a_1}\sqrt{\frac{T_1}{T_2}} \qquad (5.17)$$

Substituting equations (5.10) and (5.16) into (5.17):-

$$\frac{u_p}{a_2} = \frac{1}{\gamma}\left(\frac{p_2}{p_1} - 1\right)\left(\frac{\frac{2\gamma}{\gamma+1}}{\frac{p_2}{p_1} + \frac{\gamma-1}{\gamma+1}}\right)^{\frac{1}{2}}\left[\frac{1 + \frac{\gamma+1}{\gamma-1}\left(\frac{p_2}{p_1}\right)}{\frac{\gamma+1}{\gamma-1}\left(\frac{p_2}{p_1}\right) + \left(\frac{p_2}{p_1}\right)^2}\right]^{\frac{1}{2}} \qquad (5.18)$$

Considering an infinitely strong shock where p_2/p_1 approaches infinity, equation (5.18) becomes:-

$$\lim_{p_2/p_1 \to \infty}\left(\frac{u_p}{a_2}\right) = \sqrt{\frac{2}{\gamma(\gamma-1)}} \qquad (5.19)$$

For $\gamma = 1.4$ (for air), equation (5.19) shows that $u_p/a_2 \to 1.89$ as $p_2/p_1 \to \infty$.

Thus for perfect gas with $\gamma = 1.4$, the Mach number of the induced flow cannot exceed 1.89.

5.2.3 Other shock tube relations

Pressure relation between regions (3) and (4):-

$$\frac{p_3}{p_4} = \left[1 - \frac{\gamma_4 - 1}{2}\left(\frac{u_3}{u_4}\right)\right]^{\frac{2\gamma_4}{\gamma_4 - 1}} \qquad (5.20)$$

Solving for u_3 in equation (5.20) gives:-

$$u_3 = \frac{2a_4}{\gamma_4 - 1}\left[1 - \left(\frac{p_3}{p_4}\right)^{\frac{\gamma_4 - 1}{2\gamma_4}}\right] \qquad (5.21)$$

However, since $p_3 = p_2$, equation (5.21) becomes:-

$$u_3 = \frac{2a_4}{\gamma_4 - 1}\left[1 - \left(\frac{p_2}{p_4}\right)^{\frac{\gamma_4 - 1}{2\gamma_4}}\right] \qquad (5.22)$$

Recalling that $u_2 = u_3$, equations (5.16) and (5.21) can be equated as:-

$$\frac{a_1}{\gamma_1}\left(\frac{p_2}{p_1} - 1\right)\left(\frac{\frac{2\gamma}{\gamma+1}}{\frac{p_2}{p_1} + \frac{\gamma - 1}{\gamma + 1}}\right)^{\frac{1}{2}} = \frac{2a_4}{\gamma_4 - 1}\left[1 - \left(\frac{p_2}{p_4}\right)^{\frac{\gamma_4 - 1}{2\gamma_4}}\right] \qquad (5.23)$$

Equation (5.23) can be rearranged algebraically to give:-

$$\frac{p_4}{p_1} = \frac{p_2}{p_1}\left[1 - \frac{(\gamma_4 - 1)(a_1/a_4)(p_2/p_1 - 1)}{\sqrt{2\gamma_1\{2\gamma_1 + (\gamma_1 + 1)(p_2/p_1 - 1)\}}}\right]^{-\frac{2\gamma_4}{\gamma_4 - 1}} \qquad (5.24)$$

As air is the fluid being used in these experiments ($\gamma_4 = \gamma_1$), equation (5.24) further reduces to:-

$$\frac{p_4}{p_1} = \frac{p_2}{p_1}\left[1 - \frac{0.4(p_2/p_1 - 1)}{\sqrt{2.8\{2.8 + 2.4(p_2/p_1 - 1)\}}}\right]^{-7} \qquad (5.25)$$

Equation (5.25) gives the incident shock strength p_2/p_1 as an implicit function of the diaphragm pressure ratio p_4/p_1. See Figure 5.2.

Equation (5.25) above allows the derivation of a set of analytical results for the shock tube given the diaphragm pressure ratio. This allows the comparison of the incident

pressure magnitude from the computational modelling and from the experiments. A table of the analytical results derived from equation (5.25) is given below.

Table 5.1 – Analytical values of incident pressure given the diaphragm pressure ratio.

Diaphragm Pressure ratio, p_4/p_1	Incident Pressure ratio, p_2/p_1	Shock Wave Mach number, M_s	Induced Flow Velocity, u_p *or* u_2. (m/s)
8.00	2.60	1.54	257.7
8.38 (p_4 = 8.38 bar)	2.65	1.55	263.3
6.99 (p_4 = 6.99 bar)	2.46	1.50	240.8
5.59 (p_4 = 5.59 bar)	2.23	1.43	213.3

This brief introduction to shock waves and its generation shows that as the magnitudes of the flow properties within a shock tube can be determined analytically, these values can be compared with those generated from computational simulations and experimental results. It also shows that a simple shock tube can be used to generate shock waves with varying incident Mach numbers depending on either the gaseous material used as the driver gas or the pressure ratio across the diaphragm.

For a more detailed review of the various driver gas materials used in shock tubes, the reader is referred to the work of Glass and Sislian[81].

5.2.4 Shock wave theory – numerical

The shock tube flow can be described as a Riemann problem[82] for which there are various numerical methods for resolving the flow field after the diaphragm separating two pressure regions is ruptured. The Riemann problem is a particular case of one-dimensional flow where the problem is to find the gas flow resulting from an initial state where the gas in one region is at a pressure and density different from the pressure and density in the other region. Riemann[83] predicted that there are two possible wave systems following the rupturing of the diaphragm. The first is when the rarefaction wave is approaching the shock wave. The other is when the two waves move apart with the

shock wave moving into the low pressure region, and the rarefaction wave moving into the high pressure region. The latter wave system is the correct one as the former contradicts the physical initial condition that the pressure discontinuity is at the origin and not at infinity at the initial moment.

With the dominant nature of the flow in the direction of the shock, and with the absence of molecular diffusion, the nature of the flow field can be determined by the one-dimensional Euler equations for time-dependent inviscid flow. The mass conservation equation is the same as that for a laminar flow but the momentum and energy equations are reduced due to the absence of molecular diffusion.

$$\frac{\partial}{\partial t}(\rho u_i)+\frac{\partial}{\partial x_j}(\rho u_i u_j)=-\frac{\partial p}{\partial x_i}+\rho g_i+F_i \qquad (5.26)$$

where p is the static pressure and ρg_i and F_i are gravitational body force and external forces in the i^{th} direction respectively. F_i also contains other model dependent source terms such as porous-media sources.

These equations also represent the non-linear hyperbolic conservation laws for fluid flow. For hyperbolic equations, information at a given point (boundary condition) influences only the region between the left running wave (rarefaction wave) and the right running wave (shock wave). Simply put, starting with a known initial condition (diaphragm pressure ratio), the solution 'marches' forward in time.

5.2.5 CFD schemes for shock tube flow

The shock tube problem contains two discontinuities once the flow field has been resolved:-

- the shock discontinuity, and
- the contact discontinuity.

The shock is formed due to the removal of the diaphragm separating the higher pressure region from the lower pressure region. The contact discontinuity is the interface

between the shock wave (moving to the right) and the rarefaction wave (moving to the left) as shown in Figure 5.3. Across the contact discontinuity, pressure and velocity do not change but entropy changes discontinuously.

In order to solve the shock problem, an appropriate numerical scheme has to be chosen, which to an extent depends on whether the flow field property of interest is the behaviour of the shock or that of the contact. For gas dynamic problems, an accurate resolution of the contact is important as the temperature changes across the discontinuity. For problems investigating the effects of blast waves on structures, the speed and accurate resolution of the shock might be of prime importance. However, due to its very nature, the resolution of the shock wave is easier than that of the contact discontinuity. Shocks naturally have a compression mechanism that helps their sharper resolution whereas contact discontinuities do not have this compressing mechanism and thus, numerically their spreading tends to increase with time[84].

There are several schemes for solving the one dimensional Eulerian gas dynamic equations (the shock tube problem)[85] and a recent survey of the difference methods for solving the above conservation laws highlights most of the methods which have been applied to solving the flow field in a shock tube. A brief overview is given.

All finite difference methods assume that the solution is regular. However, these schemes produce oscillations[86] behind the shock due to numerical diffusion, dispersion or both due to truncation error. There is also diffusion across the contact discontinuity causing smearing in the course of the calculation. However, it has also been noted that too fine a mesh can also create oscillations behind the travelling shock wave[87].

In order to eliminate or reduce these oscillations, an artificial viscosity term has been developed by several researchers[88]. These reduce the oscillations by allowing the shock discontinuity to occupy a few mesh points whilst having a negligible effect on the smooth parts of the flow where the pressure gradients are not steep. The artificial viscosity will not spread a contact discontinuity as the smearing is due to the truncation error of the numerical scheme. With shocks, the smearing is due to the truncation error of the scheme as well as the artificial viscosity.

Most research on the capture of shock waves[89] and flow through porous media[90] have used the k-ε turbulence model and this is used for the turbulent flow case.

5.3 *The experimental shock tube*

The conventional shock tube consists of a driver section and a driven section. In some instances, the driver section can be of a larger cross-section, however in the work reported here, the shock tube used had a uniform cross-section. Thus the maximum pressure that could be created in the driven channel was dependent on the tube material and not on the geometry of the shock tube. The materials used to construct the shock tube are reviewed below.

5.3.1 Specification of the apparatus

The experimental apparatus consisted of the following components:-

- Tubing material
- Diaphragm puncturing mechanism
- Pressure gauge
- Pressure transducers
- Data acquisition software
- Test section
- Power supply
- Compressor.

A schematic layout of the experimental apparatus is given in Figure 5.5.

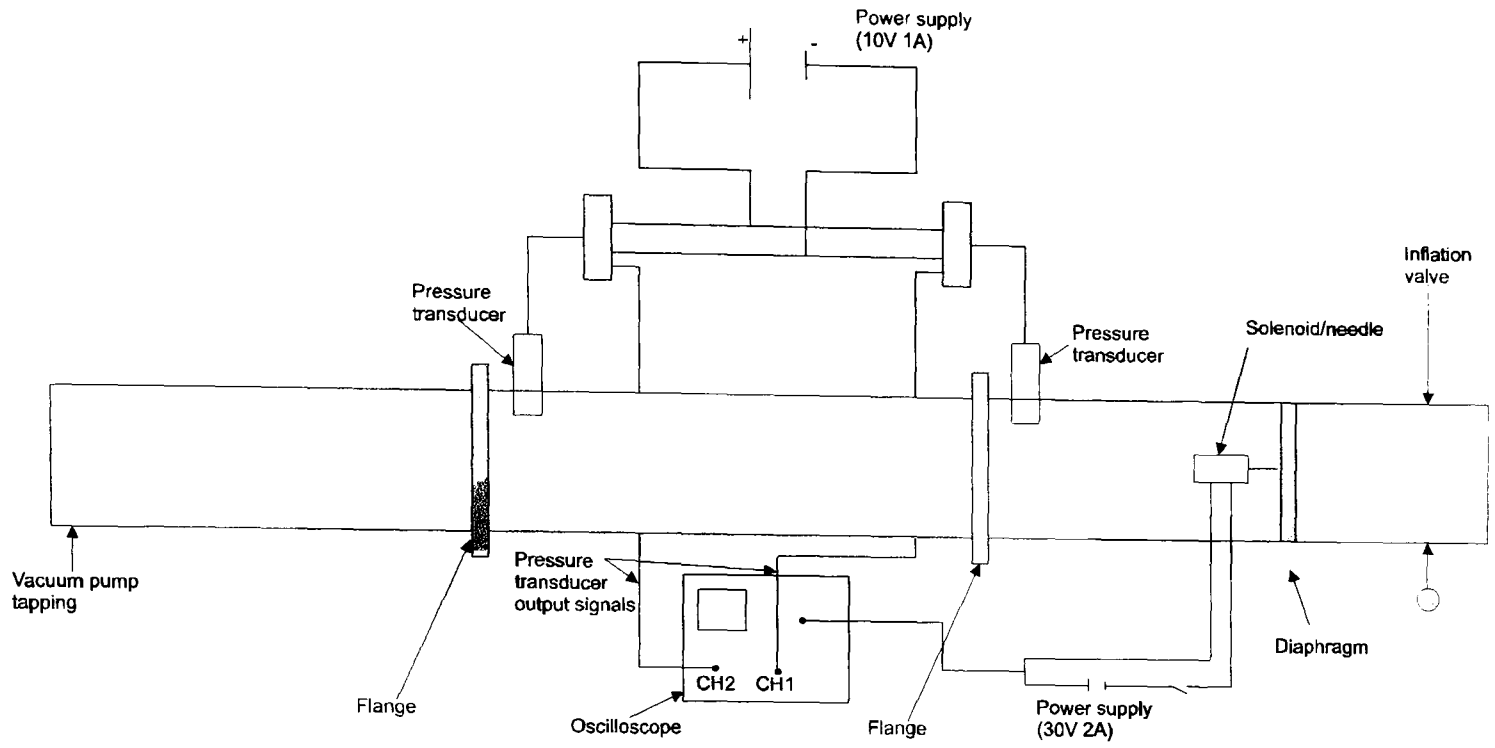

Figure 5.5 - Schematic of the experimental apparatus.

5.3.1.1 Pressure duct

The tube material and pipe fittings used in the tests reported here were manufactured from Acrylonitrile Butadiene Styrene (ABS) with an internal diameter of 55 mm and a wall thickness of 4 mm. The ABS material was capable of withstanding pressures of up to 10 bar at 20°C, most of the testing was carried out at 8.38 bar – 120 psi (gauge) to be precise. The complete shock tube is 15 m in length with a closed end. However, only a 5 m section of the shock tube was used leaving the end open to atmosphere. The driver section was two meters in length and a pressure gauge mounted to give precise readings that would help determine the diaphragm pressure ratio.

An important factor in the choice of the pressure gauge was the fact that upon bursting the diaphragm, the driver channel emptied rather quickly causing a rapid drop in the pressure leading to possible damage to the needle on the pressure gauge. Thus the chosen pressure gauge was filled with a damping fluid (98% Glycerine) and rated at 0 to 16 bar. Subsequent calibration tests revealed that the pressure gauge was under-reading by 10 psi. Thus a true 120 psi was 110 psi on the pressure gauge.

5.3.1.2 Puncturing mechanism

In order to create a shock wave in the shock tube, a diaphragm is used to separate the driver section from the driven section. There are two traditional methods for bursting diaphragms in shock tubes, one is to puncture the diaphragm manually or automatically, and the second is to electrically heat the diaphragm, which eventually leads to it bursting. The electrical bursting method utilises a thin film of metal loaded paint applied in a 'bow tie' configuration as defined by Skews and Law[30]. Figure 5.6 shows this configuration. This method was tested, however due to the diaphragm bowing outward under pressure, the nickel loaded paint cracked and no current could pass through.

Thus the approach adopted was to mechanically burst the diaphragm. This was achieved by externally mounting a brass runner at 45° to the tube and located near the end the driver section. Figure 5.7 shows an assembly of the bursting mechanism. The diaphragm material was Mylar tracing paper reinforced with clear transfer seal material. This material is used for protecting paper cards by encapsulation. This material combination was chosen after extensive tests on the disintegration of various diaphragm material. These materials were tested on their ability to rupture after being punctured with a metal spike whilst under a pressure loading of 8 bar. Some materials rupture prematurely. Figure 5.8 shows the diaphragm material after it has been punctured.

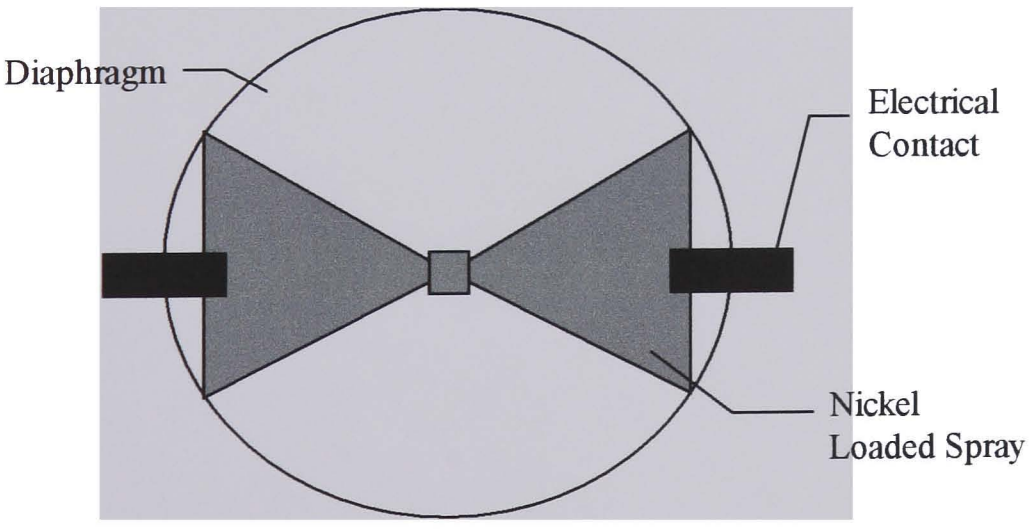

Figure 5.6 - Electrical diaphragm bursting method.

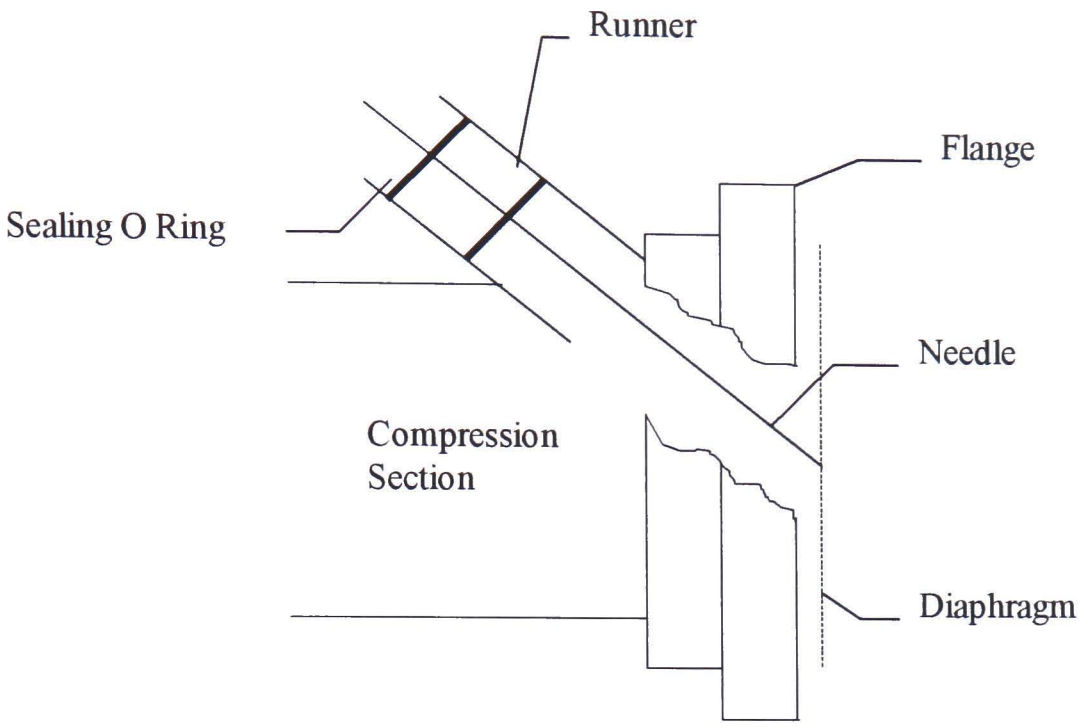

Figure 5.7 - Cross section showing mechanical bursting device.

The mechanical bursting device was mounted atop the driver section of the shock tube.

Figure 5.8 – Punctured diaphragm material.

5.3.1.3 Pressure transducers

Of the three pressure transducers attached to the driven section, two had an operating range of 7 bar to 14 bar (see Figure 5.9). They employed a fully active Whetstone bridge consisting of either semiconductor strain gauges, diffused piezoresistive gauges, or metal foil strain gauges. The strain gauges were bonded either to a thin circular diaphragm that is clamped along its circumference or atomically diffused into a silicon diaphragm configuration. The Entran pressure transducers employed the fully active Whetstone bridge. The Entran pressure transducers had a frequency response of 80 kHz.

In the case of diffused devices, the silicon integrated chip is itself the diaphragm. Applied pressure presents a distributed load to the diaphragm, which in turn provides bending stresses and resultant strains to which the strain gauge reacts. The stress creates a strain proportional to the applied pressure that results in a bridge unbalance. With an applied voltage, this unbalance produces a voltage deviation at the bridge output that is proportional to the net difference in pressure acting upon the diaphragm. Entran made these particular transducers. The third pressure transducer was manufactured by Kistler and had an operating range of 0 to 5 bar. This piezoresistive absolute pressure transducer is made specifically for measuring dynamic and static absolute pressures. Here, the measured pressure acts through a thin steel diaphragm onto a silicon measuring cell. This measuring cell contains diffused piezoresistive resistors connected to a Whetstone bridge that transforms the pressure (due to the unbalance of the bridge) into an output signal amounting to 500 mV at full measuring range.

Figure 5.9 – Entran pressure transducer.

The pressure transducers were used to measure the pressure/time history of the shock wave as it traversed across the shock tube as well as the incident pressure, reflected pressure, and the transmitted pressure across the ceramic foam (see Figure 5.10). These pressure transducers were connected to data acquisition software to allow for the recording of data.

5.3.1.4 Data acquisition software

In order to fully analyse the data from the three pressure transducers, a data acquisition system had to be acquired which allowed easy and comprehensive manipulation of the test data. An ideal system had to be fast enough to capture the initial shock wave and the subsequent reflected wave from the ceramic foam. The acquisition hardware was a 1 MHz data acquisition (DAQ) card that was sufficiently fast to register the various pressures and download them to the analysis software. The data analysis software in question was LabView. National Instruments supplied both LabView and the DAQ card.

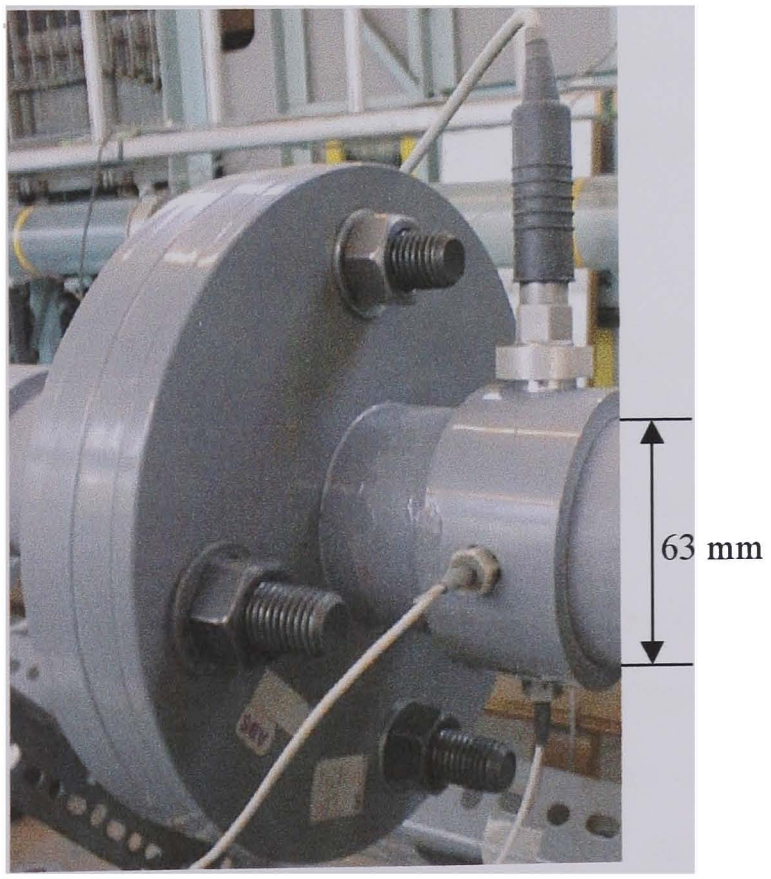

Figure 5.10 – Pressure transducers reading the incident pressure.

The data acquisition card was the AT-MIO-16E-2 and was capable of operating with sixteen single point inputs referenced to ground or eight differential (+ve and –ve channels) inputs.

The LabView software uses a programming language 'G', and also utilises a very high level graphical interface. The 'G' programming language is similar to 'C' in that it uses a modular approach to programming that enables large and complex programs to be broken down into smaller sub-programs. 'G' uses a concept known as virtual instrumentation, VI. A VI is essentially a program that performs functions on and displays measurements using a combination of a transducer or a set of transducers and a DAQ card. Programming a VI is a two-stage process. Firstly, selecting components that are required from a menu provided in LabView draws the instrument panel. Secondly, the block diagram that represents the 'G' program is then put together and wired using the LabView menu system.

In the work reported herein, two sample VIs provided in LabView were modified such that the maximum pressure reading could be ascertained for the post-processing of the data from the pressure transducers. Other modifications included the inclusion of a filter to remove the effects of shock induced vibrations of the shock tube. The figures below show the two VIs that were used to acquire the pressure transducer readings and post-process them.

Figure 5.11 shows the block diagram used in the acquisition of data from the three pressure transducers. The data from the pressure transducers were saved such that a spreadsheet programme such as Microsoft's Excel could read it.

Though the data acquisition card was rated at 1 MHz, the three channels were read at a rate of 15000 scans per second which meant the each channel was scanned 5000 times per second. The inability to use higher scan rates was due to the lack of sufficient memory in the computer used. Thus, the chosen scan rate proved to be the optimum setting for the hardware to read the pressure transducer data and write them to file. A higher scan rate would result in a backlog in the data being written to the computer's hard disk, meaning that previous data would be overwritten before it had been stored.

Figure 5.12 shows the modified VI from the LabView library that was used in the analysis of the data acquired from the three pressure transducers. Modifications to the original VI consisted of maximum and minimum display labels, and a filtering sub-VI for filtering the original noisy signals. The maximum and minimum display labels stored the maximum reading from each transducer for both the original and filtered readings from the pressure transducers. These were plotted together for comparison purposes.

Some tests were then carried out to validate the analytical results for shock tube flow when the pressure in the driver channel is 8.38 bar (120 psi). The results and the methodology for generating these results are discussed in the following section.

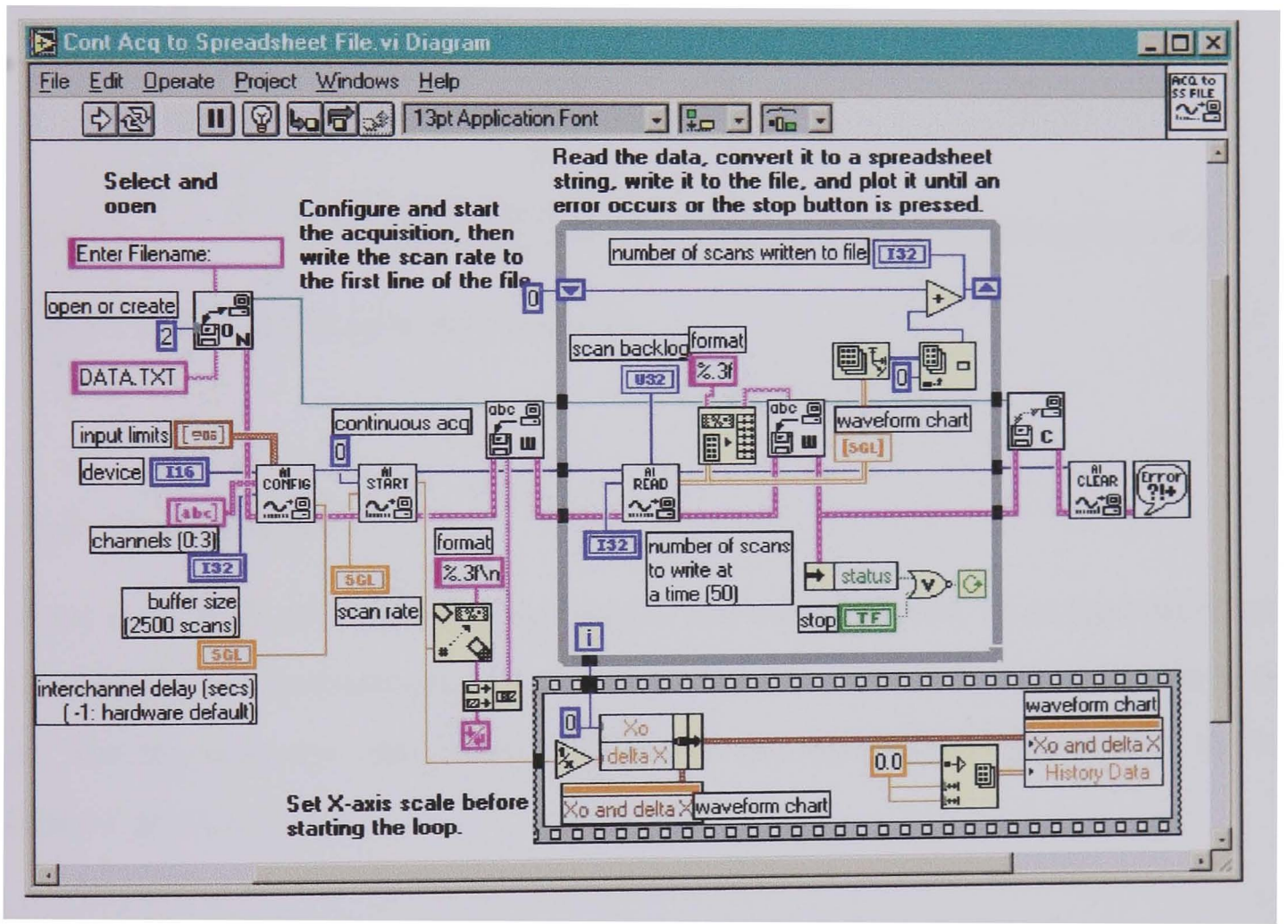

Figure 5.11 – Data acquisition VI.

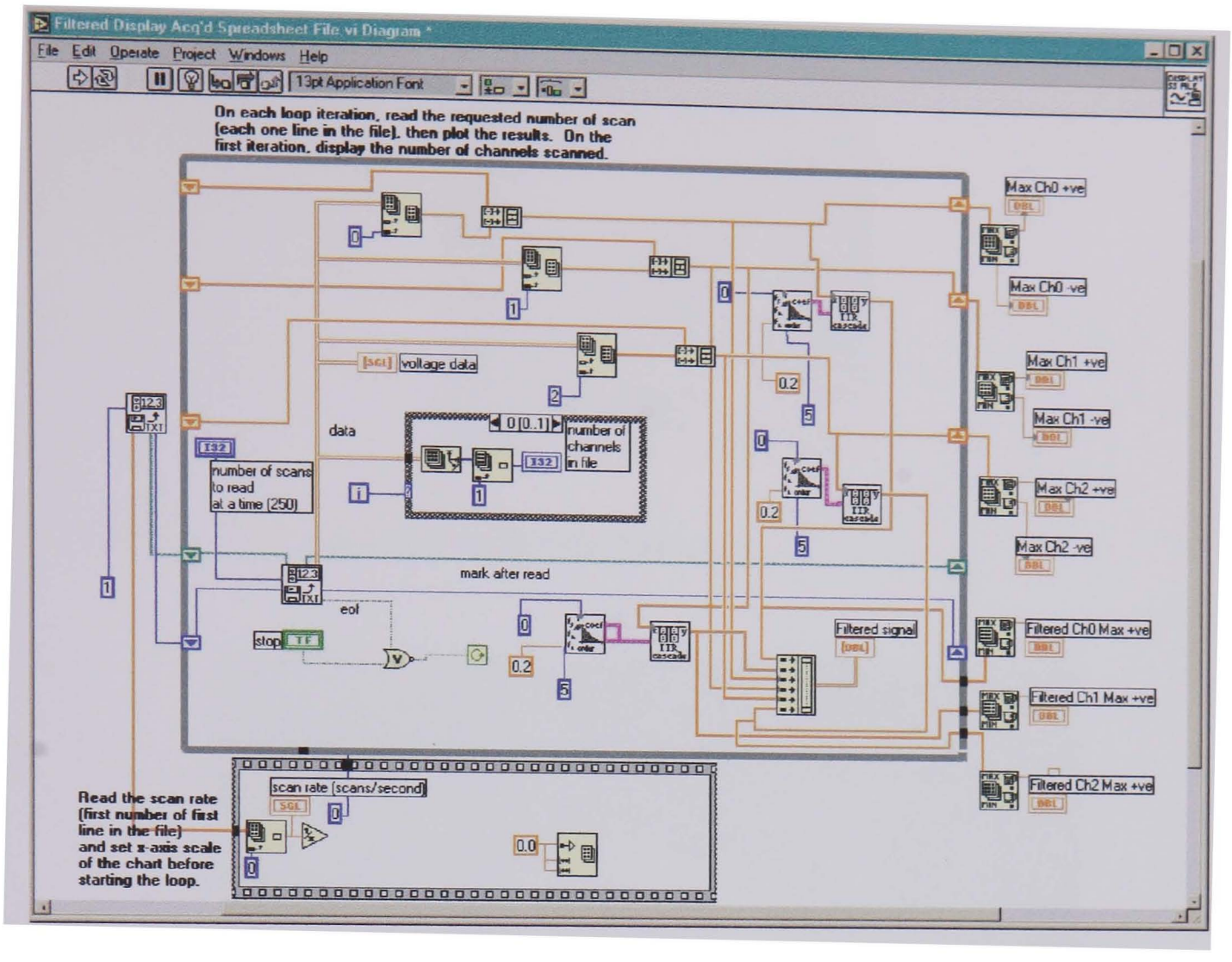

Figure 5.12 – Modified post-processor VI.

5.3.1.5 Test section

As there were slight differences in the forms of the ceramic foams, three types of fixtures were designed and manufactured to accommodate the ceramic foams within the shock tube. The fixtures were made from ABS plastic and aluminium and located in the test section of the shock tube.

The ceramic foam used in this fixture (Figure 5.13) had a smaller diameter than the internal diameter of the shock tube, 50 mm compared with 55 mm.

Figure 5.13 – Ceramic foam holder for Sample 1.

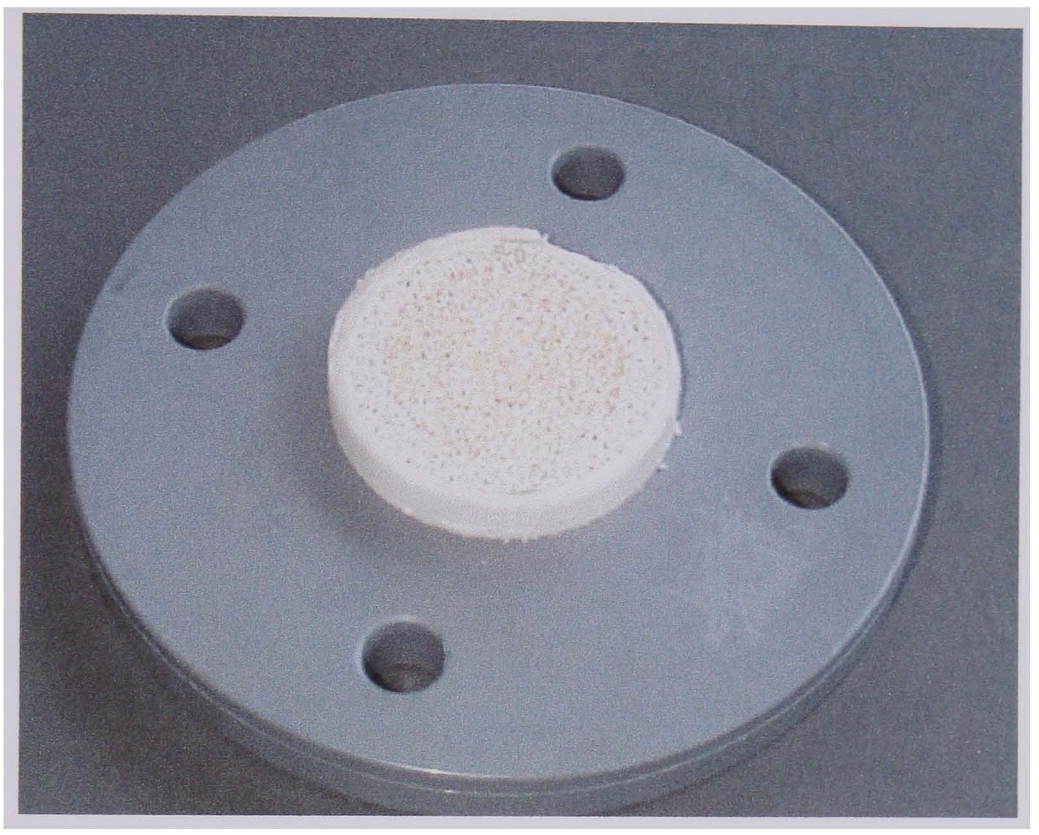

Figure 5.14 – Ceramic foam holder for Sample 2.

Two holders held sample 2 in place as it was thicker than a single holder. Figure 5.14 shows the full diameter of the ceramic foam. As shown in Figure 5.16, only a 55 mm diameter was exposed to the shock wave, as the shock tube had an internal diameter of 55 mm. This left an additional radius of 20 mm through which most of the incident shock wave could dissipate. Such dissipation could not be experienced with the Sample 1 test specimen.

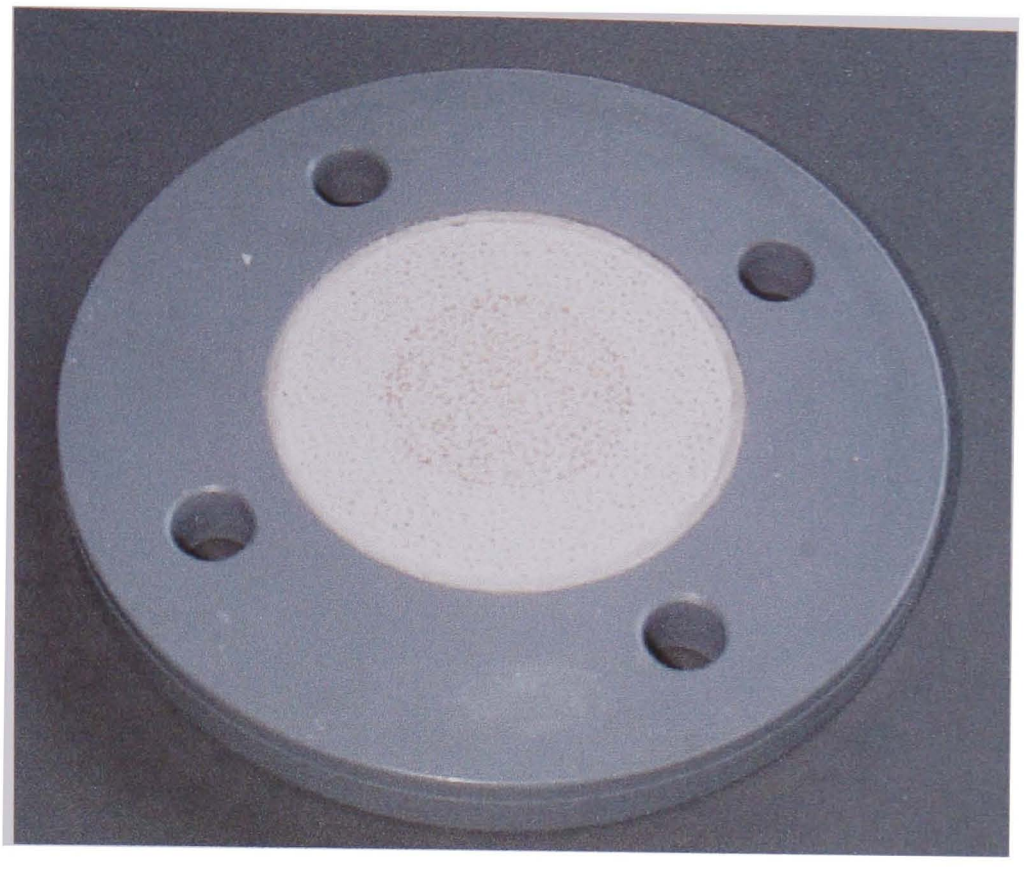

Figure 5.15 – Ceramic foam holder for Sample 3.

Sample 3 was 20 mm in thickness (the thickness of the holder and thus only a single holder was used in these tests. Again, only a 55 mm section of its diameter was exposed to the shock wave as shown in Figure 5.16.

Samples 4, 5 and 6 had a holder that was similar to that used for sample 2.

5.4 The ceramic foam

A number of materials have been used in numerous tests to represent porous media chiefly Silicon Carbide (SiC) and Alumina (Al_2O_3) as used by Levy et al[91] in their work. However, for the tests considered here, the porous media was made from partially stabilised Zirconia (Zirconium Dioxide - ZrO_2).

Zirconia exists as a monoclinic crystal at room temperature inverting to tetragonal phase above approximately 1200°C. The addition of large amounts of a stabiliser such as Magnesium Oxide (MgO) will induce a cubic crystal structure during firing that does not revert to the monoclinic phase upon cooling. The addition of generally less than 10% by weight of stabilisers yields high density ceramic bodies known as transformation

toughened Zirconia or TTZ. Two fundamentally different microstructures exist depending upon the added stabiliser.

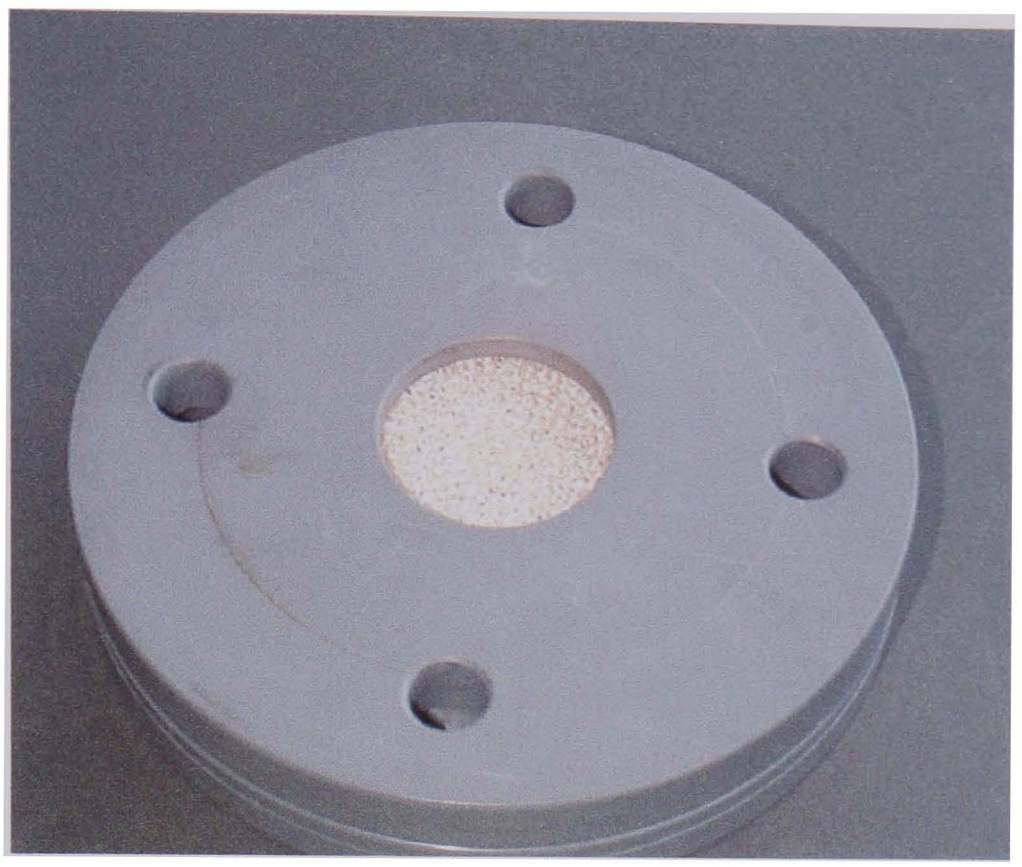

Figure 5.16 – Area exposed to the shock wave for Samples 1 and 2.

The addition of MgO yields a relatively coarse grained (50-100 micron) microstructure known as PSZ or partially stabilised Zirconia. The grains are predominantly of a cubic morphology with a fine precipitate of tetragonal phase dispersed within the grain. Yttria, Y203, additions yield an extremely fine grained (less than 1 micron) microstructure known as TZP or Tetragonal Zirconia Polycrystal. The individual grains are completely tetragonal. Figure 5.17 shows the structure of typical ceramic foam. The structure is similar regardless of the air porosity though as the air porosity value increases, the webs decrease in thickness.

The transformation toughened Zirconias are characterised by high strength and fracture toughness approaching that of the cemented carbides. These characteristics result from stress induced phase transformations of the tetragonal crystals to the monoclinic phase with a corresponding change in volume and local stress field. The TZP's show superior strength and toughness, however, their properties suffer at high temperatures, thus limiting their use to applications below 500°C. The PSZ's retain their desirable

properties at temperatures approaching 1100°C. Zirconia is available in a wide variety of shapes and sizes and is amenable to a wide variety of cold and hot forming techniques.

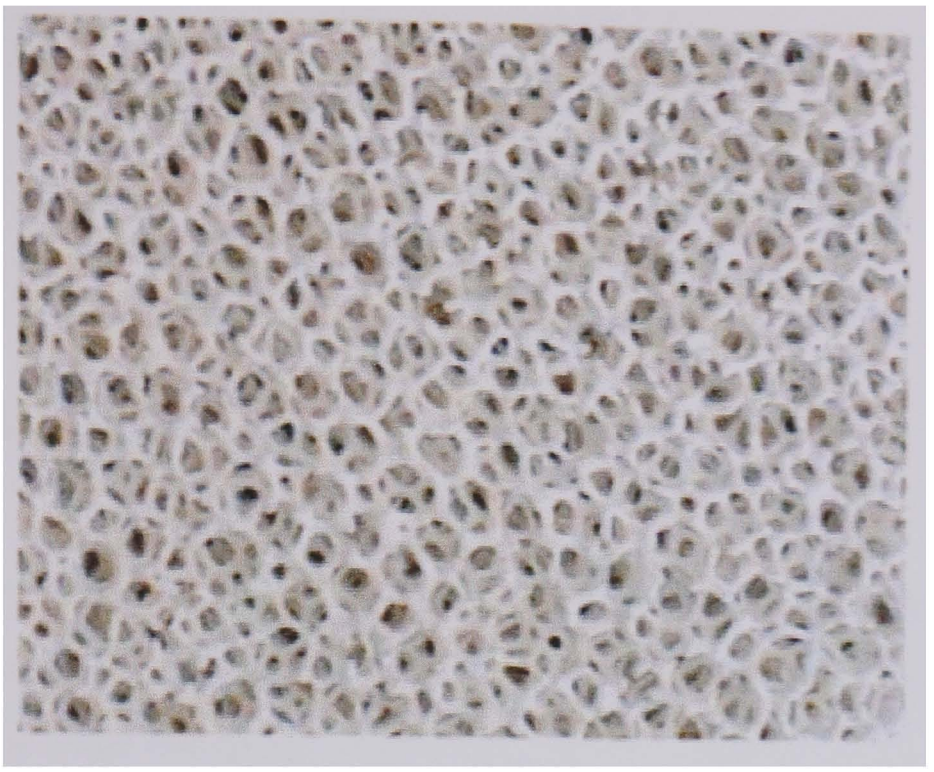

Figure 5.17 – Structure of a ceramic foam.

Zirconia is stable in oxidising and mildly reducing atmospheres. It reacts with carbon, nitrogen and hydrogen at temperatures above 2200°C. It is inert to acids and bases at room temperature with the exception of HF. It experiences a weight loss of 10^{-2} g/cm^{2}s at 2027°C in air, however, this loss is strongly dependent upon the type and quantity of stabiliser used in the ceramic.

Major developing markets for TTZ include thermal barriers for high efficiency heat engines, cutting tools, wear parts, biological implants, certain ferrous metallurgical applications and high temperature oxygen sensors. However, in this application, Zirconia is the proposed explosion door porous material and is manufactured by pouring molten Zirconia over a rigid sponge-like icosahedral structure. The sponge material is then heated until the Zirconia solidifies and the sponge melts. This type of Zirconia is used in the castings industry as a filter when molten metal is being poured into castings. Thus the name ceramic foam is derived from the foam-like structure of the porous Zirconia. Figure 5.18 and Figure 5.19 show the two types of ceramic foam used in the tests conducted.

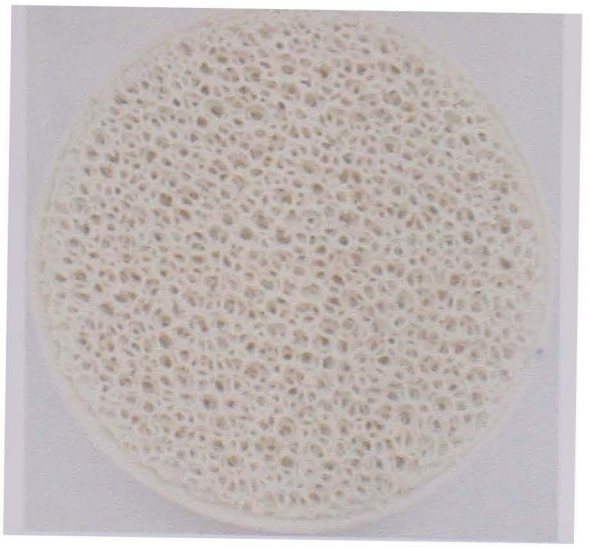

Figure 5.18 – The ceramic foam.

The ceramic foam has several attractive properties such as high density, good hardness value, low thermal conductivity, as well as offering a high porosity/permeability advantage over the other materials.

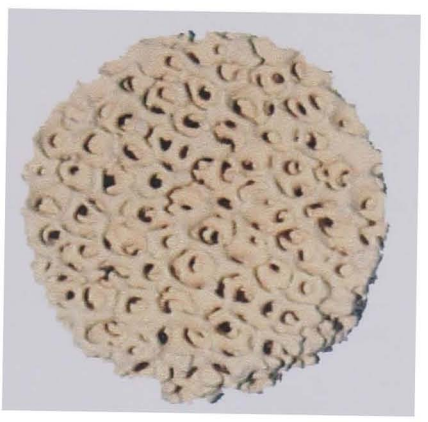

Figure 5.19 – The ceramic foam.

One important parameter used in testing porous media is air porosity. The air porosity of the ceramic foam is used as a measure of the blockage ratio; a measure of the area of the obstructions created by the pores to that of the solid material. The air porosity is calculated as follows:-

$$\phi = 1 - \frac{\rho_c}{\rho_s} \qquad (5.27)$$

where ρ_c is the bulk density of the ceramic foam material and ρ_s is the material density of the skeleton from which the ceramic foam is made. The above expression is limited to gas saturated porous materials. Thus based on a density of 5650 kg/m^3 and a bulk density of typical ceramic foam of 1197.6 kg/m^3, the air porosity was 0.788, or a 0.212 blockage ratio. An air porosity of 0.788 means that 78.8% of the ceramic foam is filled with air and the remaining 21.2% is solid.

Various types of the Zirconia ceramic foam were tested. The main differences between the ceramic foam were the pore sizes, and their thickness. The pore size of ceramic foams is measured as the number of pores per inch (ppi). Typical quoted ppi values are between 10, 15, 20, and 30. For Zirconia 10 ppi ceramic foam, the average pore diameter is in the region of 1346 μm (low density) and 1397 μm (high density). 737 μm (low density) and 838 μm (high density) for 20 ppi ceramic foam, and between 610 μm (low density) and 584 μm (high density) for a 30 ppi ceramic foam. For an extensive review of ceramic foams, the reader is referred to work of Sutton et al[92].

The ceramic foam used in these tests was obtained as free samples from both ceramic foam suppliers and from casting companies. The sizes tested are given in Table 5.2.

Table 5.2 – Ceramic foams tested.

	Test Sample 1	Test Sample 2	Test Sample 3	Test Sample 4	Test Sample 5	Test Sample 6
Diameter, mm	50	75	100	100	100	100
Thickness, mm	20	25	20	25	25	25
Pores per inch, ppi	10	15	20	10	20	30

Test sample 1 had a smaller diameter than the internal diameter of the shock tube thus there is a natural restriction in the passage of the shock wave through it. Such restrictions were not experienced with the other test samples. Test samples 4, 5, and 6 were trapezoidal in shape with the dimensions above indicating the radius for the top and bottom sides of the ceramic foams. The following data are typical of PSZ and TZP ceramics.

Table 5.3 – Properties of Zirconia.

Attribute	Test method/ Measurement*	Value (PSZ)	Value (TZP)
Physical			
Bulk Density	g/cm^3	5.75	6.04
Hardness	$Hv_{0.3}$	1120	1400
Melting Point		2765°C	2765°C
Colour		White to Tan	Yellow to Brown
Crystal Morphology		Cubic, tetragonal, monoclinic	Tetragonal
Mechanical			
Young's Modulus	GPa	203	210
Compressive Strength	MPa	1872	1872
Flexural Strength	MPa	699	1048
Poisson's Ratio		0.23	0.32
Thermal			
Thermal Conductivity	W/mK	1.8	2.7
Specific Heat	J/kgK	400	400
Coefficient of Expansion	$10^{-6}/°C$	10.1	11.0
Maximum Use Temperature		1100°C	500°C
* Room Temperature values except as noted			

5.4.1 CFD equivalent of the ceramic foam

The following calculations were based on a bulk density measured at 1197.6 kg/m^3 and a material density from the Zirconia of 5650 kg/m^3. From equation (5.27), the air porosity is 78.8%.

From this value, it can be deduced that 21.2% of the ceramic foam is solid, thus an equivalent ratio for the CFD model can be calculated.

For clarity and ease of understanding, the following points are highlighted to show the acceptability of the CFD model of the ceramic foam:-

- As the blockage is represented by a ratio of the bulk and material densities of the ceramic foam, a solid volume blockage of 21.2% is dimensionally similar to an area blockage of 21.2%. Simply put, any cross-section of the volume model will have a 21.2% area blockage.
- Modelling the CFD ceramic foam as an axisymmetric problem means that the sections represented as a series of blocks will be rotated through 360. Thus in three dimensions the volume blockage is represented by a series of rings within the porous region of the CFD shock tube.
- As the ceramic foam contains a number of icosahedral structures similar to a collection of small rings, modelling the ceramic foam as an axisymmetric problem makes the CFD model similar to the physical model.
- If the rings were sliced into infinitesimally small sections in the axial direction (cross-section), then they would be similar to a collection of small blocks with the width and height of the cross-section of the blocks in the porous region of the CFD model.

All calculations for the size of the obstructions are based on an area blockage.

Using test sample 1 as the basis for this calculation, the area of the CFD ceramic foam is 1000 mm^2 - based on width of 20 mm and a height of 50 mm. 21.2% of the total area of the ceramic foam is thus 212 mm^2.

The ceramic foam had an average of 115 points[v] per face, and the area of a face normal to the direction of travel of the shock wave is 1735 mm^2 based on a measured diameter of 47 mm, the sample 1 ceramic foam was 20 mm wide. Therefore the number of points per mm^2 (area) is 0.0663 – dividing the average number of points on a face (115) by the area of the face normal to the direction of fluid flow (1735 mm^2).

Now the CFD ceramic foam would occupy (when taking advantage of the symmetrical nature of the shock tube and the ceramic foam) an area of 500 mm^2 (25 mm x 20 mm) and 21.2% of this is 106 mm^2.

Thus the number of points over the CFD ceramic foam could then be calculated as follows:-

- the number of points per face (0.0663/mm^2) multiplied by the total area occupied by the CFD ceramic foam (500 mm^2).
- the number of points is 33. The area of each point is then the area of the ceramic foam that is solid (106 mm^2) divided by 33; 3.21 mm^2,
- to represent an air porosity of 78.8%, the CFD ceramic foam had to have a region with 33 blocks each with an area of 3.21 mm^2.
- The dimensions of each block was chosen such that it would be square in section.

Figure 5.20 shows a layout of the obstructions placed in the CFD shock tube for the sample 1 ceramic foam.

A similar analysis was done for the sample four ceramic foam. This was necessary as the ceramic foam had a diameter that was larger than the internal diameter of the shock tube, whereas, the sample 1 ceramic foam was of a smaller diameter. Figure 5.21 shows a typical layout of the CFD model of the ceramic foam within the shock tube. Note that samples 2 to 6 had this type of layout.

---

[v] The points on each face are the corners of the icosahedral structure of the ceramic foam. These points were the solid portions of the ceramic foam that would present an obstruction to the passage of the impinging shock wave.

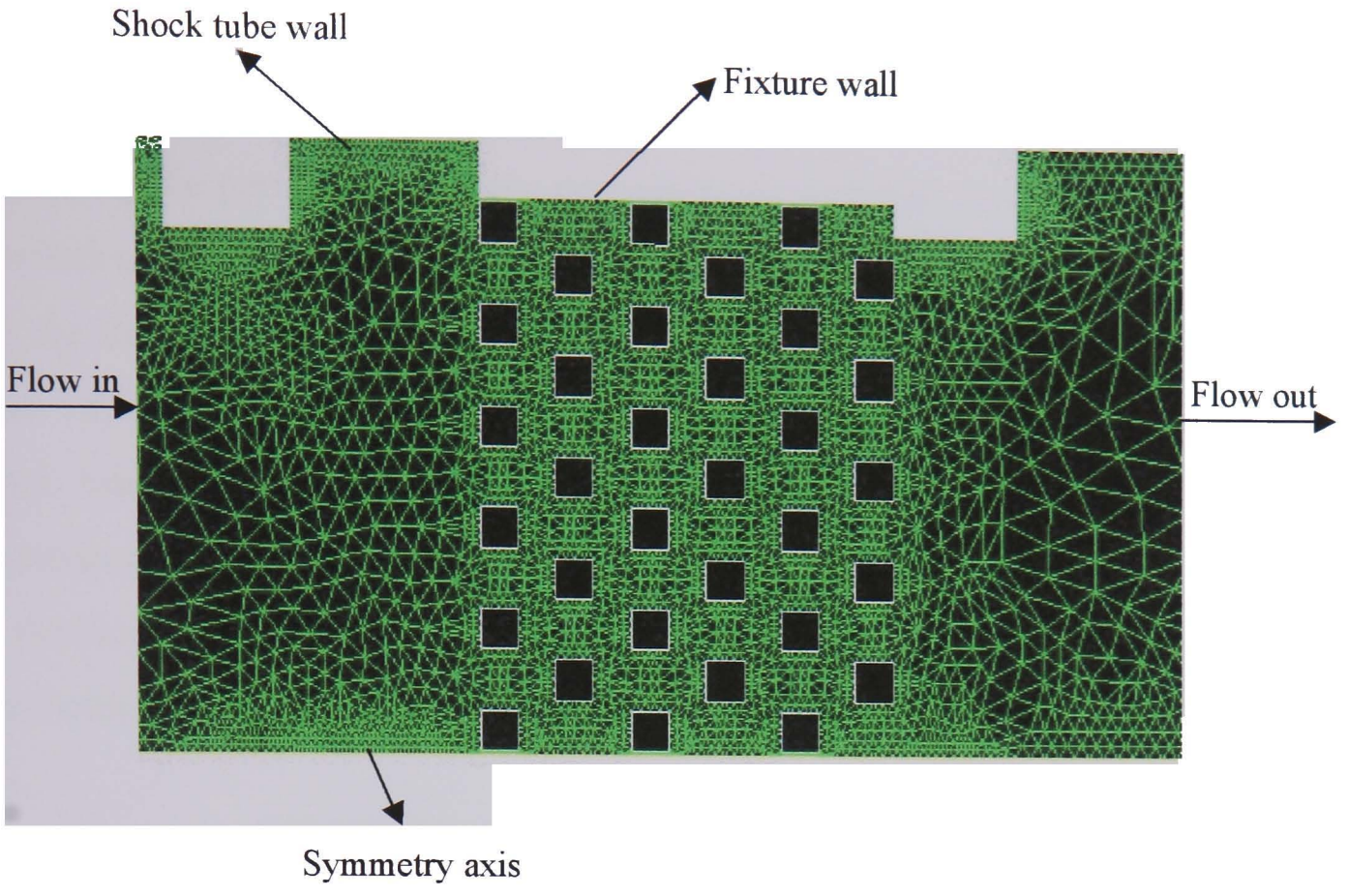

Figure 5.20 – Typical layout of the obstructions in the porous region – Sample 1.

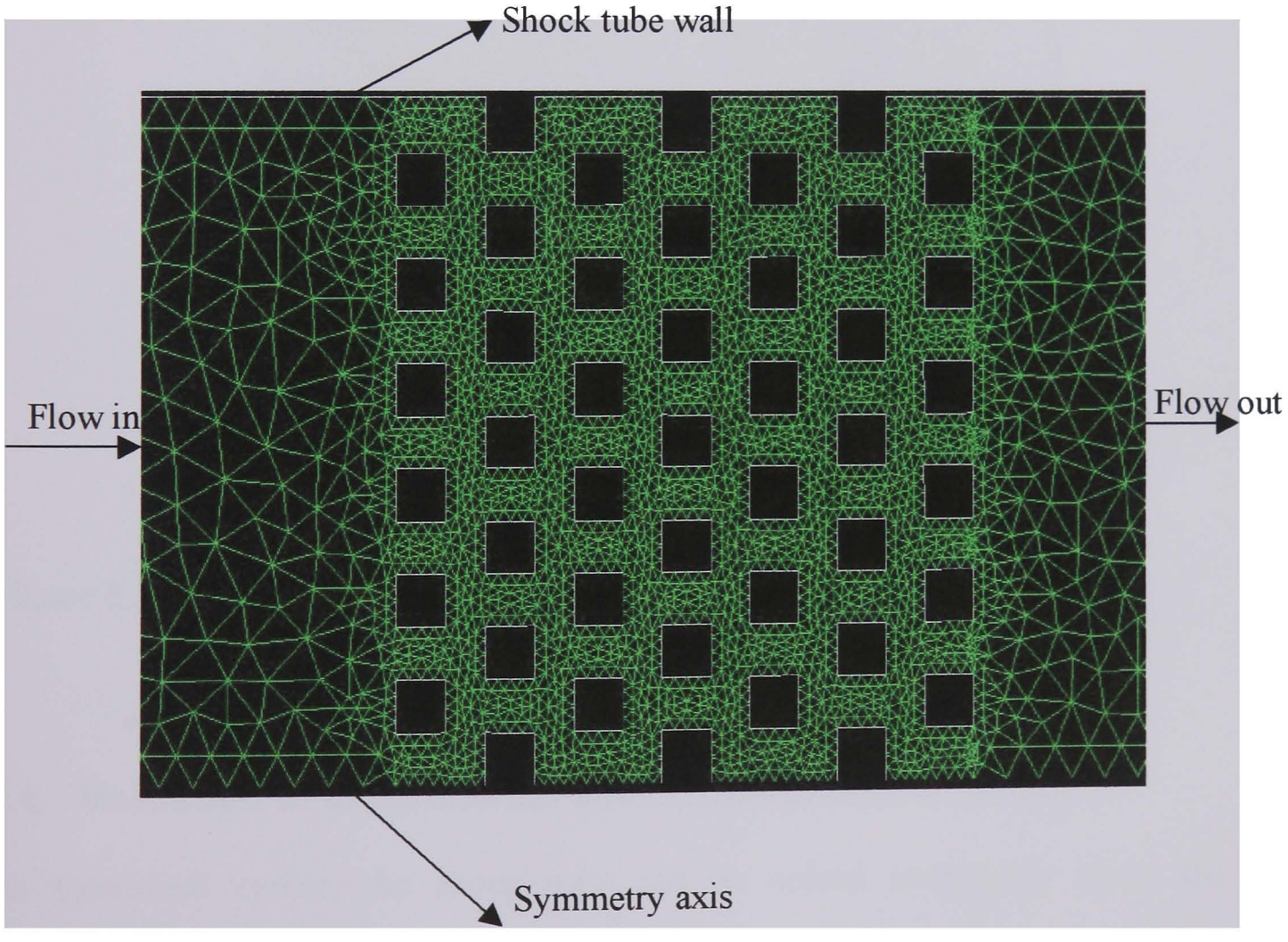

Figure 5.21 - Typical layout of the obstructions in the porous region – Sample 4.

5.5 The orifice plates

The orifice plates were used in these experiments to provide a useful means of correlating the performance of the ceramic foam with that from the orifice plates. The correlation table generated could provide an equivalency chart between the ceramic foam and the orifice plates. The orifice plates used in these tests were fabricated from mild steel. The appropriate hole diameters were calculated as a percentage of the internal shock tube diameter. Once the correct diameter for a particular configuration was ascertained, the holes were punched on the 2 mm thickness mild steel plate. Depending on the blockage area (BA), each orifice plate had a single hole, two holes, four holes, or nine holes. (See Table 6.1). Figure 5.22 shows four configurations of the orifice plate.

Figure 5.22 – Orifice plate configurations (80% BA).

5.6 Validation of experimental shock tube and CFD results

As mentioned earlier, the shock tube can be solved analytically given the initial diaphragm pressure ratio (p_4/p_1) using equation (5.25) to resolve the incident pressure ratio p_2/p_1. Once the incident pressure ratio is obtained the moving shock Mach number

can be calculated using equation (5.14). In order to validate the computational and experimental results some tests were conducted on the CFD model and in the experimental shock tube with the diaphragm pressure ratio set at 8.38:1 representing a driver section pressure of 8.38 bar and atmospheric pressure in the driven section. This diaphragm pressure was chosen as the tube material could withstand a maximum pressure of 10 bar before possible failure.

For the above mentioned diaphragm pressure ratio, the *incident pressure wave*, $p_2 p_1$ is 2.65 bar, and the moving shock wave Mach number is approximately 1.55 – see Table 5.4. With an average room temperature of approximately 300 K, the shock wave should be moving with a velocity of approximately 539 m/s. From equation (5.16), the motion induced by the passage of the shock wave, i.e., the speed of the flow behind the shock wave is 263 m/s.

All the above values were obtained analytically using equations derived for solving one dimensional motion as per that in a shock tube. Experiments were then conducted using the same initial values, i.e. a diaphragm pressure ratio of 8.38:1.

Though the CFD results are given in section 5.6.3 in this validation exercise, the CFD model is described in detail in subsequent chapters.

5.6.1 Positioning of the pressure transducers

The pressure transducers detected the arrival of the incident and reflected shock waves after the diaphragm had been punctured. These transducers had to accurately record the pressures and subsequently store the data through the data acquisition software. In order to accurately register the pressure values, the positioning of each transducer within the shock tube wall was critical. They had to be positioned such that they did not protrude into the inner wall of the shock tube, as this would create turbulence as the passing shock wave impinged upon them. Adapters were designed and manufactured to properly secure the pressure transducers on to the shock tube wall as well as to reduce the effects of vibration induced by bursting the diaphragm.

Two pressure transducers were positioned 70 mm upstream of the test region (but at different positions along the circumference) to record the incident and reflected pressures. Further downstream of the test region of the shock tube, a sensor recorded the transmitted pressure as the shock tube exited either the porous media or the orifice plate. The downstream pressure transducer was located 210 mm from the test region as the CFD simulations revealed that placing a sensor 70 mm downstream failed to capture the peak pressure magnitude. This observation was also borne out by experiments.

For incident pressure tests, all three transducers were positioned 70 mm upstream of the test region on the same circumferential axis. The incident pressure value was taken from the average of the readings from the three pressure transducers. All the pressure transducers were independently calibrated to determine their accuracy.

5.6.2 Initial experimental and CFD results

Obtaining results from the experimental shock tube follows a set procedure. The diaphragm is inserted between the driver and driven sections, locking it in place with four nuts and bolts. The driver section is filled with compressed air via a Schraeder valve mounted on the driver section tube. The diaphragm region is then checked for any air leaks until the pressure on the gauge registers a true 120 psi (gauge). The data acquisition process is then activated and the diaphragm punctured. A trace is registered on the data Video Display Unit (VDU) terminal signalling the passage of the shock wave and the subsequent data capture and hence the termination of the acquisition process.

This process is repeated six times. The data collected are then post-processed using a modified Virtual Instrument (VI) from the LabView suite of programs. An average incident pressure value is then collected and the moving Mach number is calculated from the time between the detection of the pressure pulse from two pressure transducers positioned approximately 140 mm apart.

Figure 5.23 shows a sample pressure plot from the pressure transducers. The pressure transducer reading channel 0 and channel 2 are the first to detect the arrival of the shock wave and are located on the same circumferential axis. The channel 1 pressure

transducer is located further downstream and detects the arrival of the shock wave some time later.

The original noisy signals are filtered to show a more representative signal where the passage of the shock is indicated by a step jump followed by a continuous pressure increase which then decreases as the flow behind the incident shock decreases in strength. As the shock tube was open ended, the pressure in the driver section in time decayed to the original pressure before the arrival of the shock wave. The sensors all had different initial offset values thus the reason for the plots not emanating from the same point.

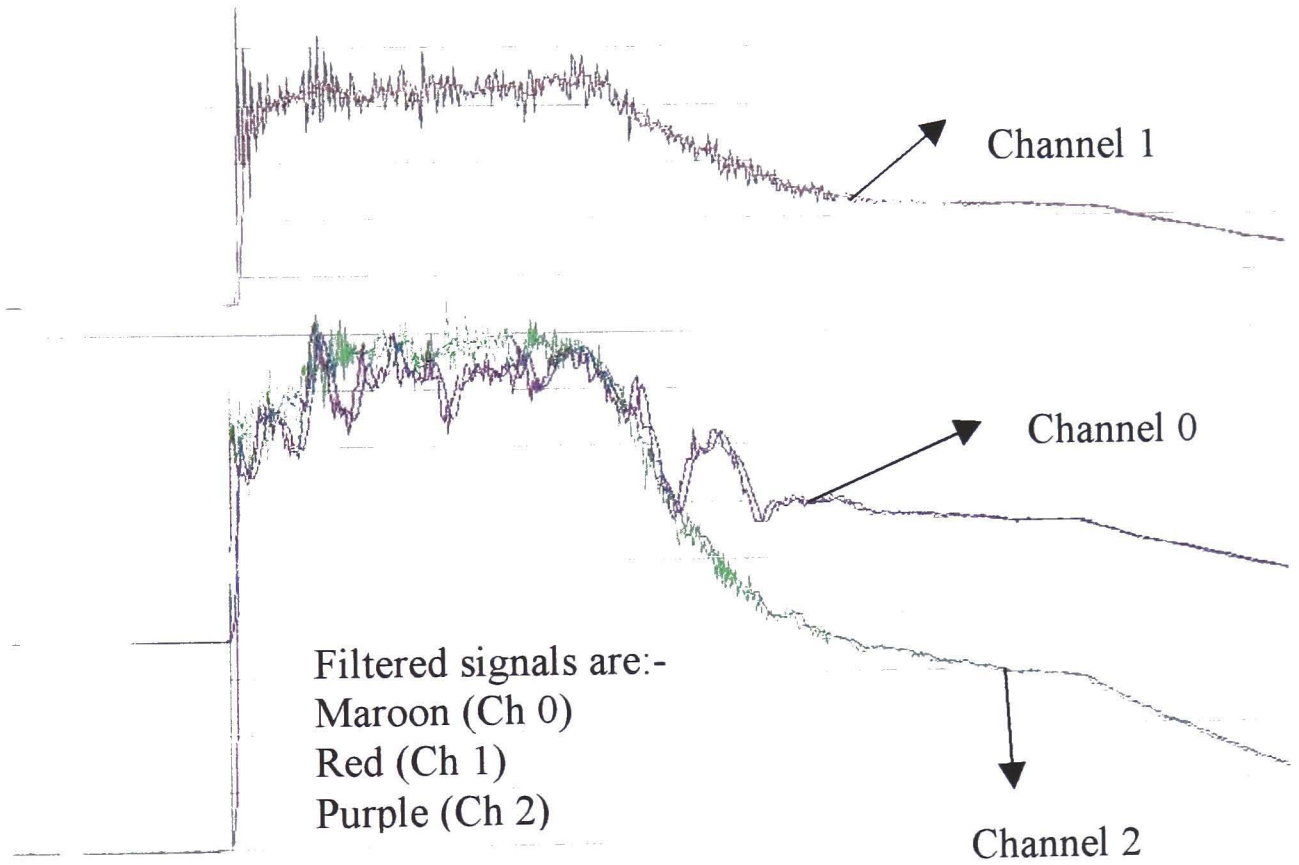

Figure 5.23 – A sample pressure transducer reading from the experimental shock tube.

The peak (filtered) pressure registered by the pressure transducers was 2.3 bar and the minimum was 2.0 bar. The shock wave Mach number was calculated as 1.49 by measuring the time taken for the shock wave to be detected by the pressure transducers at Channel 0 and Channel 2, and Channel 1. The differences between the experimental, analytical, and computational results will be discussed later in this chapter.

CFD simulation results obtained for the incident pressure validation tests are shown in Figure 5.24. The end wall at the driver section of the shock wall is the origin. The diaphragm is located 2 m from the end wall and it separates the driver section from the driven section of the shock tube. Once the diaphragm has been removed, the shock wave moves to the right and an expansion wave moves to the left. Thus Figure 5.24 shows a typical pressure profile in the vicinity of the shock wave within a shock tube.

A detailed account on how these results were obtained will be given in chapter 6. The CFD incident pressure average value is 2.67 bar and using equation (5.14), the shock wave Mach number is 1.56. The speed of the flow behind the moving shock wave is 265.6 m/s using equation (5.16).

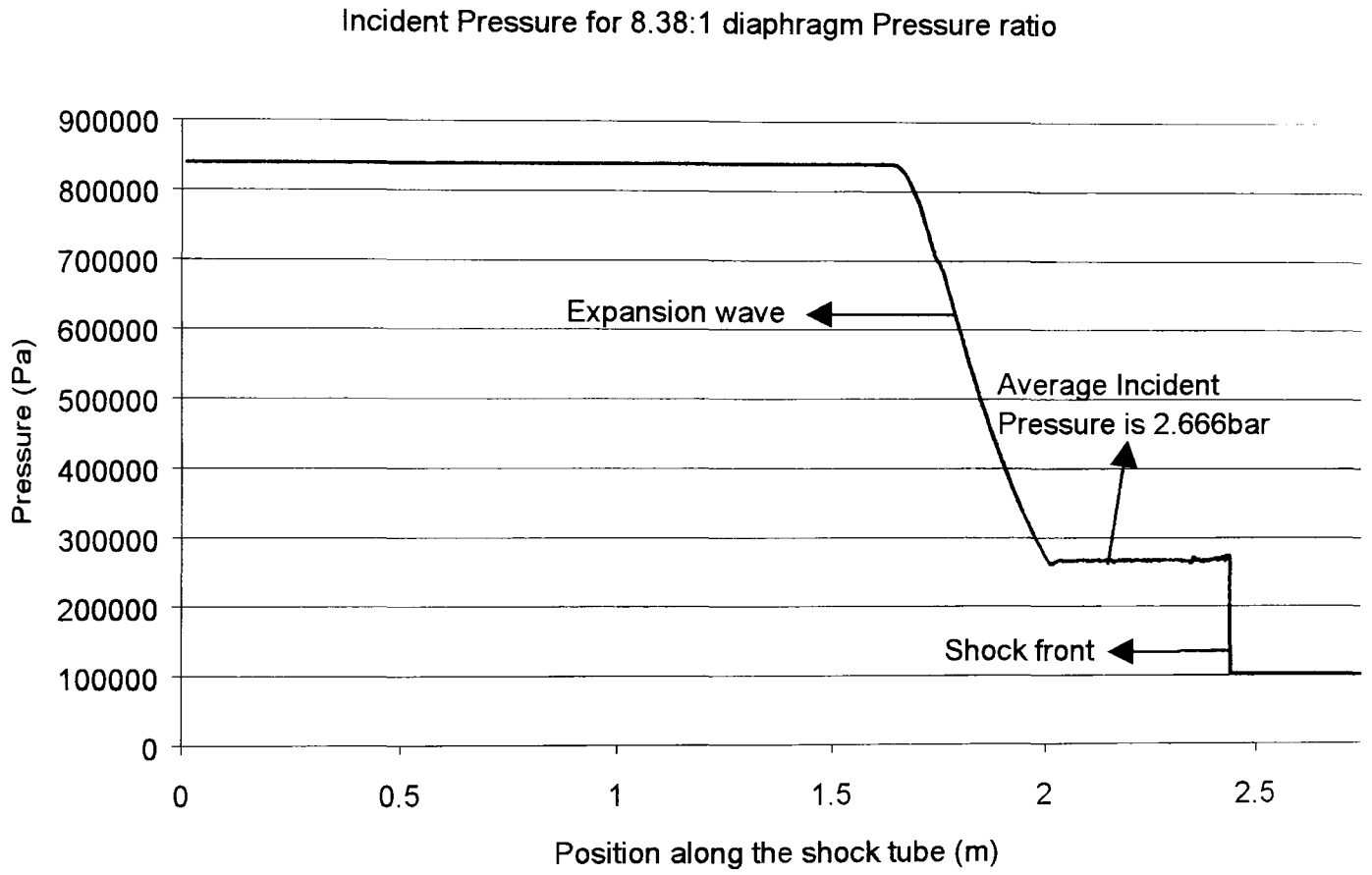

Figure 5.24 – Typical incident pressure profile from the CFD shock tube.

5.6.3 Discussion of the analytical CFD simulations and experimental results

The experimental and CFD simulation results were compared with the analytical results. From Table 5.4, the experimental and CFD simulation incident pressure results are within a margin of ±13% of the analytical incident pressures.

The differences between the lower experimental results and those from the analytical and CFD simulation results could be due to the following observations:-

- the diaphragm not being broken instantaneously and totally,
- the shock tube problems is described as a one-dimensional flow problem, whereas the experimental shock tube is primarily a three-dimensional flow problem, and
- the vibrations induced by the bursting of the diaphragm are not represented in the CFD simulations and the analytical calculations.

The results from the CFD simulation of the flow in the shock tube without any obstructions are in agreement with the analytical results. These initial tests showed the incident pressures tests and no obstructions were placed within the shock tube.

From Table 5.4, it can also be seen that the CFD simulations and experimental results in reasonable agreement.

Table 5.4 – Results comparison.

	Analytical	Experimental	CFD simulation
Incident Pressure, Bar	2.65	2.30	2.67
Mach number	1.55	1.49	1.56
Induced flow velocity, u_p, m/s	263.3	239.1	265.6

5.7 Conclusion

This chapter introduced the porous media and the experimental set-up. As part of the experimental apparatus, the shock tube was described and the numerical generation of shock waves was also presented. An advantage of shock tube flow is the ability to solve the incident pressure magnitude, the incident shock wave, density and temperature analytically. Such an advantage allows for the comparison between the experimental, computational, and analytical results.

Specifications for all the experimental apparatus and brief descriptions on the diaphragm material and the puncturing mechanism were given. A mechanical bursting device was used as the electrical bursting method was not reliable and prone to premature failure. The transducers used to gather the pressure history of the shock wave were discussed along with the data acquisition software used in conjunction with the pressure transducers. The data acquisition software also allowed post-processing of the acquired pressure history and a sample of the pressure profile from the experimental tests was shown along with that from a CFD simulation. This showed that the original signals from the pressure transducers were noisy and had to be filtered to produce meaningful results.

The ceramic foam material was discussed along with the fixtures designed to secure the ceramic foams within the test section of the shock tube. The structure of the ceramic foam was such that it could be modelled using CFD and assuming axisymmetric flow. Such an assumption it was revealed led to the ceramic foam being modelled as a series of rings similar to the icosahedral structure of the physical ceramic foam.

Initial validation tests revealed that the CFD simulations produced results that were similar to the analytical solutions. However, the experimental results were not as accurate as the CFD simulations or analytical solutions. Reasons for the differences were primarily due to the behaviour of experimental diaphragm not being accounted for in either of the numerical and analytical solutions, and shock induced vibrations from the experimental shock tube. However, the results were reasonably close to make analysis possible.

The numerical model of the ceramic foam is described in the next chapter along with the experimental results for the orifice plates.